# Predictive Modeling of a PEMFC Cathode Humidifier

by

Alexander Proracki

A thesis
presented to the University of Waterloo
in fulfillment of the
thesis requirement for the degree of
Master of Applied Science
in
Chemical Engineering

Waterloo, Ontario, Canada, 2010

## Author's Declaration

I hereby declare that I am the sole author of this thesis. This is a true copy of the thesis, including any required final revisions, as accepted by my examiners.

I understand that my thesis may be made electronically available to the public.

## Abstract

The durability and performance of commercially available polymer electrolyte membrane fuel cell (PEMFC) technology depends heavily on adequate humidification of the membrane electrode assembly (MEA). Early generation automotive fuel cell stacks will likely rely on an external humidification process based on gas-to-gas membrane planar humidifiers to humidify the inlet cathode stream. The membrane-based humidifier systems allow the reactants to receive recycled heat and moisture from the cathode outlet stream.

The objective of this thesis is to develop a flexible, computer-based simulation tool that can be used to aid in the design of these planar humidifier systems. The simulation is based on fundamental mass transfer concepts and experimental membrane behaviour based on literature results. It was determined that the mass transfer resistance through the membrane is several orders of magnitude higher than the resistance contributed by the gas diffusion media (GDM) and thus the mass transfer resistance through the GDM are not considered. An important point to note is that the Schroeder's Paradox observed in perfluorosulfonic acid (PFSA) membranes implies that membranes in contact with liquid water will exhibit higher mass transfer than membranes in contact with saturated water vapour despite the fact that the water activity in both situations are unity. Initial simulations for which no liquid water was present resulted in a humidifier water transfer rate less than half the rate observed experimentally. Thus it was hypothesized that condensed liquid water was present on the wet-side of the humidifier membrane and as such this work assumes a fraction of the membrane surface is covered by liquid water while the rest of the membrane is exposed to gaseous water concentrations comparable to the bulk channel stream above the GDM.

For typical operating conditions the outlet wet-side stream retains 92% of the inlet water content and as such it was hypothesized that constant fractional liquid water coverage across the membrane could be assumed. Later simulations confirmed the validity of this hypothesis. Six models of water coverage estimation were derived using least squares and factorial design methods. The models were compared however no single method was determined to be superior for all situations as the methods exhibit similar sums of squared error.

## Acknowledgements

I would like to acknowledge the Natural Sciences and Engineering Research Council (NSERC) and Dana - Long Manufacturing for their generous financial support for this project. I would also like to thank Brian Cheadle, Doug Vanderwees and Manaf Hasan for their assistance during my time in Oakville.

Special acknowledgements go out to Jeff Gostick, Alishah Jesani and Matthew Kok for their efforts in both building the test station as well as providing assistance at all points of the project.

Dr. Fowler's input and support for this project has been greatly appreciated. His supervision has always helped guide this thesis towards completion. I would also like to acknowledge Zhongwei Chen and Roydon Fraser for their contributions as readers of this thesis.

Finally I would like to acknowledge the hard work and dedication of all the undergraduate co-op students that contributed to this project: Alishah Jesani, Chris Jang, David Wan, Dawn Riekenbrauck, Dylan Finley, Matt Bellissimo, Nikkilynn Sepnio, and Yo Han Na.

## Dedication

I would like to dedicate this thesis to all my family and friends who helped make this accomplishment possible. Completing this project would not have been possible without the support from all of you.

First of all I would like to thank Cat for all her confidence in me and her support throughout our time together. Your patience and kindness have pulled me through some frustrating times.

I would also like to thank my parents Anthony, Wendy, Michelle and Scott for their unwavering support throughout my time at the University of Waterloo. I also couldn't forget my grandparents Olive, Olga and Stan who are the greatest public relations group anyone could hope for.

Special thanks go out to my lab-mates Charles, Ivan and Faraz. The three of you made the office just a little less dreary. Ivan your skill with synonyms and your patience with proof-reading has been priceless. Faraz you can always find the time for a little brainstorming around the office or at home.

Finally I'd like to extend my gratitude to all the friends that kept me going for the last two years: Angela, Kate, Sahar, Bonnie, Matt Wurtele, Dave Dorschner and James Rigsby.

# Table of Contents

# List of Figures

# List of Tables

# Nomenclature

PEMFC - Polymer electrolyte membrane fuel cell

GDM - Gas diffusion media

PTFE - Polytetrafluoroethylene (Teflon®)

MPL - Microporous layer

PFSA - Perfluoronated sulphonic acid

RH - Relative humidity

DI – Deionized

CNT - Carbon nano-tubes

OCV - Open circuit voltage

CEM - Controlled evaporator mixer

DAQ - Data acquisition (unit)

PID - Proportional integral derivative (controller)

USB - Universal serial bus

CFD - Computational fluid dynamics

NPT - National pipe thread

CNC - Computed numerically controlled

IMC - Internal model control

GRG2 - Generalized reduced gradient

# 1. Introduction

New technology must be developed for managing energy resources as consumer demand for environmentally responsible energy increases. One such technology, the polymer electrolyte membrane fuel cell (PEMFC), is in the early stages of commercialization. The market for PEMFCs currently consists of early adopters such as public transportation, military applications and government projects [1], [2], [3]. It is clear that the vehicles used within the transportation sector are moving away from the single-technology internal combustion power-train exhibited in the 20$^{th}$ century. A major proponent of this change is the increased desire for energy security. Supposing that the transportation sector of the future is powered by an array of energy sources the transportation operation cost will be far less sensitive to price fluctuations for a single energy source.

PEM fuel cells contain a polymer electrolyte membrane that must be adequately humidified. The ionic conductivity of this membrane is a strong function of membrane humidity thus the fuel cell must be fed reactant streams with high relative humidity levels to ensure proper humidification of the polymer membrane. This project investigates the behaviour of a prototype cathode humidifier with the intention of building a MATLAB-based humidifier simulation tool to estimate cathode humidifier performance.

The fundamental concept of a hydrogen fuel cell was first demonstrated in 1839 by William Grove [4]. The premise of the fuel cell, in the case of PEMFCs, is to convert the chemical energy stored in hydrogen and oxygen gas into electrical energy. The fundamental reactions in such a cell are as follows:

Anode Reaction: $$H_2 \overset{Pt}{\rightarrow} 2H^+ + 2e^- \quad \text{(Eq1)}$$

Cathode Reaction: $$\frac{1}{2}O_2 + 2H^+ + 2e^- \overset{Pt}{\rightarrow} H_2O \quad \text{(Eq2)}$$

Overall Reaction: $$H_2 + \frac{1}{2}O_2 \overset{Pt}{\rightarrow} H_2O \quad \text{(Eq3)}$$

These reactions stipulate that in order for a fuel cell to operate, hydrogen and oxygen are consumed while water is produced as a by-product. The electrons produced at the anode travel

through the external circuit and are consumed at the cathode. This external circuit is often the electrical load which draws its energy from the fuel cell. The protons generated at the anode are conducted through the polymer electrolyte membrane to be consumed at the cathode. This conduction mechanism releases thermal energy, as do the cathode and anode half-reactions. A complete reaction that could describe fuel cell operation is as follows:

Complete Reaction: $$H_2 + \frac{1}{2}O_2 \overset{Pt}{\rightarrow} H_2O + electrical\ energy + heat \quad \text{(Eq4)}$$

The amount of water in a fuel cell is critical to optimal fuel cell operation. Accumulating an excess of water causes the gas flow paths to be restricted while a dearth of water results in decreased fuel cell performance. This decrease in performance is covered in Section 2.4.2 and is caused by drying of the membrane. Due to the critical importance of maintaining appropriate humidification in the fuel cell, the amount of water present must be actively controlled either by designing self-humidifying fuel cell stacks or by having an external unit to control the humidification.

Insufficiently humidified fuel cell stacks will exhibit increased ohmic losses due to the loss of hydronium ion transport pathways, illustrated in Section 2.4.1. As the water content of the membrane decreases these transport pathways shrink resulting in a decreased ability for ion transport. Section 2.2 will reveal that increased fuel cell stack ohmic losses can significantly affect fuel cell performance at moderate to high current densities. Conversely excessively humidified inlet gas streams can result in condensed liquid water within the gas diffusion media (GDM). Large amounts of liquid water within the GDM pores can result in "flooding" which is characterized by severely impeded gas transport to the catalyzed membrane surface. It is imperative that inlet gas stream humidity levels must be finely controlled in order to balance the ohmic losses associated with insufficient humidification and the mass transport losses associated with excessive humidification.

Section 2.8 discusses several humidifier designs however this work shall focus on the planar membrane humidifier design. The objective of this work is to develop a new simulation tool based on experimental data that can be used as an aid in the design of PEMFC cathode humidifiers.

# 2. Background

## 2.1. PEM Fuel Cell Structure

As presented in Equation 1 through Equation 3, the protons generated by the anode half-reaction move from the anode-side catalyst layer through the proton exchange membrane to the cathode-side catalyst layer at which point they react with the oxygen fed to the cathode-side. Figure 1, located below, illustrates a typical polymer electrolyte membrane fuel cell [5]. This figure serves as a visual representation of the components described in Sections 2.1.1 through 2.1.5.

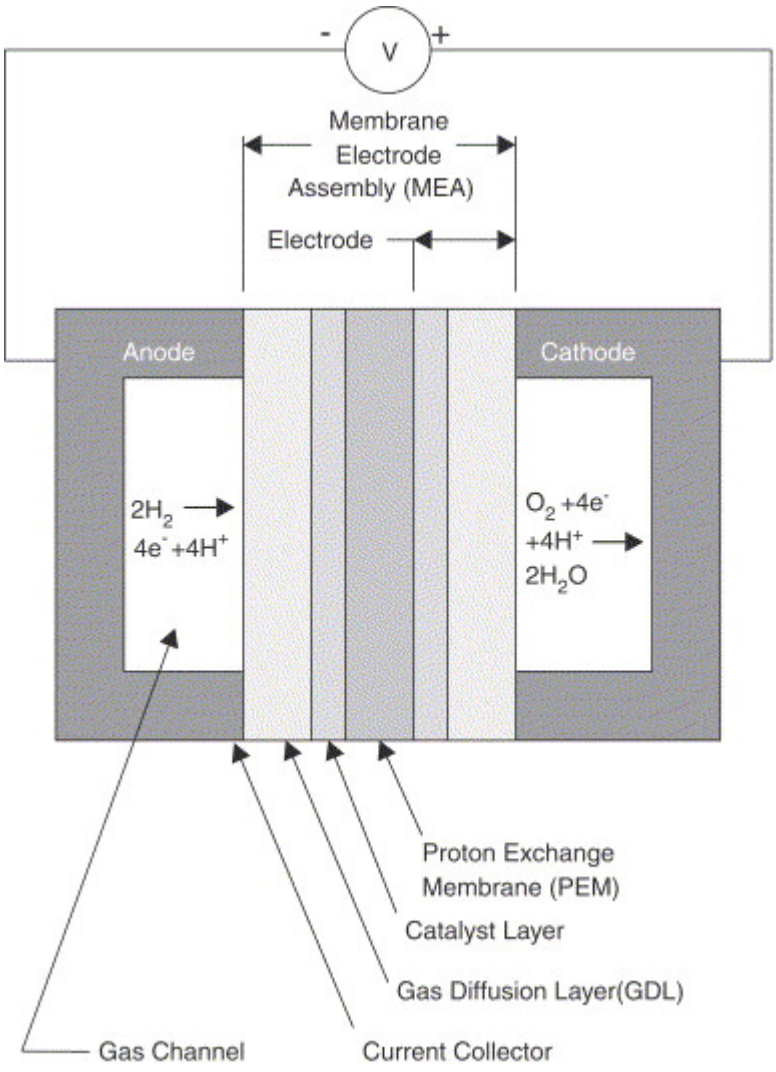


**Figure 1 - Structure of a fuel cell stack [5]**

### 2.1.1. Bipolar Plate

The main functions of bipolar plates include: conduction of electrons between adjacent cells, distribution of gas flow and to provide structural support for the stack. These plates are often fabricated from graphite, metal or electrically conductive polymer plastics. In recent years the cost of manufacturing bipolar plates has been drastically reduced [6]. A major factor in this cost reduction is the migration from machined graphite to injection-moulded polymer plates.

### 2.1.2. Diffusion media

The diffusion media is a material layer within the fuel cell which is intended to improve gas distribution within the cell as well as facilitate electrical contact between the electrode and the bipolar plate. This layer is important for the removal of excess water from the membrane surface. This layer is often produced from hydrophobic porous carbon paper. In many cases the hydrophobocity of the media is imparted by a polytetrafluoroethylene (PTFE) treatment.

### 2.1.3. Micro-porous Layer

The micro-porous layer (MPL) is a highly hydrophobic layer added between the gas diffusion media and the catalyst layer. This hydrophobic behaviour is imparted by PTFE contained within the layer itself. Gostick et al. suggests that the presence of this hydrophobic MPL can improve fuel cell performance by reducing the diffusion media water saturation during fuel cell operation [7]. At high current densities, the addition of an MPL seems to promote water breakthrough in the diffusion media by simulating a single-point injection into the diffusion media surface. This phenomenon is illustrated in Figure 2 originally presented by Gostick et al.

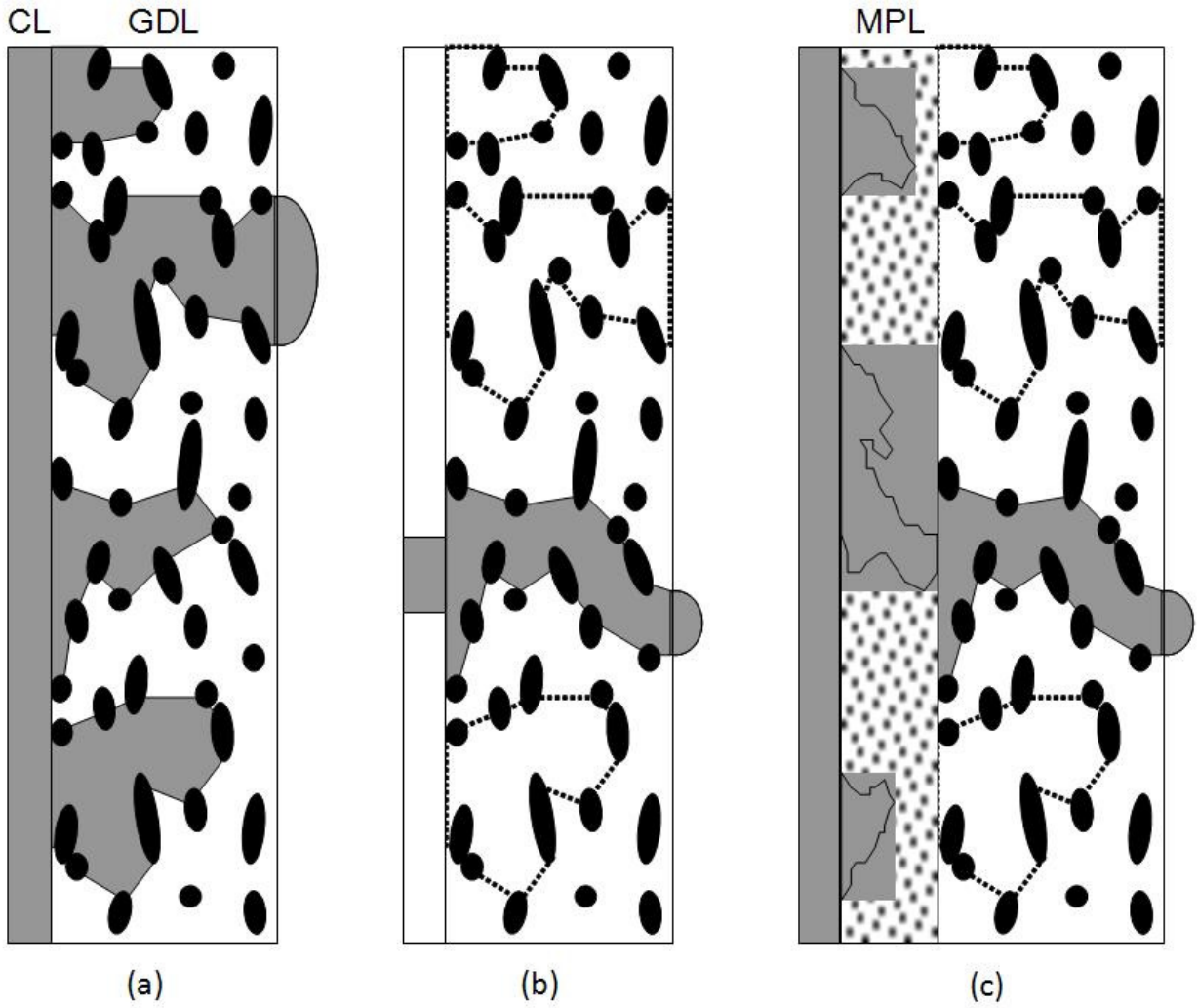


**Figure 2 - Micro-porous layer effect on GDM water saturation [7]**

Note that in Figure 2(a), a hypothetical fuel cell is illustrated in which the catalyst layer (CL) is in direct contact with the diffusion media (GDM). Liquid water is generated uniformly across the surface of the GDM and as such several pores fill with water before an exit point is found. Figure 2 (b) demonstrates that for a GDM for which water is injected at a single point, only that particular pore will fill with water while the remaining pores remain open and available for gas transport. Finally Figure 2 (c) shows how the presence of a micro-porous layer (MPL) ensures that only a single pore is filled with water despite a uniform liquid water film generated by the CL on the left-hand side of the figure. This phenomenon is important to the operation of PEMFCs as it can increase the overall gas-phase mass transport through the GDM while ensuring that the liquid water generated in the catalyst layer can be ejected from the cell.

### 2.1.4. Membrane

The primary function of the membrane is to transport protons generated at the anode to the cathode side where they react with oxygen to produce water. A fuel cell membrane must also provide a physical barrier between the anode and cathode side gas streams as well as electrically insulate the two electrodes to prevent short-circuiting of the cell. Perfluoronated sulphonic acid (PFSA) membranes are often employed as they exhibit a resistance to chemical degradation as well as low gas transfer rates. PFSA membranes are also able to conduct protons while resisting electron transfer.

### 2.1.5. Catalyst

Catalyst layers are found both on the anode side of the membrane, as well as the cathode side. The catalyst layers not only promote the two reactions mentioned previously but also provide the electrical pathway for the electrons to leave the reaction site. The catalyst layer typically consists of platinum supported by carbon structures and is applied directly to the membrane surface.

## 2.2. Factors affecting PEMFC Performance

The scientifically accepted method of presenting fuel cell performance data is the polarization curve. This curve presents cell voltage (V) on the Y-axis and current density ($mA \cdot cm^{-2}$) on the X-axis. Figure 3 presents an illustration of an example polarization curve presented by Huizing et al.[8]. Note the three regions in which distinct chemical processes dominate the fuel cell voltage losses. These three processes are presented in Equations 5 through 7.

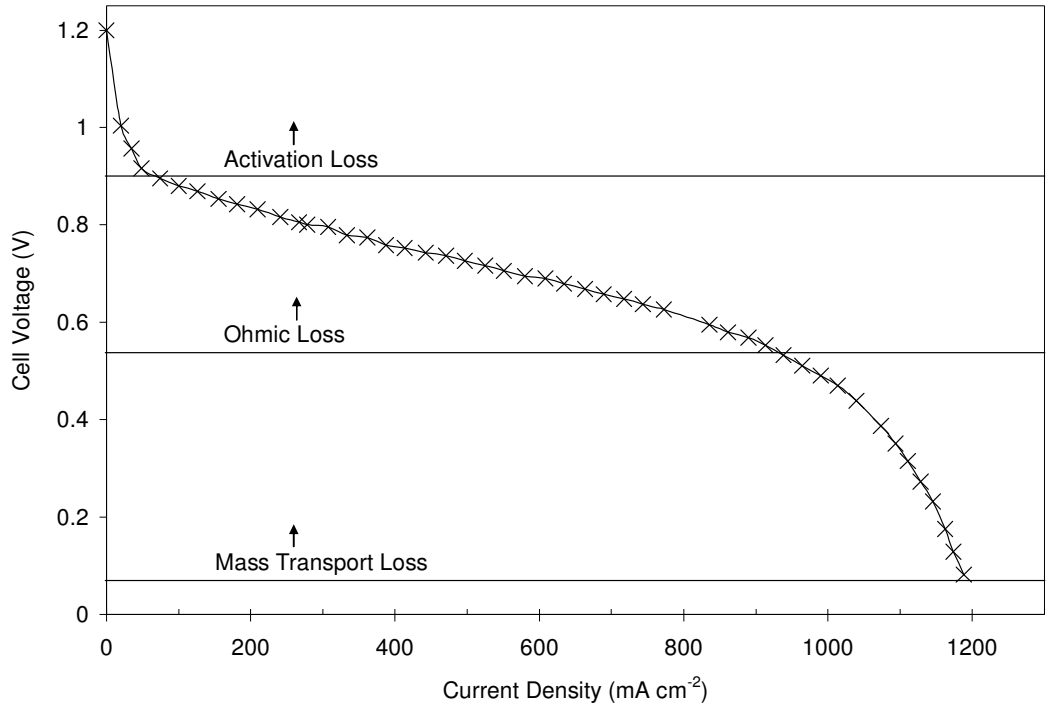


**Figure 3 - Example fuel cell polarization curve [8]**

## 2.3. Primary Losses

The three regions illustrated in Figure 3 are characterized by different reaction limitations. The following sections will introduce these limitations.

### 2.3.1. Activation Losses

The movement of electrons within the external circuit must be driven by a difference of potential between the anode and the cathode. Activation losses of potential dominate at low current densities and can be described by the Tafel or Butler-Volmer equations [9]. The source of the activation losses lies in the fuel cell half-cell reactions presented in Section 1. The Butler-Volmer equation is presented below:

$$i = i_o \left\{ exp\left(-\alpha \frac{zF}{RT} \Delta\eta_{act}\right) - exp\left((1-\alpha)\frac{zF}{RT}\Delta\eta_{act}\right)\right\} \quad \text{(Eq5)}$$

where i represents the fuel cell current density, $i_0$ is the exchange current density, α is a charge transfer coefficient, z is the number of electrons transported for the reaction, F is the Faraday's constant, R is the universal gas constant, T is the temperature and $n_{act}$ is the activation

overpotential. Under positive voltage the exponential term on the left becomes unity over an exponential term. At fuel cell operational voltages this term becomes negligible and the overpotential can be described by a Tafel relationship:

$$\Delta\eta_{act} = \beta ln\left(\frac{i}{i_o}\right) \quad \text{(Eq6)}$$

The activation overpotential will decrease as temperature, reactant concentrations, pressure or catalyst area increase. This loss dominates at low current densities and describes the very rapid drop in cell voltage at the left-hand side of Figure 3.

### 2.3.2. Ohmic Losses

The central region is characterized by a linear trend, in which the dominant effect is an ohmic resistance to electron and proton movement. Electrical resistances of the gas diffusion medium, bipolar plates as well as the external circuit are subject to Ohm's Law behaviour. The resistance to proton conduction through the electrolyte also exhibits a linear trend that can be described by Ohm's Law:

$$\Delta\eta_{ohmic} = I * R \quad \text{(Eq7)}$$

Ohm's law states that the voltage loss ($\eta_{ohmic}$) is the product of the current through the system (I) and the resistance to electron/proton movement (R). R is a function of both electron and proton flow, but can be separated into a linear combination of individual resistance sources:

$$R = r_{ionic} + r_{electrical} + r_{contact} \quad \text{(Eq8)}$$

As seen in Figure 3, for the majority of current densities the ionic resistance is the dominant resistance, and the moderate current density section of the polarization curve will exhibit a linear trend due to the linear nature of Ohm's Law.

### 2.3.3. Mass Transport Losses

The rapid loss in voltage at high current densities is caused by mass transport limitations. As the current density increases, it follows that the rate of chemical reaction that produces the electrons must also increase. At very high current densities the rate of reaction reaches the rate at which reactants can be supplied to the catalytic sites. At this point the local concentration of reactants

in contact with the catalyst decreases and the overall voltage also decreases. An empirical equation to describe these mass transport losses has been presented [10]:

$$\Delta\eta_{trans} = m * exp(n * i) \quad \text{(Eq9)}$$

Where $\eta_{trans}$ represents the mass transport overpotential, m and n are fitting coefficients, and i is current density. This exponential increase in potential loss affects the polarization curve at high current densities and describes the voltage drop above 1000 $mA \cdot cm^{-2}$.

#### 2.3.4. Overall Loss Relationship

Once these three major sources of voltage loss are quantified, they can be combined into a general equation that can be used to predict the overall voltage of a particular fuel cell, $V_{cell}$ ([11],[12]).

$$V_{cell} = E_O - \eta_{act} - \eta_{ohmic} - \eta_{trans} \quad \text{(Eq10)}$$

$$V_{cell} = E_o - \beta ln\left(\frac{i}{i_o}\right) - iR - m * exp(n * i) \quad \text{(Eq11)}$$

Where $E_o$ represents the open circuit voltage (OCV). A simplified representation of the OCV, in which the oxygen reduction reaction limits the overall reaction rate, was suggested [13]:

$$E_o = E_r + 2.303\frac{RT}{\alpha F} log(i_o) \quad \text{(Eq12)}$$

This equation follows the form of the Nerst equation for the determination of the voltage within an electrochemical cell.

## 2.4. Fuel cell Hydration

As stated in Section 1 it should be noted that reactant stream hydration plays a critical part in PEM fuel cell performance. Insufficiently controlled humidification of the reactants can also adversely affect the operational lifetime of PEMFC membranes. As membrane water content increases, the membrane will tend to swell due to the expansion of hydrophilic pathways within the membrane structure. Uneven swelling results in physical stresses acting upon the membrane itself which can lead to point failures or tears in the membrane. In order to optimize both fuel cell stack performance as well as operational lifetime the reactant steam humidity levels must be

carefully controlled at a high enough level to minimize ohmic losses within the membrane while not exceeding the level in which flooding can occur.

### 2.4.1. Membrane Structure

As was presented in Section 2.1.3 PEM fuel cells often use a PFSA membrane. One commercial product, Nafion™ has been particularly popular in fuel cell development. The monomer component of PFSA membranes is produced by perfluorination of polyethylene to produce polytetrafluoroethylene (PTFE). PTFE, or Teflon, is used due to the fact that the strong C-F bonds produce a highly stable and chemically resistant framework for the membrane. At this point the monomers are treated in order to introduce fluorinated side-chains that contain a sulphonic acid ($HSO_3$) group. The generic polymer molecule is illustrated below in Figure 4. Note that the values of n, m and x are heavily dependent on the exact PFSA material under consideration.

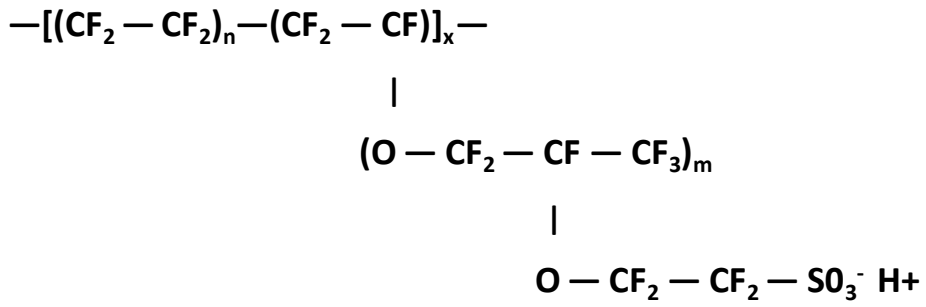


**Figure 4 - Basic PFSA structure**

The sulphonic acid group provides the ability for this polymer to conduct protons. The group itself is hydrophilic and the hydrogen molecule is highly mobile while the fluorinated backbone is highly hydrophobic. In the presence of water the membrane will segregate itself at the nano-scale producing hydrophobic and hydrophilic regions as shown in Figure 5.

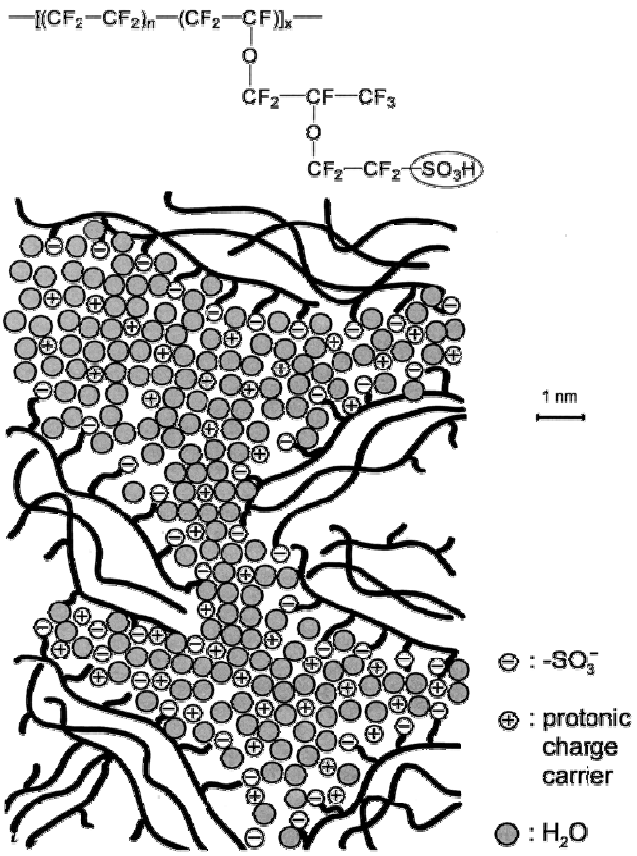


**Figure 5 - Hydrophilic pathways within PFSA [14]**

The hydrophilic pathways shown in the above figure allow water and hydronium ions to be transported across the membrane while the hydrophobic clusters provide physical support that resists gas crossover.

### 2.4.2. Effect of Humidification

Section 2.4.1 presented the concept of hydrophilic pathways in which proton transfer can take place. The degree of humidification is often presented through the factor λ, which is the ratio of water molecules to $SO_3^-$ functional groups. The minimum ratio for proper fuel cell performance is around six while a fully humidified membrane λ ratio will approach 22 for cells at 25°C [15]. Zawodzinski et al. developed an empirical equation to relate membrane water content to the vapour phase water activity [16].

$$\lambda = 0.043 + 17.81a_W - 39.85a_W^2 + 36.0a_W^3 \quad \text{(Eq13)}$$

Where vapour phase water activity can be calculated according to Equation 14.

$$a_w = \frac{P_W}{P_W^*(T)} \quad \text{(Eq14)}$$

Where $P_W$*is the saturated vapour pressure at T.

Supposing that gas phase humidity levels decrease the membrane humidification would also decrease resulting in the situation where the conductivity of these hydrophilic pathways also decreases. This loss of conductivity is caused by a dissociation of the $SO_3^-$ - $H_2O$ clusters which hinders the transfer of protons through the hydrophilic membrane pathways. As observed by Buchi et al. this decreased conductivity leads to an overall increase in Ohmic losses within the cell and thus, decreased fuel cell performance [17]. Figure 6 presents polarization curves from both a humidified and a non-humidified fuel cell.

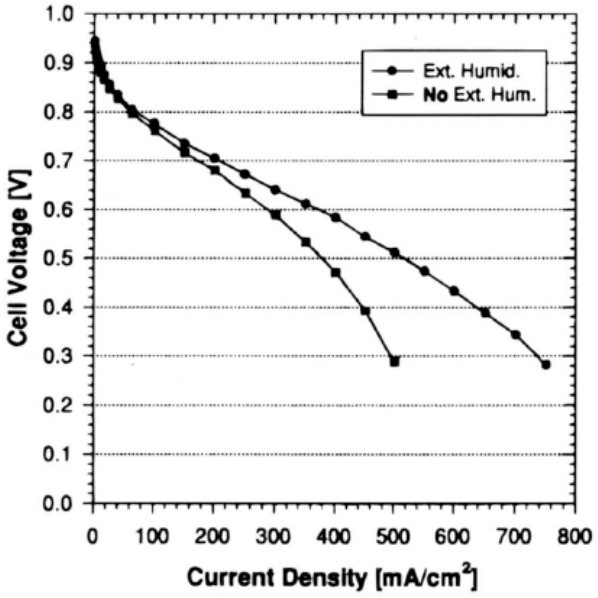


**Figure 6 - Fuel cell performance with and without humidification [17]**

In addition to decreased performance, insufficiently humidified fuel cells will also experience decreased performance as well as an increased failure rate. A fuel cell stack operated under insufficiently humidified conditions will experience significantly increased ohmic losses caused by constriction of the ion transport pathways illustrated in Figure 5. In order to minimize ohmic resistance to mass transfer a PFSA membrane must be saturated with water. Improper humidification can also significantly affect the operational life-time of the fuel cell stack. If the membrane is not uniformly humidified, proton conductivity will also be non-uniform. In these

situations, the hydronium ions are preferentially transported along the high humidity pathways resulting in a localized area of high current which accelerates membrane degradation. These regions of increased current will also increase in temperature affecting the region's local humidity. Non-uniform membrane hydration will also impart mechanical stresses on the membrane as it expands in the presence of water. These mechanical stresses will have a deleterious effect on the membrane operational lifetime as they can lead to membrane pinholes or, in extreme cases, membrane tearing.

Excess humidification of the inlet streams will also present a problem if liquid water condenses or "floods" the cell. Condensation can impede oxygen transport to the cathode by blocking pores in the GDM as well as by inhibiting air flow through the bipolar plate flow channels. Both these factors will strongly affect the fuel cell performance at high current densities due to their effect on the mass transport losses. Figure 7 presents the polarization curves generated by Yoon et al. for several situations [18].

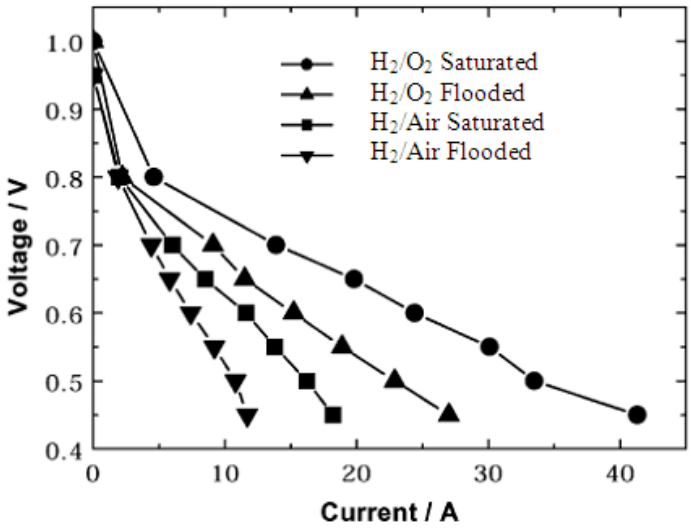


**Figure 7 - Effect of flooding on fuel cell performance [19]**

## 2.5. Fuel cell mass balances

The primary scope of this section is not to engage a full mass balance but instead focus on the water flows within the fuel cell system. There are four primary mechanisms by which water transport takes place: electro-osmotic drag, diffusion, generation, and humidification.

### 2.5.1. Electro-Osmotic Drag

As discussed in Section 2.4.1, the protons are transported across the membrane by ion diffusion. These protons are stabilized by a cluster of water molecules which move with the proton from anode to cathode [20]. The number of water molecules transported per proton is referred to as the electro-osmotic drag coefficient ($N_{w,drag}$). Vapour-equilibrated Nafion™ 117 membranes were shown to perform at electro-osmotic drag coefficients between 1 and 1.4 for situations in which the membrane water content ($\lambda$) was equal to eleven [21]. It was further observed that a membrane equilibrated with liquid water at 25°C, equivalent to a water content of 22, demonstrated an electro-osmotic drag coefficient between 2.5 and 2.9 [16]. It has been suggested that the transport rate of water attributed to electro-osmotic drag can be described by the following relationship:

$$N_{w,drag} = n_{drag}\left(\frac{2*I}{F}\right) \quad \text{(Eq15)}$$

In which $n_{drag}$ is a coefficient linearly proportional to the water content of the membrane and is expressed in Equation 16 and F is the Faraday constant.

$$n_{drag} = \frac{2.5}{22}\lambda \quad \text{(Eq16)}$$

The factor, $\lambda$ corresponds to the $H_2O/SO_3^-$ ratio within the membrane.

### 2.5.2. Diffusion

During fuel cell operation a water concentration gradient across the membrane drives a diffusion mechanism of water transport. The diffusion of water can be described by Fick's Law:

$$N_{w,diff} = D_W \frac{dc_w}{dy} \quad \text{(Eq17)}$$

In Equation 17 $N_{w,diff}$ represents the molar diffusion rate of water, $D_w$ is the diffusion coefficient of water through the membrane, $c_w$ is the water concentration and y is the through-plane depth.

The simplest representation of the diffusion equation is when the membrane diffusion coefficient does not vary with membrane water content. This diffusion statement is presented below in Equation 18.

$$N_{w,diff} = D_W \frac{(c_{cath} - c_{anod})}{\delta_m} \quad \text{(Eq18)}$$

In Equation 18 $c_{cath}$ and $c_{anod}$ represent the membrane surface water concentrations while $\delta_m$ represents the overall membrane thickness.

Section 2.9.5 presents the analysis method suggested by Motupally which is used in this project. This method fundamentally represents Fickian diffusion however the integration limits are converted to membrane surface water contents (λ).

### 2.5.3. Electrochemical Generation

A significant portion of the water in a PEMFC is generated at the cathode by the electrochemical reaction expressed in Equation 19. The rate of water generation can be estimated by converting the overall system current into a molar rate.

$$N_{generation} = \frac{I}{2F} \quad \text{(Eq19)}$$

Where 'I' represents the system current in amperes, F represents Faraday's constant and the 2 represents the two electrons consumed per mol of water produced.

### 2.5.4. Humidification

The fourth source of water transport in the fuel cell is the water content carried by the reactant gas streams. The amount of water vapour contained by the cathode and anode inlet streams is one of the most straight-forward ways to control humidification within the fuel cell itself. Proper humidification of these streams contributes strongly to optimal fuel cell performance. The amount of humidification required relies not only on the cell temperature but also upon the power demand. Higher current densities generate more water at the cathode and the cell could flood if the inlet gases are too humid. The controlled factor in fuel cell water management systems is the relative humidity of the inlet streams. Relative humidity can be calculated though the use of the following relationship:

$$RH = \frac{P_w}{P_{sat}} * 100 \quad \text{(Eq20)}$$

There are several methods to determine the saturated water vapour pressure from Equation 20 including equations of state such as the Wagner equation [22].

$$ln(P_{vpr}) = \frac{A(1-T_r)+B(1-T_r)^{1.5}+C(1-T_r)^3+D(1-T_r)^6}{T_r} \quad \text{(Eq21)}$$

Where $P_{vpr}$ is the reduced vapour pressure and is calculated as shown in Equation 22.

$$P_{vpr} = \frac{P_{sat}}{P_c} \quad \text{(Eq22)}$$

And where $T_r$ is the reduced temperature.

$$T_r = \frac{T}{T_c} \quad \text{(Eq23)}$$

The saturated water vapour pressure can be calculated for the water-air system by using the Wagner coefficients presented in Table 1 [23].

**Table 1 - Water-air system Wagner coefficients [23]**

| Coefficient | Value |
|---|---|
| A | -7.775 |
| B | 1.466 |
| C | -2.771 |
| D | -1.317 |
| $T_c$ | 647.31 |
| $\ln(P_c)$ | 10.003 |

An alternative method is interpolation of vapour pressure data taken from a source such as Perry's Chemical Engineering Handbook [24]. This method is acceptable for quick calculations however for a major computational program such as this thesis project the Wagner method is both more accurate and less computationally intensive. Example vapour pressure data can be found below in Table 2.

**Table 2 - Example set of water vapour pressure [24]**

| Temperature (K) | $H_2O$ Vapour Pressure (kPa) |
|---|---|
| 273.16 | 0.612 |
| 280.00 | 0.992 |
| 290.00 | 1.920 |
| 300.00 | 3.537 |
| 310.00 | 6.231 |
| 320.00 | 10.546 |
| 330.00 | 17.213 |
| 340.00 | 27.188 |
| 350.00 | 41.682 |
| 360.00 | 62.194 |
| 370.00 | 90.535 |
| 380.00 | 128.85 |

The specific humidity is another property and can be found by using Equation 24.

$$\omega = \frac{m_w}{m_{air}} \quad \text{(Eq24)}$$

Where $m_w$ is the mass of water per unit volume and $m_{air}$ is the mass of air per unit volume. By using the ideal gas law and assuming a cathode gas stream of air and water only, the following relationship between water partial pressure and specific humidity can be made:

$$\omega = \frac{P_w * M_w}{(P_{Total} - P_w) * M_{air}} \quad \text{(Eq25)}$$

In order to calculate the mass flow requirement of water to be added to the cathode stream, one must first determine the rate at which air is fed to the fuel cell. Assuming the desired current provided by the fuel cell is known, the flow rate of oxygen required can be determined by the use of Equation 26:

$$N_{O2} = \frac{I*\chi}{4*F} \quad \text{(Eq26)}$$

In which $\chi$ represents the number of cells in the fuel cell stack. Once the oxygen demand is calculated, an elementary calculation can be performed to find the overall air demand. Equation 27 assumes nominal oxygen content of 21% by volume.

$$N_{air} = \Psi * \frac{N_{O2}}{0.21} \quad \text{(Eq27)}$$

Where $\Psi$ is referred to as the stoichiometry, or a factor of excess air flow to remove contaminants and improve fuel cell performance.

### 2.5.5. Cell Water Balance

The previously stated mass transfer relationships for the water content can be combined to describe the overall situation within the fuel cell. As stated it is undesirable to run the fuel cell under drying or flooding conditions as these situations can adversely affect the operational lifetime or reduce the overall performance of the stack. In order to maintain the water balance for both the anode and cathode these streams must be humidified to an appropriate level before being fed to the fuel cell stack.

An overall fuel cell stack analysis was performed by Merida et al. where the fuel cell stoichiometry, temperature and pressure were compared with the water content of the stack. As seen in Figure 8, the fuel cell experiences drying conditions for nearly all conditions in excess of 60°C [25]. As Section 2.3.1 demonstrates, activation losses are minimized as stack temperature is increased. Clearly in order to maximize fuel cell efficiency the stack must be operated above 60°C and the reactant streams must be humidified to offset the drying conditions within the cells.

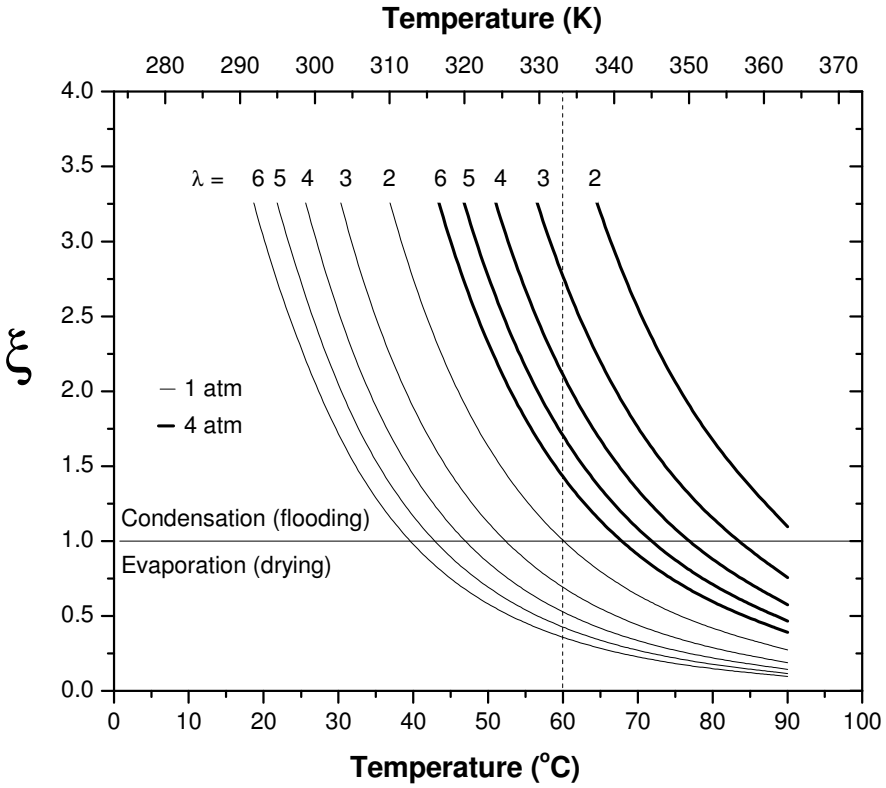


**Figure 8 - Fuel cell water content based on temperature, pressure and stoichiometry [25]**

## 2.6. Humidification Processes

Section 2.5 has established that based on current technology the majority of fuel cell systems must have some method of humidifying the incoming reactant streams. This section covers several technologies and concepts for maintaining an adequate humidity level for fuel cell stacks.

There are two primary modes in which fuel cell systems can be humidified. Internal humidification refers to methods in which water is added directly to the cells or product water is retained within the stack. External humidification refers to processes in which inlet gas streams are humidified prior to entering the fuel cell stack.

The amount of water produced within the fuel cell is sufficient to properly humidify the stack, as illustrated below in Figure 9 by Huizing et al. [8]. This product water is not, however, able to humidify the system without either an external or internal humidification system. A "closed-loop" external humidification system must transfer water from the cathode exhaust to the inlet streams in order to prevent the problems presented in Section 2.4.2.

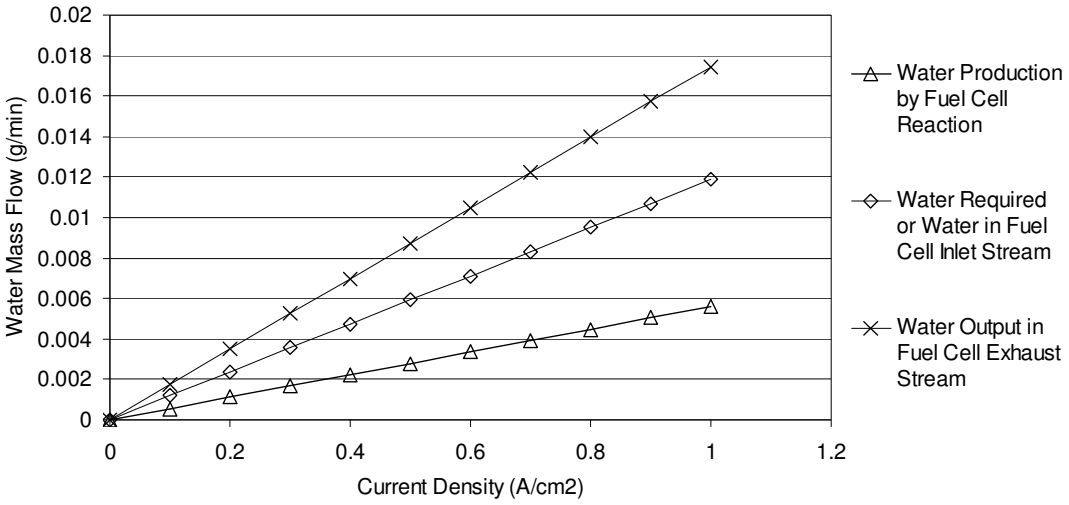


**Figure 9 - Mass transfer paths in a PEMFC [8]**

Research has indicated that humidifying both anode and cathode inlet streams may not be necessary under certain conditions, as a system without cathode humidification but a fully saturated anode stream experiences a 5% performance decrease at 400 mA $cm^{-2}$. It has also been suggested that a fully humidified cathode inlet may result in flooding [26]. Williams suggests that a partially humidified cathode stream (75-90% RH) would result in improved fuel cell performance.

## 2.7. Internal Humidification

### 2.7.1. Stack-Integrated Humidifiers

One of the most straightforward methods of internal humidification is the integration of membrane humidifiers within in the fuel cell stack itself in a series arrangement [27]. In this design cooling water also passes by one side of the membrane humidifier, thereby humidifying the inlet gases. This method considerably simplifies the fuel cell system in terms of packaging but also introduces several significant drawbacks. These drawbacks include depletion of the cooling system water as well as coupling the stack and humidifier temperatures.

Another integrated humidifier, suggested by Santis et al. [28], involves extending the PFSA membrane in order to include a humidification section within each cell. Unfortunately this method considerably increases cell complexity and requires considerably more PFSA material per stack.

### 2.7.2. Steam or Liquid Water Injection

Wood et al. proposed a system in which liquid water is injected directly into the cells [29]. The performance of each individual cell benefits considerably from this method of humidification however it does introduce significant parasitic losses resulting from both the pumping and heating of the liquid water. The overall system complexity also increases, as the cells must be modified and additional hardware is required.

### 2.7.3. Alternate Membrane Chemistry

Significant research has been put forth to develop novel membrane materials that either retain or generate additional humidity within the cell ([30], [31], [32], [33],[34]). Metal oxides such as $TiO_2$ and $SiO_2$ promote the retention of water within the membrane. Small amounts of platinum impregnated within the membrane will catalyze any $O_2$ and $H_2$ diffusing through the membrane, generating additional liquid water within the membrane itself [35].

The drawbacks of these methods are that the effects imparted by additives are static, and cannot be adjusted under transient conditions. For example these additives will improve fuel cell performance at low current densities where fuel cell humidity can be quite low. At higher current densities, however, these additives would increase the likelihood of cathode flooding.

Research into integrating a layer of carbon nano-tubes (CNTs) in the membranes enables the fuel cell to run without any humidification for either reactant stream [36]. This membrane consists of a layer of CNT/Nafion™ dispersion sandwiched between two traditional Nafion™ membranes. It was suggested that overall mechanical strength would also benefit from this non-traditional layer. The inner layer of CNTs improves dry reactant performance by enabling the catalytic combination of oxygen and hydrogen to generate water within the membrane itself. The research group indicated that the addition of the CNT layer improved dry reactant performance by 25% over a traditional PFSA membrane.

Research into alternative materials within the catalyst layer has also been done. Han et al. suggested that addition of silica to the catalyst layer can improve performance when the anode stream is not humidified [37]. It was found that the optimal silica loading was 6% by weight for the self-humidified anode fuel cell.

Investigation of gas diffusion media conducted by Gostick et al. suggests that the presence of a micro-porous layer can reduce the water saturation required for liquid water breakthrough [7]. Lower water saturation within the gas diffusion media at liquid breakthrough will reduce gas-phase mass transfer resistance while allowing liquid water to be removed from the membrane surface.

### 2.7.4. Passive water distribution

The addition of hydrophilic wicks has been shown to improve fuel cell performance. These wicks draw liquid from an external reservoir into the cell. This passive system has an advantage in that low-humidity regions will preferentially take up water due to the increased driving force. A significant disadvantage is that this system complicates the sealing and assembly of the fuel cell stack.

Ge et al. reported an increase in fuel cell performance when absorbent sponges were added to the bipolar plate flow fields [38]. Similar to the hydrophilic wicks previously mentioned this passive system promotes redistribution of liquid water within the cell whereby water can be transported away from regions of high water content, such as the flow field outlets.

Another method of passive water distribution was to use porous bipolar plates. These highly porous plates tend to absorb liquid water produced within the cell and distribute it to low-humidity regions. Much like the previous two systems, this system tends to impart a degree of self-regulation within the cell but can impact performance at high current densities if water removal from the stack is impeded. Research indicates that at a stoichiometric ratio of 1.3 an experimental porous plate design produced 3.5 times the amount of power than a fuel cell with non-porous plates [39]. A second type of alternative bipolar plate contains capillary pipelines to transport water from the cathode to the anode [40].

## 2.8. External Humidification

### 2.8.1. Sparging Systems

These systems are characterized by a column in which air is bubbled through heated liquid water. Humidity is a function of water temperature, liquid-gas contact area and residence time [41]. These properties can be easily controlled by adjusting bubble size, column length and water

temperature. This method is well-known and the technology is mature but using these systems in commercial systems is impractical due to several reasons.

One such reason is that the liquid water contained in these columns must be maintained, which is not practical in most commercial applications. Parasitic losses observed by utilizing this method are high as the water temperature must be maintained and gas pressure loss through the column can be very significant [42].

### 2.8.2. Enthalpy Wheel

Enthalpy wheel systems operate by passing inlet gases through a humidified honeycombed ceramic. This ceramic wheel rotates within the humidifier unit and is humidified by the fuel cell outlet stream. This system does not require an external water source as water demand is met by using the fuel cell outlet stream. Heat duty for the inlet gases can also be reduced if heat from the outlet streams is captured. While parasitic losses are small the system does have a significant lag time which can impair performance under transient conditions. The system is illustrated below in Figure 10.

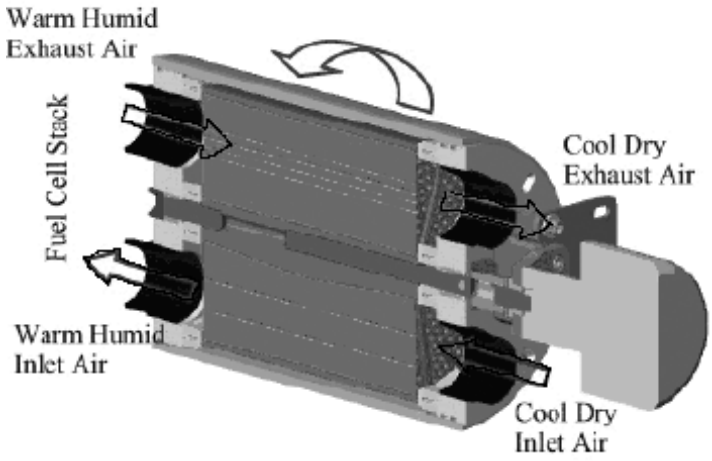


**Figure 10 - Enthalpy wheel humidifier**

### 2.8.3. Membrane Humidifiers

The component of interest in these systems is the hydrophilic polymer membranes used to transfer water from one stream to another. Similar to the enthalpy wheel, these systems can use

water from the fuel cell cathode outlet and do not require any external water sources. Traditional membrane system designs can be used; both tubular and planar designs are feasible.

Tubular designs often closely resemble shell-and-tube heat exchangers and benefit from the considerable engineering knowledge already in place for those systems. The fuel cell cathode exhaust is passed through the small hollow membrane tubes while the inlet air stream fed to the shell side. An advantage of this system lies in the usage of a large surface area while maintaining a low pressure drop on the fuel cell inlet stream. Minimizing the outlet stream pressure drop is not as important as the fuel cell stack is often pressurized to increase reaction kinetics. These systems suffer from a complex assembly process as well as an expensive manufacturing process to produce the tubular membranes. Figure 11 illustrates an example of a shell-and-tube membrane humidifier proposed by Tanaka et al.[43].

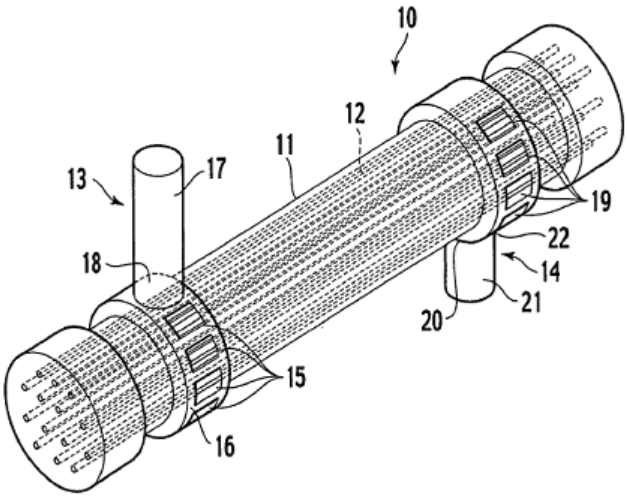


**Figure 11 - Shell-and-tube membrane humidifier [43]**

where the labelled components are as listed in Table 3 below.

**Table 3 - Shell and Tube Components**

| Component | Function |
|---|---|
| 10 | Hollow-fiber membrane module |
| 11 | Vent pipe |
| 12 | Hollow-fibre membrane |
| 13 | Distributing mechanism |

| | |
|---|---|
| 14 | Distributing mechanism |
| 15 | Vent Holes |
| 16 | Distributor |
| 17 | Gas Conduit |
| 18 | Connection Hole |
| 19 | Vent Holes |
| 20 | Distributor |
| 21 | Gas Conduit |
| 22 | Connection Hole |

Planar designs resemble plate-and-frame heat exchangers and benefit from a reasonably simple assembly process. Streams travel in a counter-current or cross-current manner and transfer both heat and humidity from the cathode outlet stream to the inlet streams. The hydrophilic membrane separating the two streams is selected such that both heat and water transfer are maximized while gas transfer is minimized, much like the fuel cell membrane itself. The chemical stability required in the fuel cell membrane is less important for the humidifier units. While designs often contain PFSA membranes, lower-cost alternatives are also being investigated. Several patents are available which detail plate-and-frame membrane humidifiers. An example design is shown in Figure 12.

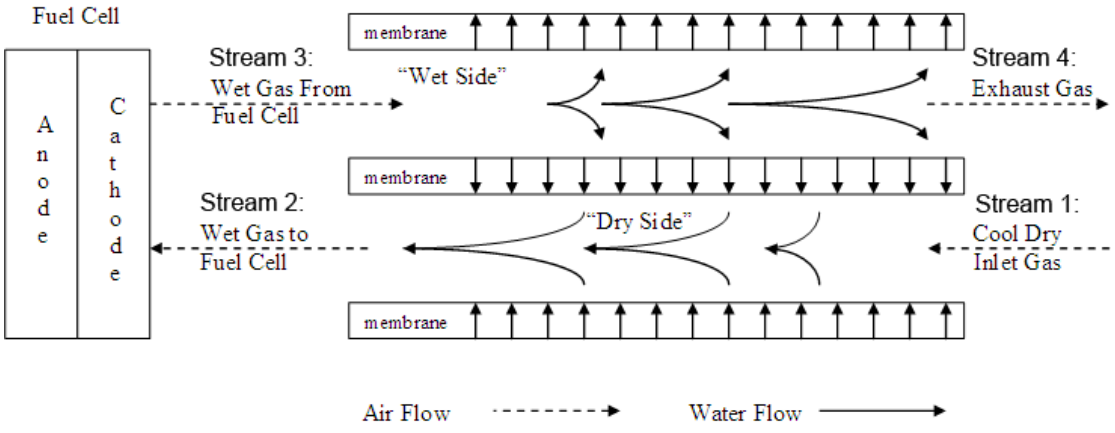


**Figure 12 - Gas and liquid streams in a planar humidifier**

## 2.9. Fuel Cell and Humidifier Modeling

In many cases, the techniques used to model a PEM fuel cell can also be applied to humidifier modeling. While fuel cell models must account for electrode potentials and redox reactions that do not exist in a humidifier, the complicated methods for modeling two-phase flow and partially wetting diffusion media are common to both.

One modeling project presented by Zhong et al. in 2006 suggests the use of a support vector machine (SVM) can be used to predict fuel cell performance. SVMs are a regression technique that can be "trained" by inputting appropriate data [44]. The key limitation of this work is that the model calculates voltage using current density and temperature but leaves other key parameters such as partial pressure and membrane hydration as constants. Another factor to consider is that the model results are highly dependent on the data used to train the model, fundamental heat and mass transfer relationships are not considered.

### 2.9.1. PFSA in membrane humidifiers

It has been suggested that membrane humidifiers with a PFSA membrane may perform particularly well due to low gas transfer and high water transfer properties. One paper presents a model for determining water transfer rate through five different types of PFSA membrane based on gas flow conditions at 60°C [45].

### 2.9.2. Two phase flow

A significant challenge in producing a robust model of either the fuel cell or the humidifier system is the two phase flow phenomenon in the gas diffusion media. In a fuel cell, water produced at the cathode-side membrane surface must be rejected to the cathode gas stream. The gas diffusion is often treated with PTFE to impart hydrophobocity however the membrane itself is quite hydrophilic. This hydrophilicity encourages the formation of liquid water on the surface of the membrane which must then be transported to the surface of the GDM. Excessive amounts of liquid water will block the pores in the GDM, limiting transport of gaseous oxygen from the cathode gas stream to the catalyzed membrane surface.

Existing empirical correlations for two phase flow are not reliable for use in GDMs as the correlations were obtained by using soil and sand samples whose structure differs significantly from the fibre mesh layout in GDMs [5].

### 2.9.3. System

The control of fuel cell humidifiers is a topic that has grown considerably in recent years. Significant work has been performed towards characterizing and optimizing humidifier systems at steady state however commercial vehicles will rely heavily on transient power demands. Several models have been developed which include model predictive control [46], integrated thermal/mass transfer models [47], and CFD analysis [48].

### 2.9.4. Diffusion Coefficient of water in a gas mixture

It can be seen that any attempt at modeling the performance of a fuel cell cathode humidifier requires a significant understanding of mass transfer. The methods used to determine the Fickian mass transfer coefficients for water through both the gas phase and through the membrane are discussed in this section.

Hirschfelder et al. [49] suggested that the diffusion coefficient for a component A through component B can be estimated by using Equation 28 provided the molecules are non-polar and non-reacting.

$$D_{AB} = \frac{0.001858T^{\frac{3}{2}}\left[\frac{1}{M_A}+\frac{1}{M_B}\right]^{0.5}}{P\sigma_{AB}^2\Omega_D} \quad \text{(Eq28)}$$

Where T is the absolute temperature in K, P is the absolute pressure in atm, $\sigma_{AB}$ is the collision diameter, $M_x$ is the component molar mass and $\Omega_D$ is the collision integral.

Brokaw suggested that this method can be expanded to include polar gases by evaluating the collision integral according to Equation 29 [50].

$$\Omega_D = \Omega_{D_0} + \frac{0.196\delta_{AB}^2}{T^*} \quad \text{(Eq29)}$$

Where

$$\delta_{AB} = (\delta_A\delta_B)^{0.5} \quad \text{(Eq30)}$$

$$\delta = \frac{1.94*10^3\mu_p^2}{V_bT_b} \quad \text{(Eq31)}$$

Where $\mu_p$ is the dipole moment (Debye), $V_b$ is the liquid molar volume ($cm^3\ g^{-1}\ mol^{-1}$) at its boiling point and $T_b$ is the normal boiling point (K).

$$T^* = \frac{\kappa T}{\varepsilon_{AB}} \quad \text{(Eq32)}$$

$$\frac{\varepsilon_{AB}}{\kappa} = \left(\frac{\varepsilon_A}{\kappa}\frac{\varepsilon_B}{\kappa}\right)^{0.5} \quad \text{(Eq33)}$$

$$\frac{\varepsilon_x}{\kappa} = 1.18(1 + 1.3\delta^2)T_b \quad \text{(Eq34)}$$

$$\Omega_{D_0} = \frac{A}{(T^*)^B} + \frac{C}{exp(DT^*)} + \frac{E}{exp(FT^*)} + \frac{G}{exp(HT^*)} \quad \text{(Eq35)}$$

Where

| | | | |
|---|---|---|---|
| A=1.06036 | B=0.15610 | C=0.19300 | D=0.47635 |
| E=1.03587 | F=1.52996 | G=1.76474 | H=3.89411 |

Equation 28 estimates the Fickian diffusion coefficient for a binary pair. To estimate the diffusion coefficient for a gas mixture, the following relationship can be used.

$$D_{1-mix} = \frac{1}{\frac{y'_2}{D_{1-2}} + \frac{y'_3}{D_{1-3}} + \cdots + \frac{y'_n}{D_{1-n}}} \quad \text{(Eq36)}$$

Where

$$y'_2 = \frac{y_2}{y_2 + y_3 + \cdots + y_n} = \frac{y_2}{1 - y_1} \quad \text{(Eq37)}$$

### 2.9.5. Diffusion of water in a PFSA membrane

Water flux through the humidifier membrane was estimated according to the method presented by Motupally et al. [15]. Equation 38 illustrates the relationship.

$$N_w = -\frac{\rho_M}{M_M \delta_M} \int_{\lambda_1}^{\lambda_2} D_{w,F} d\lambda \quad \text{(Eq38)}$$

Where $\rho_M$ is the membrane density ($g \cdot cm^{-3}$), $M_M$ is the molecular weight of the membrane ($g \cdot mol^{-1}$), $\delta_M$ is the membrane thickness, $D_{wF}$ is the Fickian diffusion coefficient ($cm^2 \cdot s^{-1}$) and $\lambda$ is the membrane water content.

Zawodzinski et al. [51] presented the following relationship between membrane $\lambda$ and the activity of the water vapour in contact with that membrane.

$$\lambda = 0.043 + 17.81a_W - 39.85a_W^2 + 36.0a_W^3 \quad \text{(Eq38)}$$

Motupally et al. reported that the final form of the Fickian diffusion coefficient, in terms of $\lambda$, was best described by the following piecewise relationship.

$$D_{w,F} = \begin{cases} 3.1 * 10^{-3}\lambda\left(-1 + e^{0.28\lambda}\right)exp\left(\frac{-2436}{T}\right), & 0 < \lambda < 3 \\ 4.17 * 10^{-4}\left(\lambda + 161e^{-\lambda}\right)exp\left(\frac{-2436}{T}\right), & 3 \leq \lambda < 17 \end{cases} \quad \text{(Eq39)}$$

## 2.10. PEM Fuel Cell Reactant Streams

The target conditions for fuel cell cathode and anode streams were presented by the U.S. Department of Energy (DoE) in 2007 [52]. Table 4 summarizes the target operating conditions for automotive fuel cells.

**Table 4 - Target fuel cell reactant stream conditions**

| Stream | Temperature (C) | Pressure (atm) | Relative Humidity |
|---|---|---|---|
| Cathode | 70-120 | 1-3 | 20-100% |
| Anode | 70-150 | 1-3 | 5-100% |

Note that temperatures above 100°C are targeted in order to aid thermal rejection as well as address complications arising from condensed water. The DoE has identified high-temperature, which is temperatures in excess of 90°C, polymer membranes as a key area of research.

# 3. Analysis Methodology

## 3.1. Experimental

The primary objective of this thesis project is to determine the water transfer performance of a prototype planar membrane fuel cell humidifier. The primary components of the experimental apparatus is illustrated below in Figure 13 and consists of a controlled evaporator-mixer (CEM), six pressure transmitters, three flow meters, three PID-controlled electric heaters, five thermocouples, two condensers, two water collection cylinders, and a small water reservoir (pressurized). This work also included the collection of data from a planar membrane humidifier designed and built by Dana Long Manufacturing however the design, test conditions, materials and data associated with this humidifier are not included as they remain confidential.

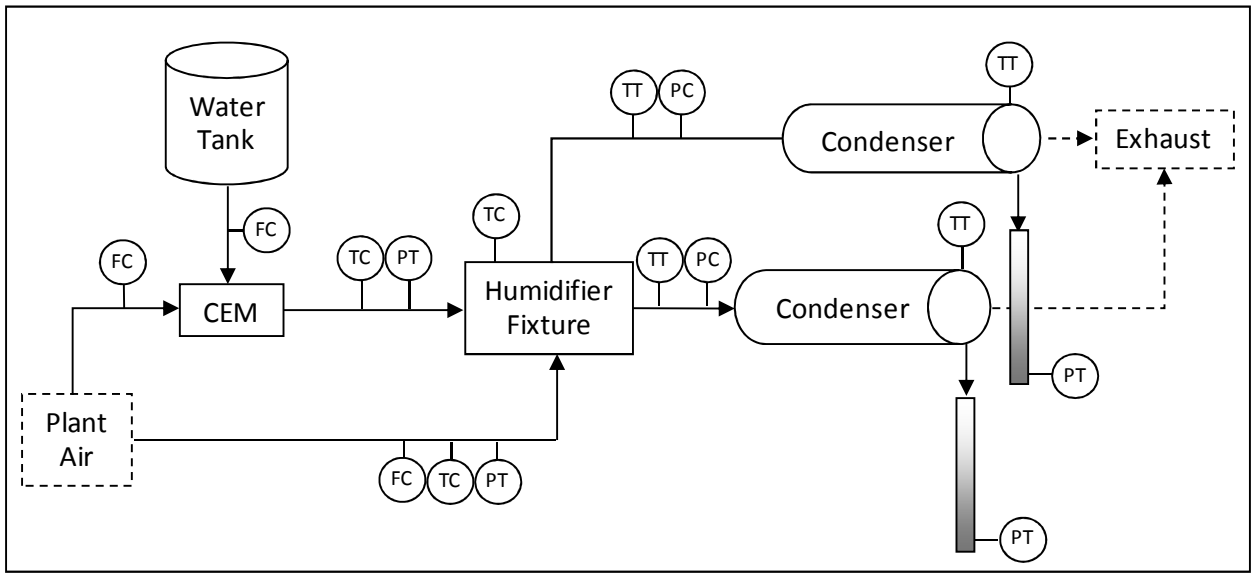


**Figure 13 - Simplified experimental apparatus**

Inlet gas temperatures are maintained through OmegaLUX rope heaters controlled through a LabVIEW PID controller. The humidifier fixture is heated by an OmegaLUX silicone heating blankets under PID control. Wet-inlet water content is maintained through a Bronkhorst CEM system connected to a Bronkhorst controller. The role of this CEM system is to simulate the temperature and humidity at the anode outlet of an automotive PEM fuel cell stack. The water injection rate and CEM operating temperature are specified through LabVIEW however they are controlled through the Bronkhorst controller. Liquid water is stored under a pressurized

atmosphere in a small steel cylinder before being fed through a mass flow controller leading to the CEM. The water injection system, humidifier fixture and CEM are visible in Figure 14.

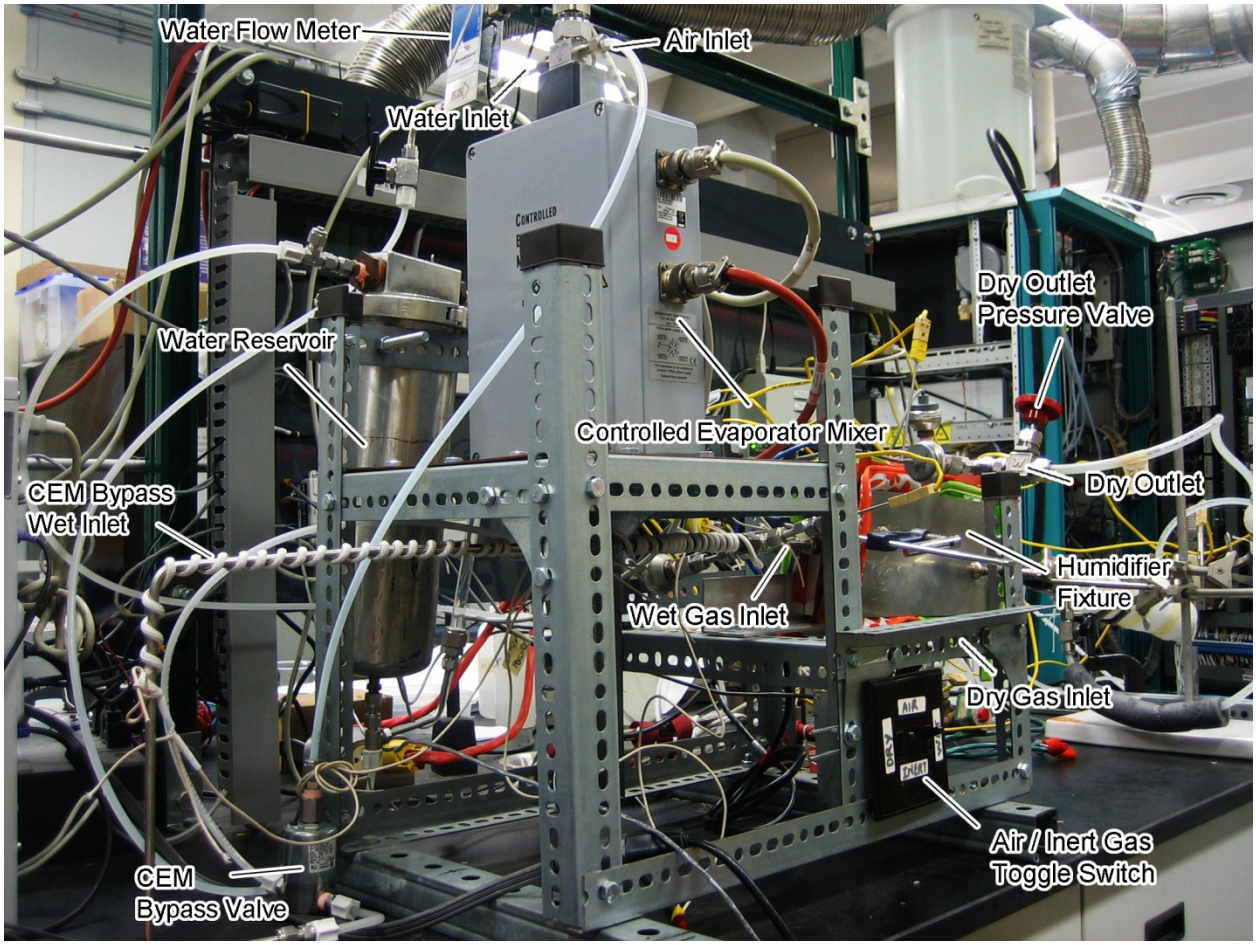


**Figure 14 - Apparatus: CEM and humidifier fixture**

Temperature and pressure data is collected through four National Instruments USB-6008 data acquisition units (DAQs) connected directly to a desktop computer via a USB connection. The list of data acquisition input channels are presented below in Table 5.

**Table 5 - Data acquisition input channels**

| **Device 1** | |
|---|---|
| Analog Input 0 | Dry Inlet Pressure (kPa) |
| Analog Input 3 | Wet-side Inlet Gas Flow Rate (slpm) |
| Analog Input 7 | Dry-side Inlet Gas Flow Rate (slpm) |
| **Device 2** | |
| Analog Input 3 | CEM Liquid Water Injection Rate (g $hr^{-1}$) |
| **Device 3** | |
| Analog Input 0 | Wet Inlet Pressure (kPa) |
| **Device 4** | |
| Analog Input 0 | Wet Outlet Pressure (kPa) |
| Analog Input 3 | Dry-side Differential Pressure (no longer used) |
| Analog Input 4 | Dry Outlet Pressure (kPa) |
| Analog Input 7 | Wet-side Differential Pressure (no longer used) |

Table 6 contains the list of experimental apparatus output channels. Note that while the dry-side pressure actuation channel was defined the pressure control hardware was not implemented. Both dry and wet stream outlet pressures were controlled using manual needle valves on the fixture outlets.

**Table 6 - Control system outputs**

| **Device 1** | |
|---|---|
| Analog Output 0 | Wet-side Gas Flow Set point (slpm) |
| Analog Output 1 | Dry-side Gas Flow Set point (slpm) |
| **Device 2** | |
| Analog Output 0 | CEM Water Injection Set Point (g $hr^{-1}$) |
| **Device 3** | |
| Analog Output 0 | CEM Temperature Set Point (°C) |
| **Device 4** | |
| Analog Output 0 | Dry-side Pressure Set Point (kPa, not implemented) |
| Analog Output 1 | Water Removal Pump control |

Control actions are performed by a Measurement Computing Multifunction DAQ. The positive displacement water feed pump is operated using a simple on/off relay connected to this multifunction DAQ while the inlet gas temperatures and humidifier fixture temperature are controlled by adjusting the duty cycle of their respective heaters. These heater control relays are operated through the Measurement Computing DAQ. A more detailed photograph of the data acquisition and control system can be found in Figure 15.

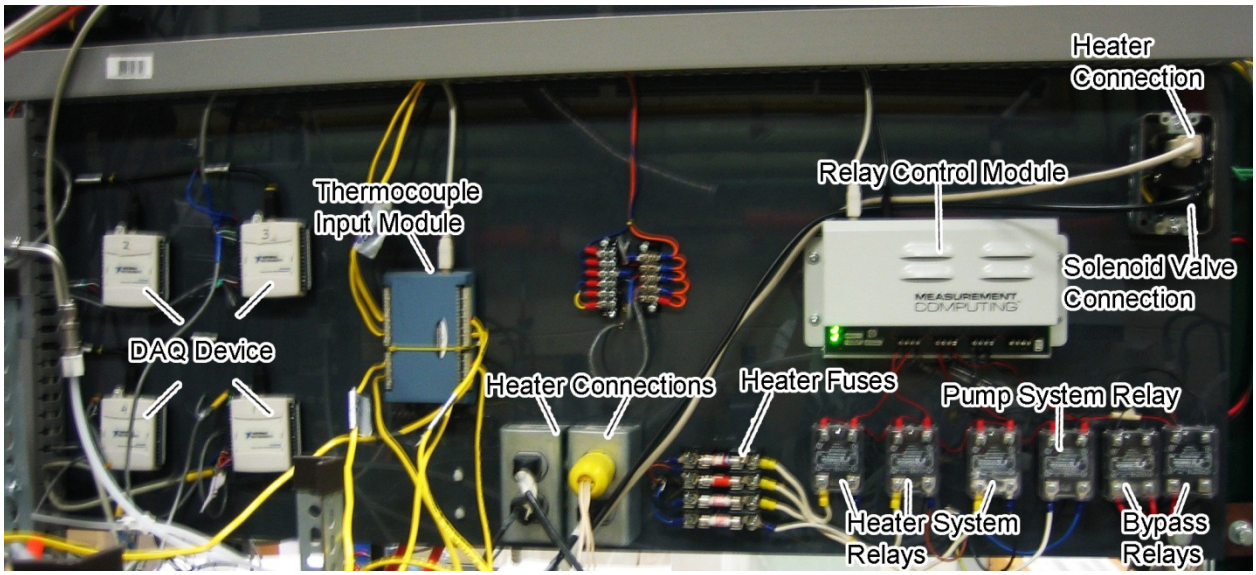


**Figure 15 - Apparatus: DAQ and control system**

This collected data is displayed through the interface illustrated below in Figure 16. Desired gas flow rates, gas inlet temperatures, fixture temperature and water injection rate are controlled via the interface.

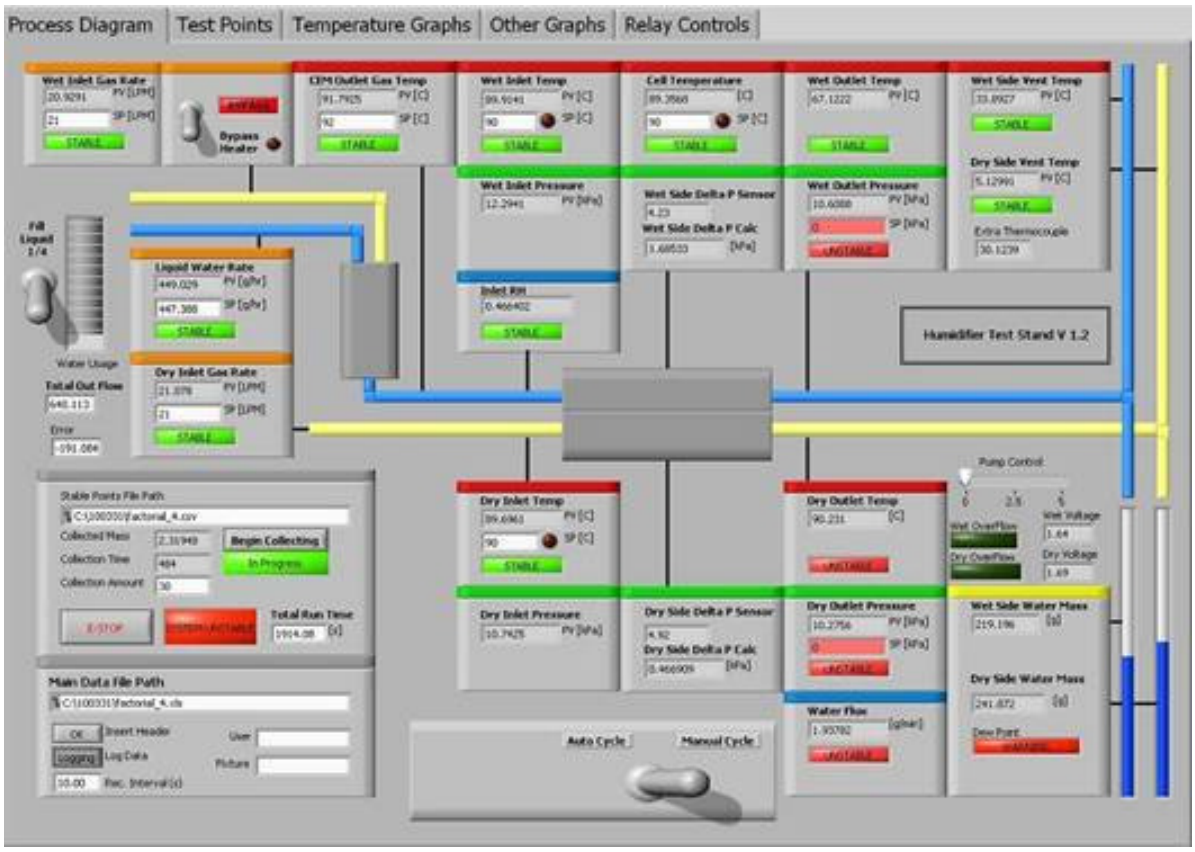


**Figure 16 - Apparatus: Primary interface**

An experiment is conducted by allowing the system to operate at steady state for 10-15 minutes while data is collected on a 10 second cycle. This data cycle time was developed with consideration to the sensitivity of the pressure transducers as well as the performance of the humidifier fixture.

Subsequent determination of the humidifier performance consists of analyzing both the dry-side water knockout mass and the water content of the dry-side gas exhaust. The integrity of experimental data is verified by comparing the total water flow injected into the system through the CEM with the water flow exiting the system in the two condenser gas outlet streams and the liquid water observed in the collection tubes. Assuming the gas exiting the condensers is at the dew-point, the amount of water exiting the system in the vapour phase can be inferred. This assumption is valid only assuming there is a detectable liquid water condensation rate. If there is no discernable condensation then this assumption cannot be made. The condensed water mass for a given period of time is simply difference between the mass of water in the dry-side

knockout tube at the start and the conclusion of the experiment. The mass of water within the collection tubes is calculated by first determining the liquid water height within the cylinder through the use of the hydrostatic pressure equation. The height of liquid water is then multiplied by the cross-sectional area of the water collection tubes. The vapour water content is integrated over the course of the experiment based on the data collected each 10 seconds. These water knockout tubes must be emptied manually with a negative displacement pump. Figure 17 shows the condenser system and water collection tubes in detail. The deionised (DI) water pump in this figure is used to refill the liquid water level within the intermediate tank connected to the CEM.

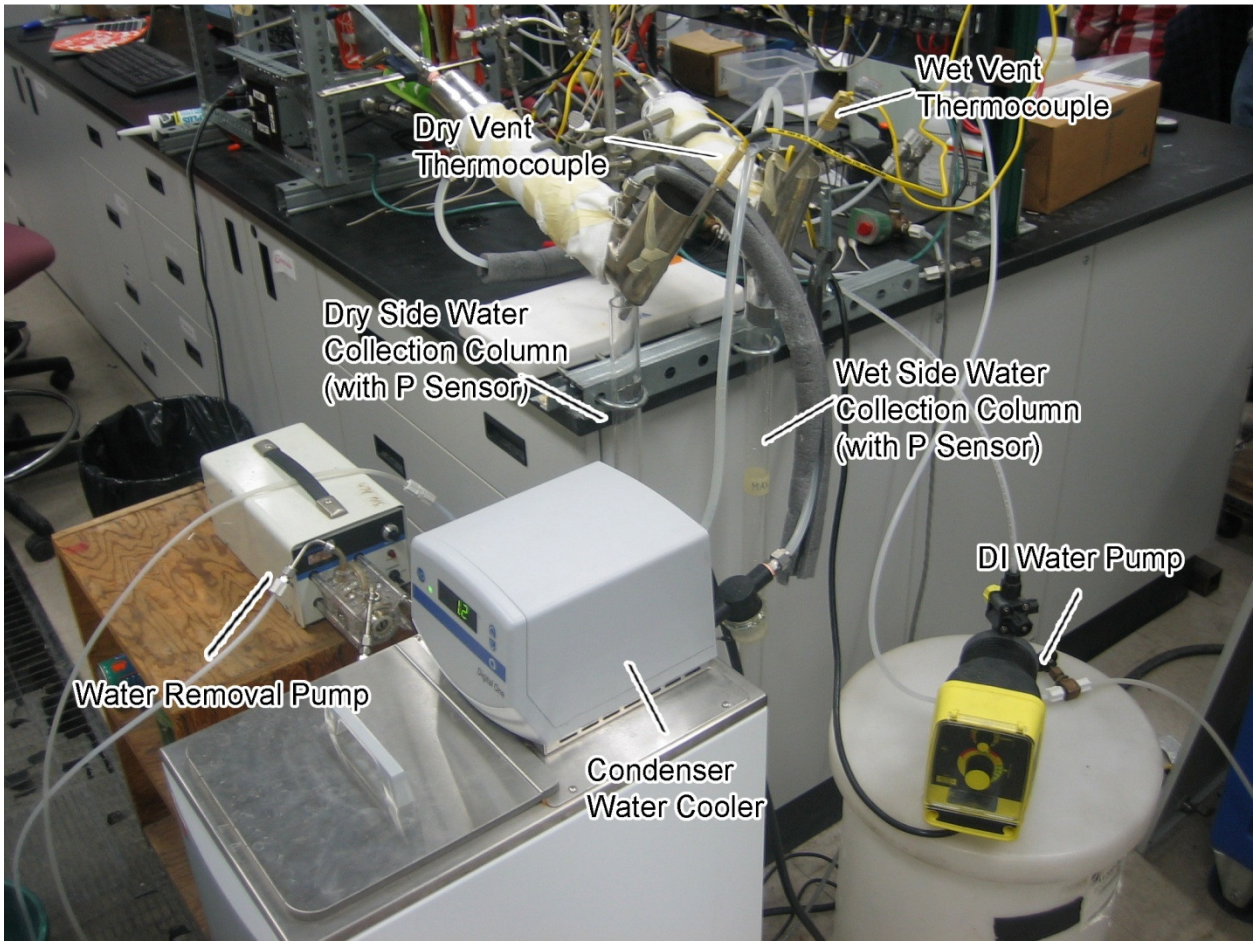


**Figure 17 - Apparatus: Water condensation and collection**

## 3.2. Humidifier Fixture

The humidifier fixture used in this thesis project was designed to be robust and customizable. An outer casing contains the gas stream NPT connections, the gas manifolds, thermal wells,

compression bolt holes/threads as well as the flow-channel insert. The manifolds and gas flow insert are oriented in the major axis of the casing, as pressure drop through the humidifier on the fuel cell anode outlet stream is not a major concern. Figure 18 shows an expanded view of the fixture. Note the NPT connections on the upper-left and lower-right faces of the humidifier casing (a) as well as the thermal wells on the upper-right and lower-left. The gas flow channels for the upper dry-side can be seen in the flow channel insert (b) running from the upper-left to lower-right. The channels for the lower wet-side insert are obscured but run perpendicular to those of the dry side insert. Finally note the membrane and GDM assembly (c) found between the wet- and dry-side flow-path inserts.

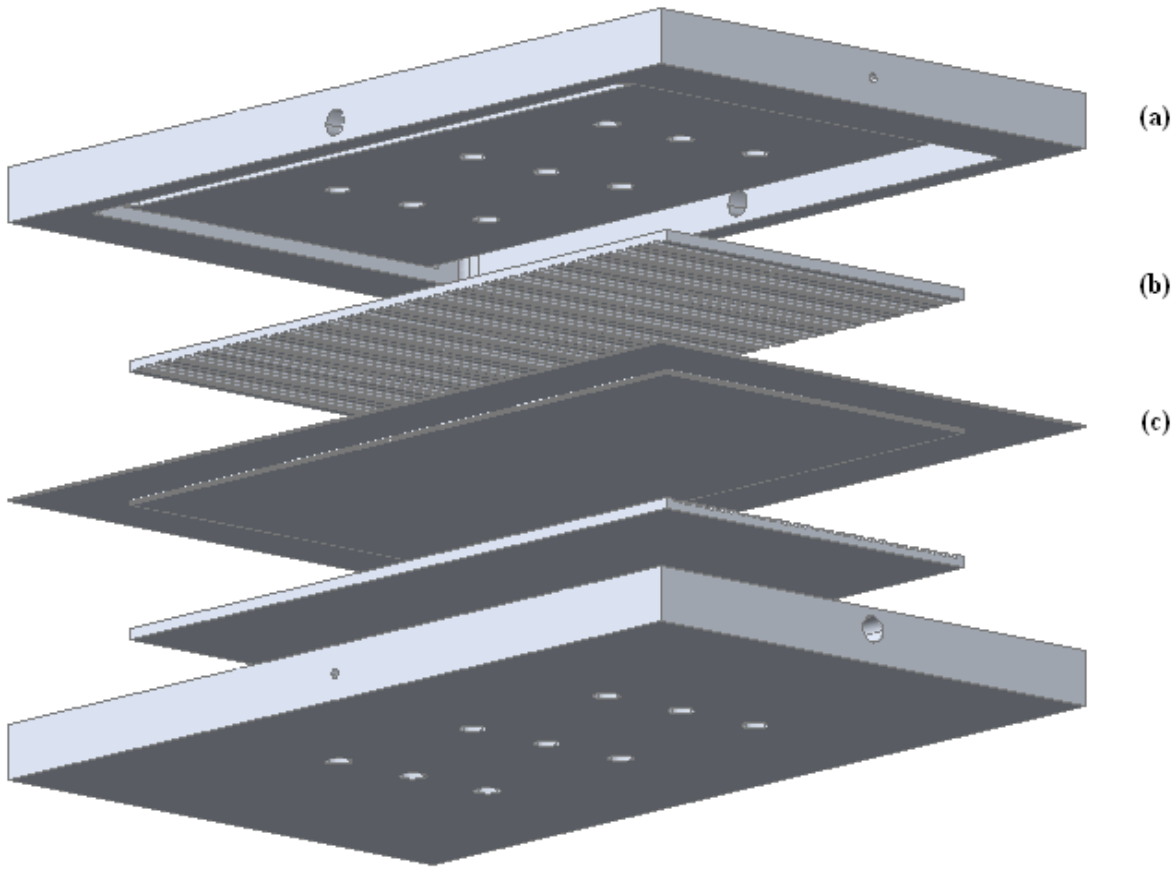


**Figure 18 - Fixture: Exploded view with inserts, membrane and GDMs**

An orthogonal view of the lower fixture casing looking from the top towards the bottom, or looking from the dry-side towards the wet-side is presented below in Figure 19.

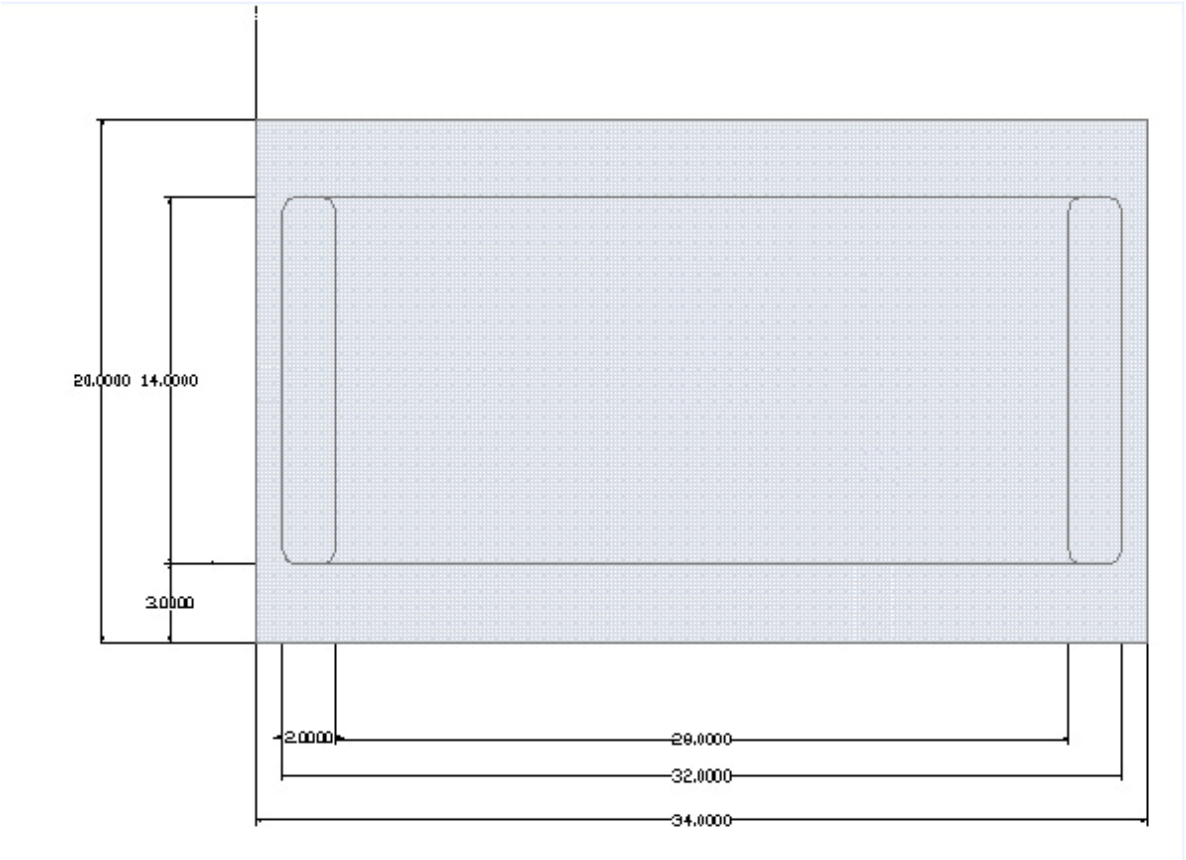


**Figure 19 - Fixture: Wet-side casing**

### 3.2.1. Material Considerations

This section presents the specifications and rationales used for the design and fabrication of the major fixture components.

#### Outer Casings

These aluminum plates were fabricated using computed numerically controlled (CNC) machine tools. The casings provide solid mounting points, thermocouple wells and screw threads for connecting the inlet and outlet gas streams. Twelve threaded bolt holes are included on the wet-side casing while matching bolt holes on the dry-side allow the membrane and GDM to be uniformly compressed through the use of the torque wrench. The outer faces are smooth to allow direct application of the heater pads used to maintain the fixture temperature. Aluminum was selected for its favourable thermal characteristics however an alternative material, plastic acrylic, was considered as it allowed direct observation of condensation within the manifolds.

### Flow-path Insert

The flow-path inserts, visible in Figure 18, were designed to be easily fabricated and installed. This modular design allowed alternate channel geometries to be easily investigated with minimum effort. Aluminum was selected as the insert material not only due to its machinability but also to minimize galvanic corrosion of both the inserts and the casings.

### Membrane

The membrane selected for these trials was DuPont's Nafion™ NR-212 uncatalyzed membrane. NR-212 was selected due to its favourable water-transfer properties, it is well characterized in literature as well as the fact that it is widely available for commercial and research purposes. The thicker membrane was preferred over the thinner NR-211 membrane in order to reduce the probability of physical failure. A recurring problem during experimentation was physical membrane failures along the gas manifolds allowing gas crossover between wet and dry streams.

### Diffusion Media

Sigracet® GDL 10AA was selected for use as the diffusion media for the humidifier fixture. This product is a carbon fibre based paper without any post-treatment, namely that the paper has not been subjected to a microporous layer or a polytetrafluoroethylene (PTFE) treatment. These post-treatments are required to improve gas-phase mass transfer in fuel cells where oxygen and hydrogen must reach the catalyst on the membrane surface however in humidification processes liquid water formation on the wet-side improves humidifier performance. Original concepts for this humidifier fixture assumed that the diffusion media was resilient enough to prevent membrane deformation over the manifolds however experimentation revealed that the membranes continued to fail despite the presence of the diffusion media. This prompted the addition of the Kapton® layer described below.

### Seals

Two separate layers were used to prevent undesired gas leaks in the experimental apparatus. The orange rubber gasket ensures a gas seal between the two aluminum casings. The integrity of this seal is verified by immersing the fixture in water while passing air through the wet and dry channels. The primary function of the yellow Kapton® layer is to reinforce the membrane over

the gas manifolds. The membrane itself provides the gas seal between the wet and dry sides and for low pressure differential situations reinforcement was not required however for situations where this difference exceeded 20 kPa membrane failures would occur. Addition of the Kapton® reduced membrane failures however this solution is still limited to pressures below 40 kPa. Integration of the seals into the casings may be a worthy alternative to the rubber gaskets and Kapton® layers. Figure 20 presents the wet-side casing with rubber gasket and Kapton® reinforcement layer installed.

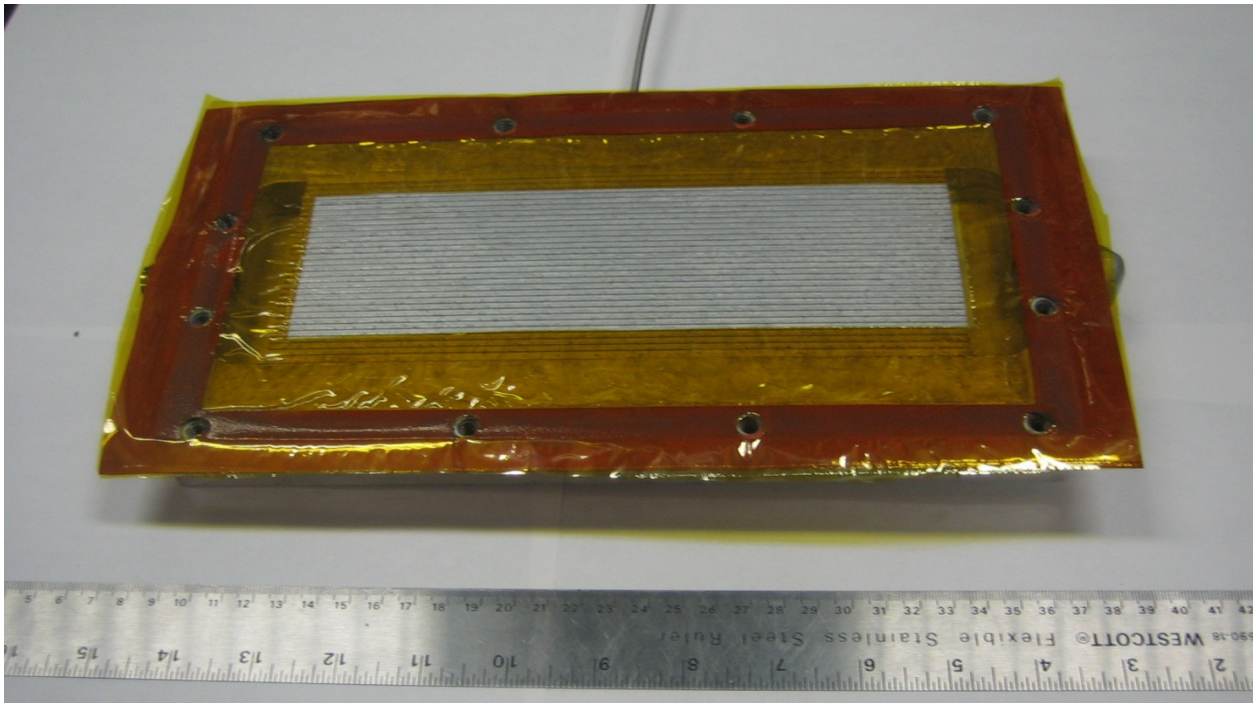

**Figure 20 - Fixture: Wet-side casing with sealing layers**

Note the thermocouple inserted in the upper part of the casing as well as the NPT to Swagelok® connections at the right and left. Twelve threaded bolt holes are located along the perimeter of the aluminum casing. The manifolds are visible through the Kapton® layer on the left and right sides of the flow-channel insert. The dry-side casing contains manifolds and gas flow paths oriented along the minor direction as the pressure drop on the fuel cell anode inlet should be minimized. Figure 21 shows the dry-side casing with the GDM and membrane layers installed.

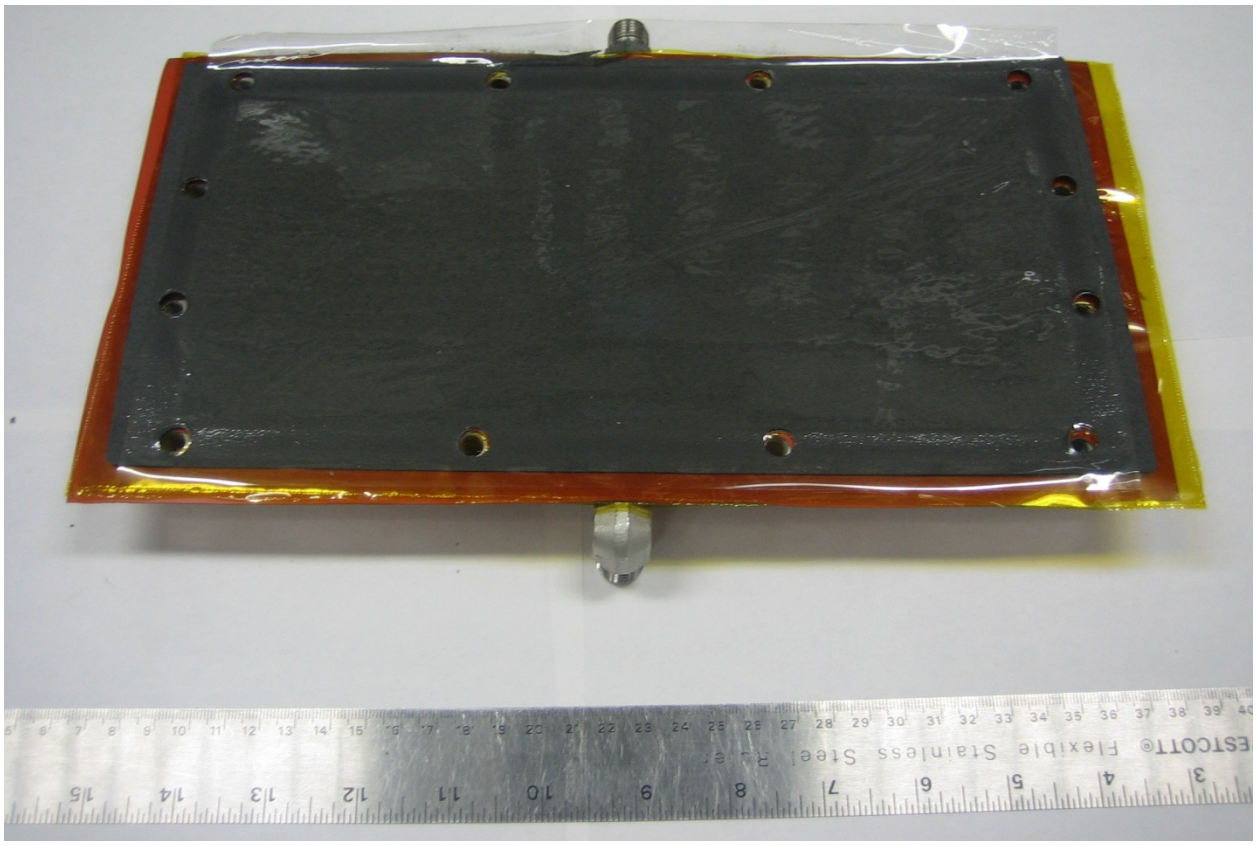

**Figure 21 - Fixture: Dry-side casing with GDM and membrane**

Note the two NPT to Swagelok® connectors at the top and bottom of the pictures. The dry-side casing contains twelve "straight-through" bolt holes for final assembly.

## 3.3. Performance Evaluation Method

Given the temperatures of the condenser exhaust stream, saturated vapour pressures can be estimated using tabulated values such as those from Perry's Chemical Engineering Handbook [24] or by using a method such as Wagner's equation.

Assuming the outlet pressure is at one atmosphere, Dalton's law of partial pressures would indicate that the saturated vapour pressure in atmospheres would represent the mole fraction of water in the gas stream. Using the ideal gas law, the water vapour mass flow rate can be determined according to Equation 40 below.

$$\dot{m}_w = \frac{y_w}{1-y_w} * \dot{V}_{dry} * \frac{P_{std}}{R*T_{std}} * M_w \qquad \text{(Eq40)}$$

Where $y_w$ represents the mole fraction of water, $V_{dry}$ represents the standard conditions volumetric flow of the dry-side gas, $P_{std}$ is equal to the standard pressure of one atmosphere, $T_{std}$ is equal to the standard temperature of 273.15 K and $M_w$ represents the molecular mass of water in g $mol^{-1}$.

A cumulative uncondensed water content encompassing the entire experimental run can be determined by taking the value calculated using Equation 40 and multiplying it by the ten second interval for which it is assumed to be valid. Summing this value over the course of the experiment will result in the mass of water exhausted from the dry side condenser in the vapour-phase.

While the vapour content must be calculated for each ten second interval the condensed water mass can be determined by simply subtracting the initial water knockout mass from the final value. Given an overall vapour-phase water mass, an overall condensed water mass and the length of the experiment an average water transfer rate for the fixture can be determined.

## 3.4. Example Data for a Standard Run

The experimental test station collects and records many factors during an experimental run. In the interest of brevity and readability only those factors required to calculate the fixture water transfer performance shall be presented. These factors, illustrated in Table 7, include dry- and wet-side water knockout mass, the dry-side gas flow rate as well as dry- and wet-side condenser outlet temperatures.

**Table 7 - Standard run example data**

| Run Time (s) | Dry Flow (slpm) | Wet Knockout Mass (g) | Dry Knockout Mass (g) | Dry Vent T (°C) | Wet Vent T (°C) |
|---|---|---|---|---|---|
| 420 | 31.157 | 243.485 | 267.477 | 7.114 | 42.256 |
| 430 | 31.157 | 242.275 | 268.531 | 7.094 | 42.478 |
| 440 | 31.157 | 243.788 | 269.872 | 7.111 | 42.427 |

This data can be collected at all times during experimentation including early start-up and between experimental test-points. Figure 22 below illustrates the trends for both condenser vent

temperatures for a set of experimental tests. This set contains the start-up conditioning followed by a set of 5 test-points and then the same 5 test-points in reverse order.

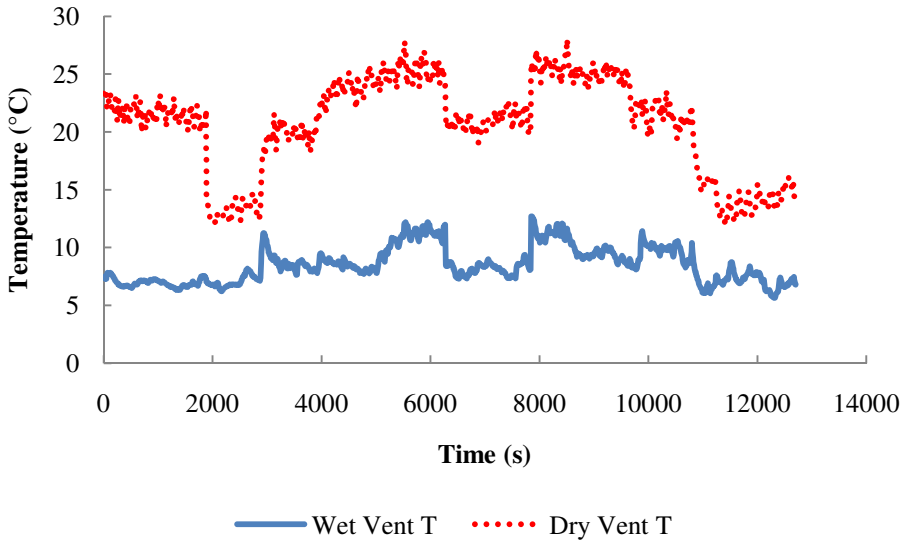


**Figure 22 - Condenser vent temperatures example data**

Note that in this case the fact that the dry vent temperature is higher than the wet vent temperature is due to the condenser cooling arrangement. In this test the cooling water is fed through the wet-side condenser before flowing through the dry-side condenser. The mass of water within the water knockouts can be found in Figure 23 below for this run.

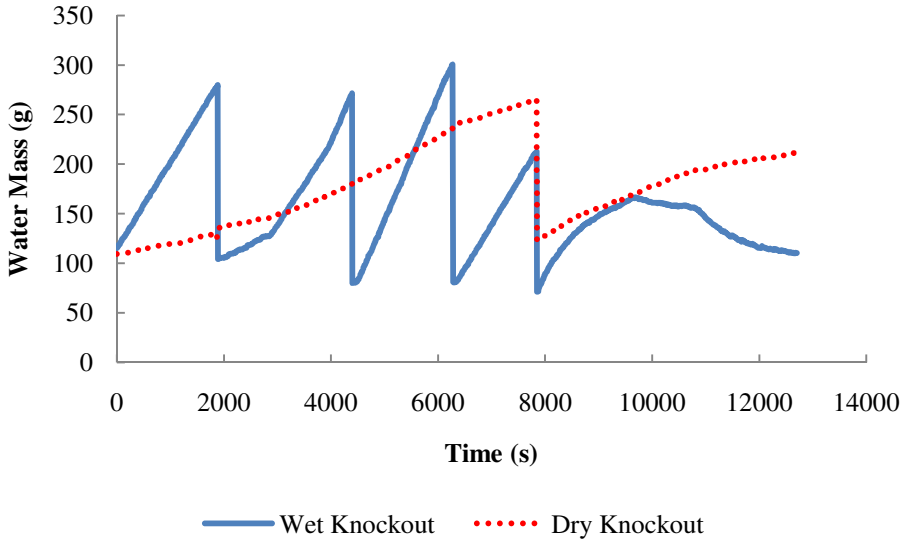


**Figure 23 - Water knockout masses example data**

Notice that the slope of the wet-side water mass is much greater than that of the dry-side. This behaviour agrees with the hypothesized performance considering that the wet-side gas tends to have far more water content as well as the fact that the wet-side condenser temperature is considerably lower than the temperature on the dry-side. The sharp downward trends are caused by water knockout empty events, in which the water is siphoned off to avoid overflow. These empty events should never take place during a section of fixture performance evaluation data as it can interfere with the water balance verification calculations presented soon in Section 3.6. Part of the information required in these forthcoming verification calculations is the feed rate of water to the system. An example of this feed rate data can be found in Figure 24.

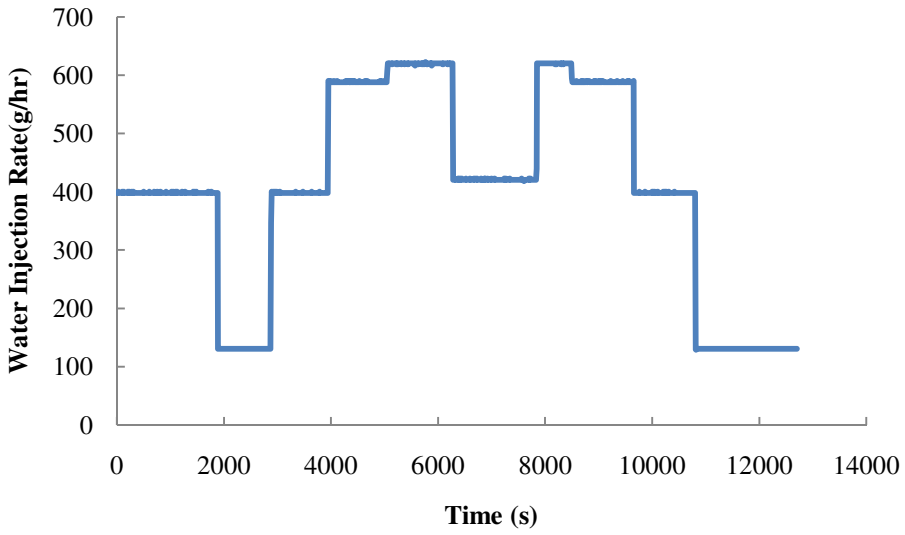


**Figure 24 - Water injection rate example data**

One can see the initial start-up water injection rate, by the five separate set-points and their reversed order. The injection rate exhibits little instability and can be adjusted to generate wet-side gas with consistent water content. In order to calculate the relative humidity of the wet inlet gas one must combine this water injection rate with the standard gas flow rate illustrated in Figure 25.

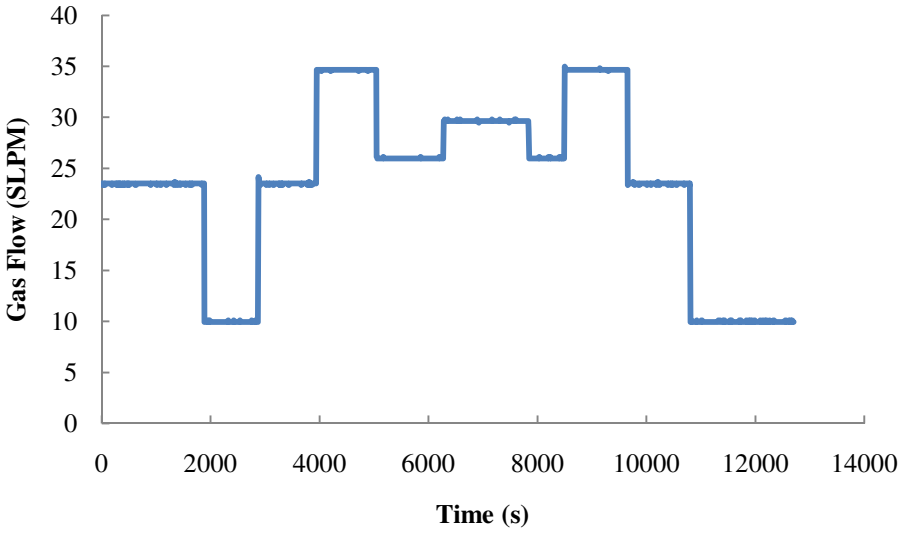


**Figure 25 - Wet-side air flow rate example data**

The data in Figure 25 presents the data in standard litres per minute (SLPM) which is defined as the volumetric flow rate at 273 K and 1 atm. It should also be clear that this value represents only the oxygen and nitrogen components of the wet-side gas stream. Only the wet stream data was shown in this example as for this particular set of data the wet and dry air flow rates are equal to each other. The small perturbations visible during operation are due to the data granularity of the gas flow meter readings. The streams can be independently controlled, an advantage used in many of the results forthcoming in this thesis, however in a realistic fuel cell humidifier test situation these streams should be very close to each other.

## 3.5. Standard Operational Scenarios

A group of five scenarios were selected as representative operational set-points for the fuel cell humidifier. Table 8 summarizes approximate conditions for each of these 5 standard test-points. Approximate values are presented here for confidentiality reasons.

**Table 8 - Standard operational scenarios**

| Test-Point | Wet-Side Inlet RH (%) | Channel Reynolds' Number | Temperature (°C) |
|---|---|---|---|
| 1 | 70-80 | 1000-1400 | 80 |
| 2 | 70-80 | 2500-2900 | 80 |
| 3 | 70-80 | 4000-4400 | 80 |
| 4 | 70-80 | 3100-3500 | 80 |
| 5 | 70-80 | 3300-3700 | 80 |

During early exploratory experiments it was observed that the fixture performance for the first test-point was difficult to determine using the existing experimental apparatus. For this reason experimental trials focused mainly on points 2 through 5.

## 3.6. Performance Verification

There are several post-run methods that can be employed to verify the integrity of experimental data collected on this apparatus. The most straightforward of which is investigation of the raw data trends over time to look for instability or poor set-point tracking. A more advanced method of performance verification is to perform a mass balance on the water entering and leaving the system. Confirming that the fixture is completely sealed does not guarantee that the data analysis will generate water balanced mass steams at the fixture exit. Recall the method in which fixture performance is evaluated. A condenser on both the wet and dry outlets cools the exit streams such that liquid water begins to condense. Supposing that one of the streams cannot be cooled to its dew-point, the amount of water in that stream cannot be predicted. Only the condenser vent temperatures and the inlet gas feed-rates are known and as such water content is calculated under the assumption that the water vapour partial pressure is equal to the saturated water vapour pressure at the condenser outlet temperature. Knowing that additional water can be calculated if the condenser cooling is inadequate, the veracity of experimental data can be confirmed by summing the wet-side water knockout mass, the dry-side water knockout mass, and the water content from the wet- and dry-side condenser vents. The total water content of these four streams should equal the water injection rate defined by the experimenter.

## 3.7. Thermal System Modeling

The humidifier test station contains many components that must be accurately controlled in order to collect relevant performance data. The temperatures of the humidifier fixture, the dry inlet gas and the wet inlet gas are controlled by LabVIEW through built-in PID virtual instruments (VI). Inputs to the PID VI include the temperature set-point, the measured temperature and the PID tuning parameters. The output of the PID block is the duty cycle of the associated heater. Initially these tuning parameters were estimated using a trial-and-error approach, however excessive oscillation at steady-state indicated that the tuning parameters were not ideal.

A model-based tuning methodology was used to optimize PID performance. Step tests were used to determine the thermal models the following sections of the apparatus:

1. Humidifier temperature
2. Wet-inlet gas temperature
3. Dry-inlet gas temperature

The step test was performed by allowing the system to reach steady-state at a particular heater duty cycle. Once the system temperature was stable, the duty cycle was instantaneously increased through the LabVIEW interface. The process reaction curve was recorded and used in the generation of thermal system models. Initially first-order models were assumed to fit each of these thermal systems. These models assume that a step increase in the heater duty cycle results in a first-order temperature response of the form illustrated in Equation 41. An excellent reference for development of first- and second-order models is *Process Dynamics and Control* by Seborg, Edgar and Mellichamp [53].

$$y(t) = KM\left(1 - e^{\frac{-t}{\tau}}\right) \tag{Eq41}$$

If a first-order response does not seem to describe the temperature response observed, it is possible the analysis must extend to fit a second-order response. The second-order response was generated by a least-squares regression for Equation 42.

$$y(t) = KM\left(1 - \frac{\tau_1 e^{\frac{-t}{\tau_1}} - \tau_2 e^{\frac{-t}{\tau_2}}}{\tau_1 - \tau_2}\right) \tag{Eq42}$$

Once these thermal system models were identified the PID tuning parameters were generated using the Internal Model Control (IMC) method [53]. The difference between classical feedback control and IMC control can be found below in Figure 26 and Figure 27.

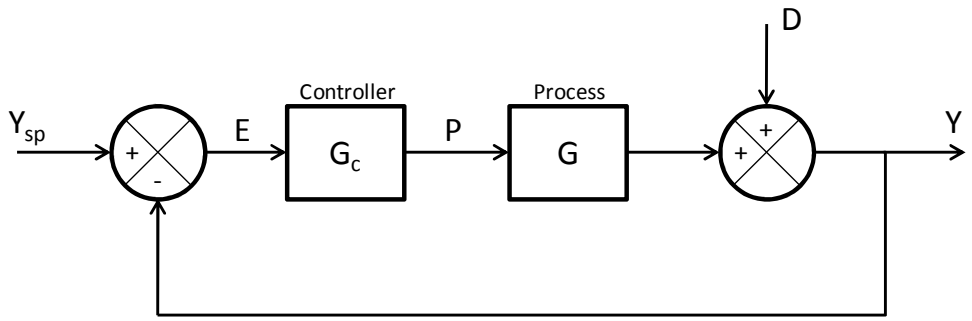


**Figure 26 - Classical Feedback Control [53]**

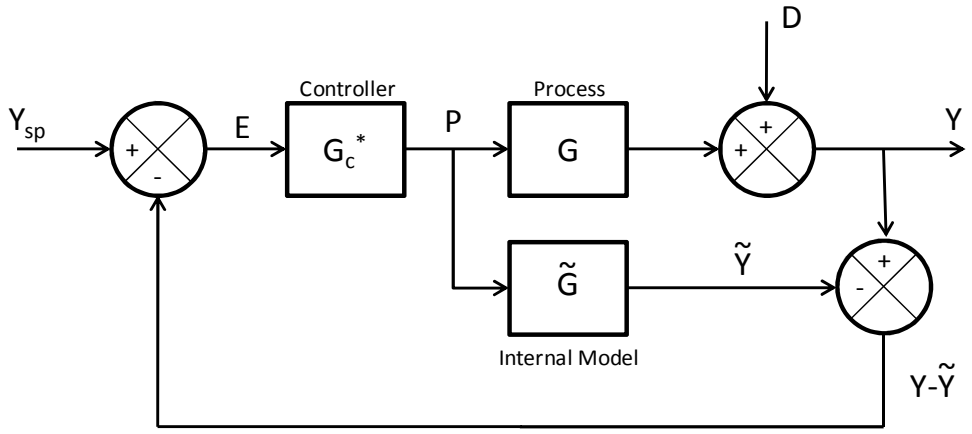


**Figure 27 - Internal Model Control [53]**

These block diagrams are identical assuming the following relationship between $G_C$ and $G_C^*$

$$G_C = \frac{G_C^*}{1 - G_C^* \tilde{G}} \quad \text{(Eq43)}$$

IMC tuning relations are derived through the following steps:

Step 1: Factor the process model according to Equation 44.

$$\tilde{G} = \tilde{G}_+ \tilde{G}_- \quad \text{(Eq44)}$$

Where time delays and right-half plane zeros are contained in $\tilde{G}_+$ and $\tilde{G}_+$ has a steady-state gain of unity.

Step 2: The controller transfer function is constructed according to Equation 45.

$$G_C^* = \frac{1}{\tilde{G}_-} f \quad \text{(Eq45)}$$

In which *f* is a low-pass filter of the following form:

$$f = \frac{1}{(\tau_C s+1)^r} \quad \text{(Eq46)}$$

For this application r = 1 was selected. Substitution of Equation 45 and Equation 46 into Equation 43 results in a controller expression which can be rearranged into the standard parallel form. This parallel form enables easy identification of the PID tuning parameters.

# 4. Model Development

## 4.1. Introduction

Development of humidifier system performance models was a major objective of this thesis project. The first two types, regression models, were used to analyze humidifier performance as well as identify possible physical conditions within the cell. The conclusions drawn from the regression models enabled the development of a MATLAB simulation with the intention of creating a tool capable of predicting performance for alternate humidifier geometries.

## 4.2. Least squares development and results

A least squares model was developed early in the project as a predictive tool for humidifier performance. This model was initially developed for the industrial sponsor's product but was later adapted for use in the humidifier designed as part of this thesis project. The results of this model were also used in order to identify key parameters that would be investigated in future factorial design experiments.

The simple model consisted of a linear combination of factors of the following form:

$$\dot{m}_w = a_0 + \sum_1^m a_m * X^k \qquad \text{(Eq47)}$$

Where X represents the physical parameter (i.e. T, C, V), k represents the exponent (i.e. -2,-1,1,2) and $a_m$ represents the term coefficient.

Excel's Solver add-in is used to determine the values of $a_m$ which results in the lowest sum of squared errors. The results of this analysis are presented in Section 5.1.

## 4.3. Factorial design and analysis

The next stage in model development was a factorial design of experiment. A full factorial design of experiment with 4 factors was developed. The factors selected to be investigated were wet-side water concentration, cell temperature, dry-side flow rate, and wet-side flow rate (dry basis).

Wet-side water concentration was selected due to its importance in Fickian diffusion (Eq38) while cell temperature has a significant effect on the membrane diffusion coefficient. Flow rates were selected in lieu of Reynolds' numbers. As can be seen in Table 9 the gas density and

viscosity terms in the Reynolds' number calculation are relatively constant in the temperature range of these experiments. These viscosities were calculated using the methods presented by Fundamentals of Momentum, Heat and Mass Transfer [54].

**Table 9 - Gas-phase densities and viscosities at operating conditions**

| Temperature (°C) | Density (g $m^{-3}$) | Viscosity x$10^5$ (Pa s) |
|---|---|---|
| 70 | 1125 | 2.04 |
| 90 | 1063 (94%) | 2.13 (104%) |

The levels of the factors used during the factorial design experimentation are presented below in Table 10.

**Table 10 - Factorial design factor levels**

| Factor | Water Inlet Conc. (g $m^{-3}$) | Temp (°C) | Dry Flow (SLPM) | Wet Flow (SLPM) |
|---|---|---|---|---|
| Low Level (-1) | 11.3 | 80 | 21 | 21 |
| High Level (+1) | 14.5 | 90 | 31 | 31 |

These factors were selected based on preliminary trial-and-error experimentation. The magnitudes of the factors are representative of the standard operational scenarios presented in Table 8.

## 4.4. MATLAB Simulation

The humidifier performance simulator, developed in full as part of this thesis project, uses fundamental mass transfer concepts to predict the performance of the fuel cell humidifier. The inputs to the model include: inlet wet- and dry-flow rates, inlet streams' relative humidity, gas flow channel geometries, gas stream pressures, cell temperature, and membrane thickness. As can be seen in Figure 28 the gas flow paths are arranged in a cross-flow pattern. The gas flow path lands, those sections in contact with the membrane, are shaded yellow and blue. Note that while these lands are situated on opposite sides of the membrane, they bound a section of the membrane that is treated as the active mass transfer area.

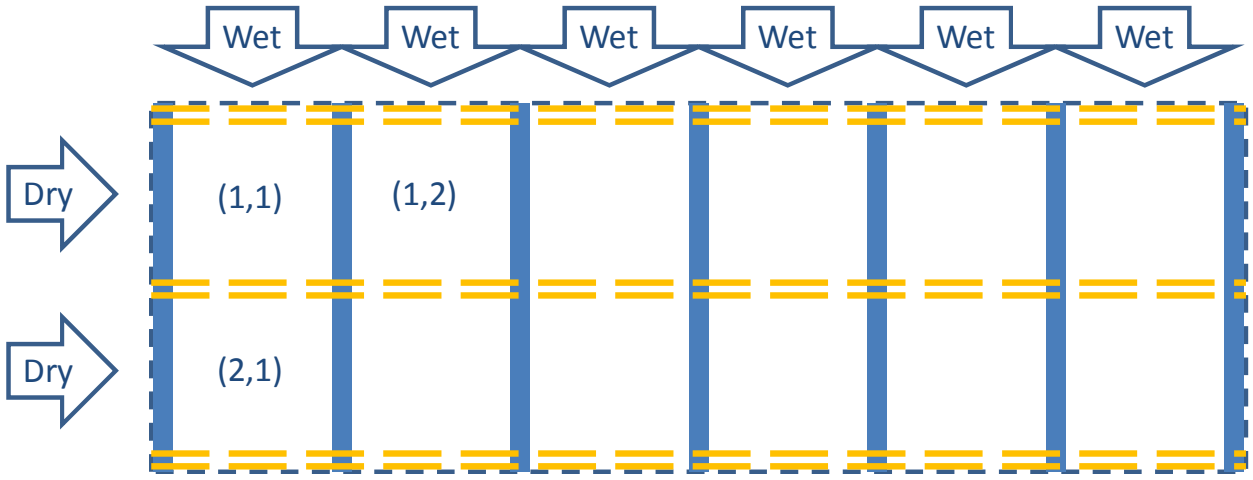


**Figure 28 - Simulation: Model fundamentals**

Initially only the conditions at location (1,1) are known however once this node's performance is calculated, the conditions in subsequent nodes (X,Y) can be determined by performing a mass balance around the node at locations (X-1,Y) and (X,Y-1). Once each node's performance is calculated, an overall humidifier performance can be inferred by comparing the wet channel outlet water contents to the inlet contents. The algorithm for determining the humidifier's performance is presented below in Figure 29.

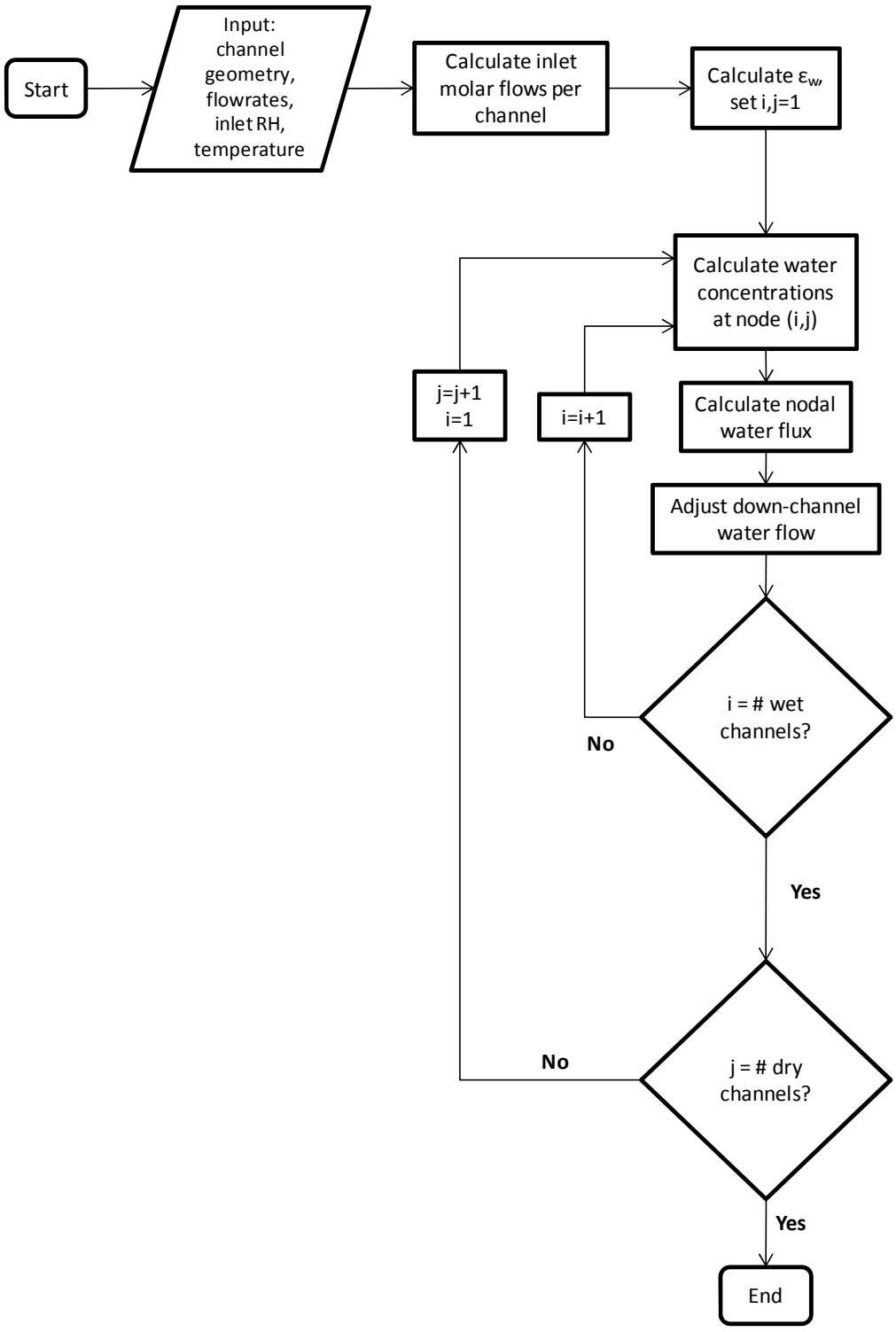


**Figure 29 - Simulation: process flow diagram**

Water vapour flux was calculated at each intersection of a wet and dry flow channel through the use of a one-dimensional Fickian diffusion calculation. Equation 48 presents the relationship for water transfer through a PFSA membrane as proposed by Motupally [15].

$$N_w = \frac{-\rho_M}{M_M \delta_M} \int_{\lambda_1}^{\lambda_2} D_{W,F} d\lambda \quad \text{(Eq48)}$$

Where $\rho_M$ represents the membrane density (g cm$^{-3}$), $M_M$ represents the molecular weight of the membrane (g mol$^{-1}$), $\delta_M$ is the membrane thickness, $D_{W,F}$ is the Fickian mass transfer coefficient and $\lambda$ represents the water content of the membrane.

The physical meaning of $\lambda$=10 suggests that for each sulphonic functional group within the membrane, there is ten molecules of water. A more complete explanation of the $\lambda$ factor can be found in Section 2.4.2.

Using this information, the performance of each particular node can be determined. Sections 4.4.1 and 4.4.2 present methods in which this performance is calculated.

### 4.4.1. Three Region Node

An early concept of the humidifier fixture simulation had three regions in each node calculation. These three regions were gas-phase diffusion through the wet-side GDM, Fickian diffusion through the membrane and gas-phase diffusion through the dry-side GDM. While the water concentrations for the surfaces of the GDM were known, the water concentrations at the GDM/membrane interface were not known. An iterative method was employed to calculate these interfacial concentrations by equating the mass transfer rates for all three regions. Steady state operation of the humidifier fixture required that this condition hold true. A schematic of this concept is presented below in Figure 30.

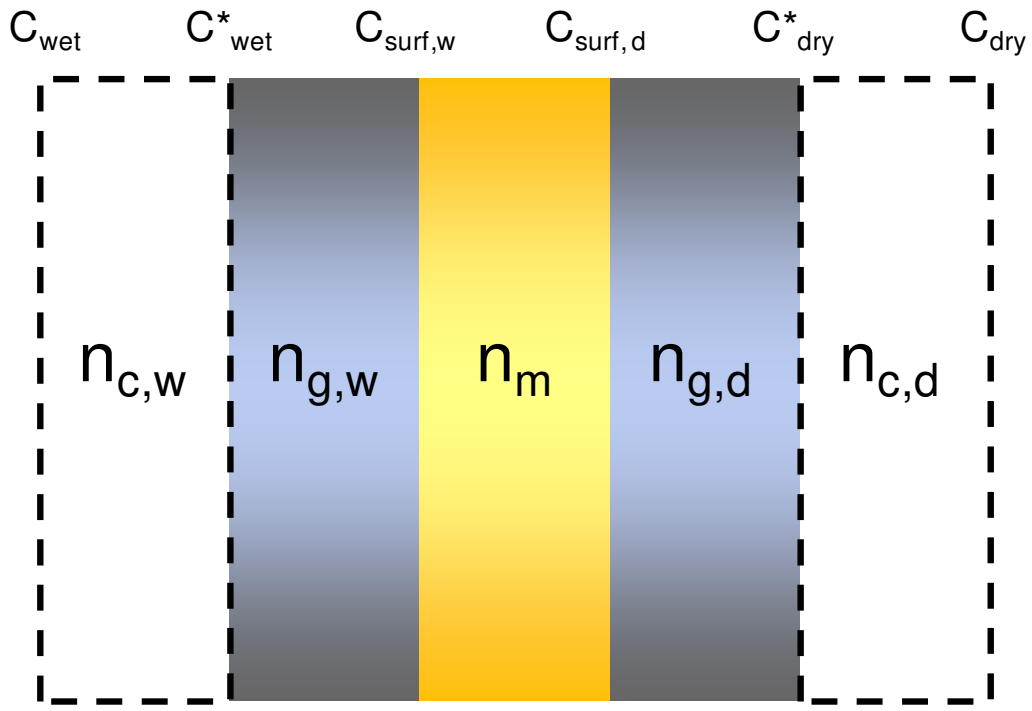


**Figure 30 - Simulation: Three region node**

The only concentrations known at the onset of simulation are $C_{wet}$ and $C_{dry}$. The mass transfer rates, represented by $n_x$ are calculated according to the equations presented in Table 11. Note that in this table ε represents the porosity within the GDM while $D_{AB}$ represents the mass diffusion coefficient of water in a gas mixture.

**Table 11 - Calculation node regions**

| Region | Equation | Regime |
|---|---|---|
| Wet Channel | $n_{c,w} = D_{AB}(C_{wet}-C^*_{wet})$ | Gas Phase Diffusion |
| Dry Channel | $n_{c,d} = D_{AB}(C^*_{dry}-C_{dry})$ | Gas Phase Diffusion |
| Wet GDM | $n_{g,w} = \varepsilon D_{AB}(C^*_{wet}-C_{surf,w})$ | Gas Phase Diffusion |
| Dry GDM | $n_{g,d} = \varepsilon D_{AB}(C_{surf,d}-C^*_{dry})$ | Gas Phase Diffusion |
| Membrane | $n_m = D_{w,F}(C_{surf,w}-C_{surf,d})$ | Membrane Diffusion |

Early simulation models assumed the GDM surface concentrations, $C^*_{wet}$ and $C^*_{dry}$, were equal to the bulk channel concentrations. In these simulations $C_{surf,w}$ and $C_{surf,d}$ were manipulated such

that $n_m$, $n_{g,w}$ and $n_{g,d}$ were equal to each other while ε was defined by the user and used as a model tuning parameter.

Initial calculations indicated the transfer rate through the gas-phases was several orders of magnitude higher than that through the membrane. The end result of this conclusion was that the water concentrations at the GDM/membrane interface were nearly the same concentration as that at the surface of the GDM. If membrane surface concentrations are assumed to be equal to the gas concentrations at the GDM surface then the node water transfer can be determined using a single integral equation thereby negating the need for an iterative calculation. In the interest of improving simulation performance this iterative method including all regimes was removed and node transfer determinations were subsequently calculated solely based on membrane diffusion.

### 4.4.2. Partial Water Coverage Model

Humidifier performance estimations using the three regime node model were significantly lower than experimental data indicated. It was conjectured that a model that accounted for the presence of liquid water could describe the humidifier performance. Equation 48 describes Motupally's method of calculated PFSA membrane water flux using membrane water content, also known as Lambda (λ) [15]. Equation 38 describes the method in which gas phase water activity affects the value of λ at the membrane surface. This relationship holds true for gas phase water activities from zero to one however a membrane in contact with liquid water does not behave in the same manner as a membrane in contact with saturated water vapour despite both conditions representing a water activity of unity. This non-contiguous behaviour is known as Schroeder's Paradox and results in an elevated value of λ for membranes in contact with liquid water. Motupally states that for a wet membrane at 30°C the associated membrane Lambda is equal to 22 while a wet membrane at 80°C has a Lambda of 17. The model was revised to include a tuning parameter $\varepsilon_w$ which represented the fraction of the membrane surface which was covered in liquid water. Thus it is assumed that some water will condense on the surface of the membrane prior to diffusion and this condensed water layer covers a fraction, $\varepsilon_w$, of the nodal membrane area. For operating temperatures other than 30°C and 80°C the membrane lambda is extrapolated from those values indicated by Motupally [15]. At this point the nodal water transfer rate can be described according to Figure 31.

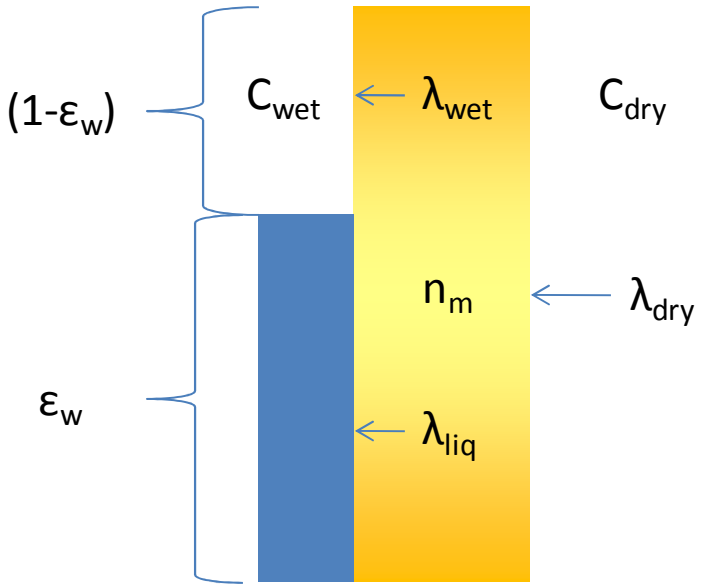


**Figure 31 - Simulation: Partial coverage node**

This situation is implemented in the simulation by assuming a certain fraction, $\varepsilon_w$, of the membrane surface produces a mass transfer rate equal to that of a membrane in contact with liquid water while the remaining fraction, $(1-\varepsilon_w)$, produces a mass transfer rate described by a membrane in contact with humidified gas at the gas-flow channel conditions.

The value of $\varepsilon_w$ is highly dependent on the test conditions such as temperature, inlet water content and gas stream flow rates. It was necessary to develop methods in which $\varepsilon_w$ could be calculated given those experimental conditions. The first step was to determine theoretical water coverage for each of the experimental test-points. At this point $\varepsilon_w$ was a user-defined constant in the model which was adjusted manually until the modelled fixture performance matched the observed experimental performance. In this method each set of experimental conditions was matched with a value of $\varepsilon_w$ which resulted in the appropriate modeled water flux. Once values for $\varepsilon_w$ were determined by a trial-and-error method, a regression model could be used to mathematically express $\varepsilon_w$ in terms of the experimental conditions.

Two forms of regression model were proposed: a generic linear least-squares model and a regression model based on the factorial design results presented in Section 5.4. The general form of the least-squares model is presented below in Equation 49.

$$\varepsilon_w = \alpha_1 + \alpha_2 T + \alpha_3 T^2 + \frac{\alpha_4}{T} + \frac{\alpha_5}{T^2} + \alpha_6(SV_w) + \alpha_7(SV_w)^2 + \frac{\alpha_8}{(SV_w)} + \frac{\alpha_9}{(SV_w)^2} +$$

$$\alpha_{10}(SV_d) + \alpha_{11}(SV_d)^2 + \frac{\alpha_{12}}{(SV_d)} + \frac{\alpha_{13}}{(SV_d)^2} + \alpha_{14} RH + \alpha_{15} RH^2 + \frac{\alpha_{16}}{RH} + \frac{\alpha_{17}}{RH^2} \qquad \text{(Eq 49)}$$

where $SV_w$ and $SV_d$ represent the space volumes of the wet and dry streams while RH represents the relative humidity of the wet-inlet stream in decimal form. One should note while the general description of the least-squares method is found here, the water coverage estimation models based on factorial design methods are not discussed until Section 5.6.

# 5. Results & Discussion

## 5.1. Thermal Modeling Results

As described in Section 3.7, a model-based tuning methodology was employed to optimize both the test station and fixture thermal characteristics. The thermal system step responses found in Figure 32, Figure 33 and Figure 34 were generated by disabling the PID temperature control system and manually adjusting the heater duty cycles. A test run consisted of operating the heater at a particular output until the system reached a steady state at which point the duty cycle was instantaneously changed to a different value. The system response to this input change was recorded in order to develop mathematical models to describe the system behaviour. The humidifier fixture and dry-inlet gas systems were found to be well described by a first-order model while the wet-inlet gas system appeared to follow a second-order model. The steady-state gains and time constants were derived according to Section 3.7 and are presented below in Table 12.

**Table 12 - Thermal modeling: PID gains and time constants**

| System | K (°C per % duty) | $\tau 1$ (min) | $\tau 2$ (min) |
|---|---|---|---|
| Wet Inlet 2$^{nd}$ Order (1) | 0.77 | 0.94 | 0.92 |
| Wet Inlet 1$^{st}$ Order (1) | 0.69 | 1.83 | N/A |
| Dry Inlet (2) | 0.91 | 5.78 | N/A |
| Fixture (3) | 2.06 | 24.33 | N/A |

Using these steady state gains and time constants, the following temperature response models were generated. Figure 32 contains the temperature responses for PID #1, the wet inlet temperature.

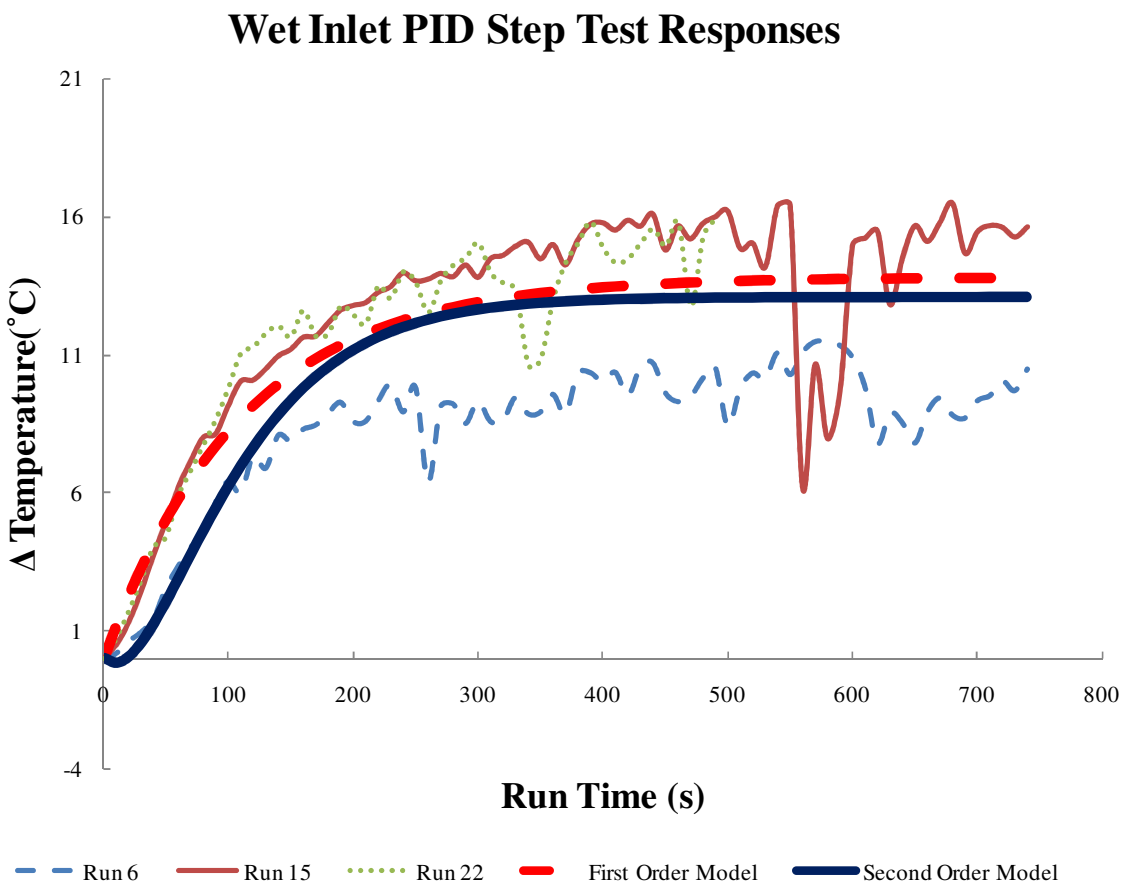


**Figure 32 - PID tuning: Wet inlet temperature modelling**

It can be seen that the Run 6 temperature profile is significantly different than the data seen in Runs 15 and 22. It should be noted that the first-order thermal model was developed using all three sets of data. A second order model for this system was derived after observing significant cyclic behaviour in the wet inlet temperature during the performance evaluation runs illustrated in Figure 35. For now both first and second order models will be considered and further discussed with Figure 35. The step response analysis for PID #2, the dry inlet temperature, is contained in Figure 33.

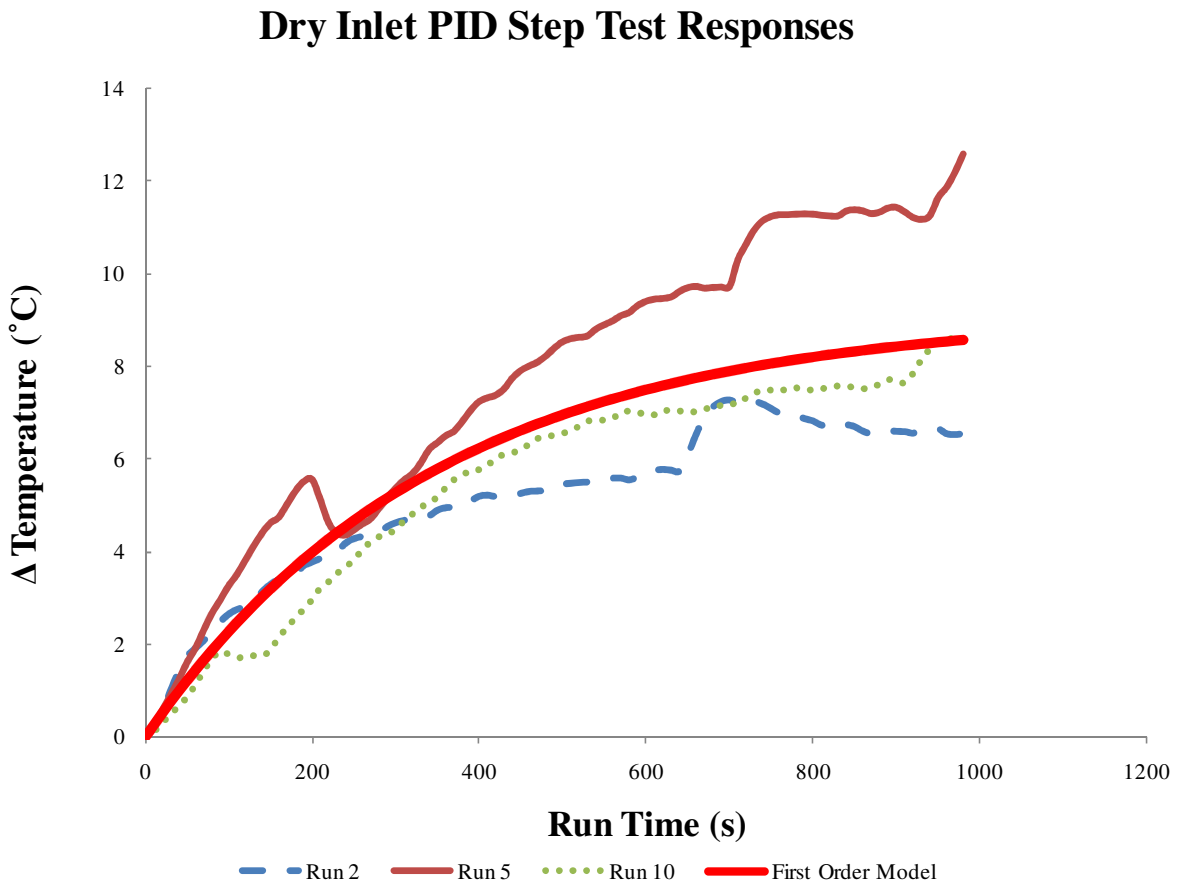


**Figure 33 - PID tuning: Dry inlet temperature modelling**

Examination of the dry inlet temperature responses indicates relatively consistent behaviour. The first order model was developed using the concepts introduced in Section 3.7. As indicated in Table 12 the dry inlet temperature model was determined to have a gain of 0.91 °C per % duty and a time constant of 5.78 minutes. A dry-inlet system performance comparison between the original trial-and-error based tuning parameters and those derived by model-based tuning can be found in Figure 36. Finally the PID #3 step responses for the humidifier fixture temperature can be found in Figure 34.

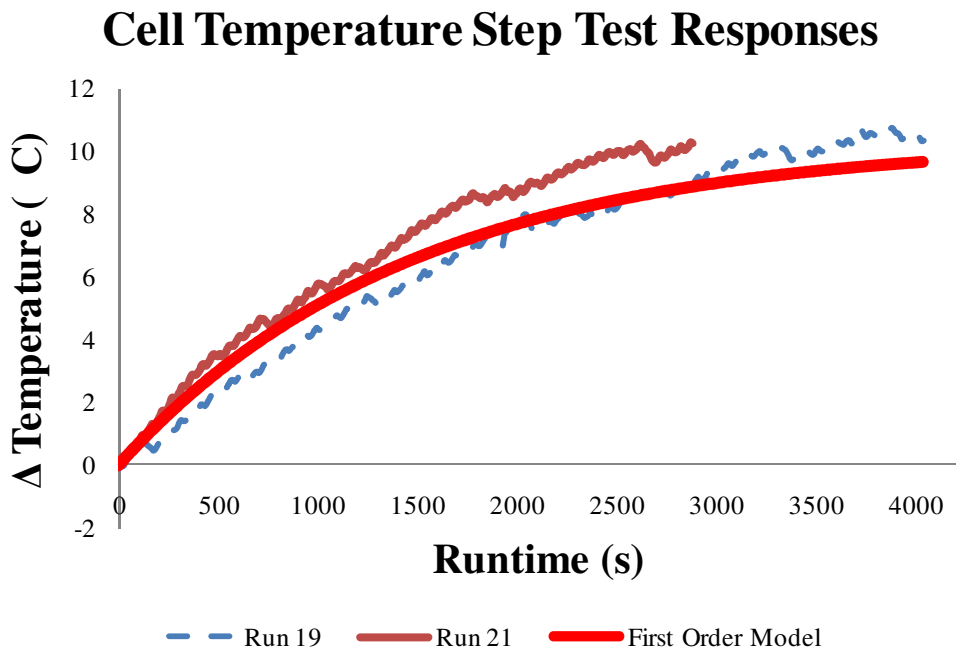


**Figure 34 - PID tuning: Cell temperature modelling**

One will immediately note that the system response time for the cell temperature is much slower than those of the gas inlet temperatures. A major factor in this slower response time is the thermal inertia associated with the moderately sized aluminum casing of the humidifier fixture. This lag time in the thermal response is expected and must be considered in the design of all such systems. The fixture heater output is also, by design, significantly lower than those in the gas inlets. The gas inlet heaters are required to heat a gas stream from room temperature to 60-90°C before the gas streams are fed to the humidifier fixture. These heaters must balance unsteady inlet conditions, stability and performance in order to ensure reliable humidifier performance. The fixture heater, by comparison, must regulate a system for which the majority of the inputs are already themselves controlled. Ideally the fixture heaters would be selected based on maximizing system stability over fast set-point tracking.

## 5.2. PID Performance Evaluation

The thermal models generated in Section 5.1 were used in the model-based design methods presented in Section 3.7 to generate PID controller tuning parameters. The behaviours of the thermal systems were compared using the proposed PID tuning parameters and the existing trial-and-error based controllers. The test consists of adjusting the set-point for the particular system

to 70°C, allowing the system to reach steady-state and then instigating a set-point bump from 70°C to 80°C. The results for these performance tests are presented Figure 35, Figure 36 and Figure 37.

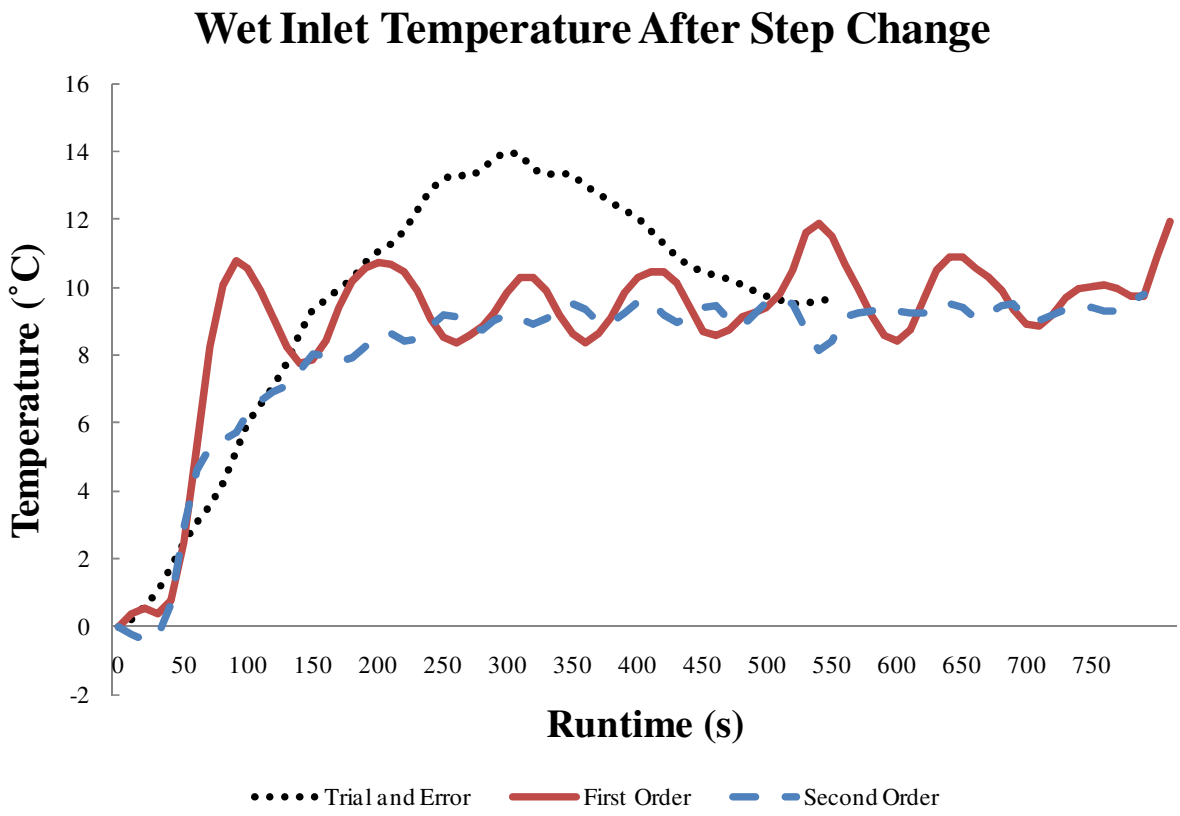


**Figure 35 - PID tuning: Wet inlet controller performance**

One can see that the performances of the first and second order based controllers are much more desirable than the trial-and-error controller. The first order controller reacts to the set-point change very quickly as well as exhibiting greater stability over the original settings while the second order controller sacrifices the extremely rapid set-point tracking for very stable steady-state characteristics. The calculated PID parameters used in these experimental runs can be found below in Table 13.

**Table 13 - PID: Wet inlet tuning parameters**

| | $K_c$ | $\tau_I$ | $\tau_D$ |
|---|---|---|---|
| Trial-and-Error | 0.800 | 0.500 | 0.500 |
| Model Based | 14.719 | 1.864 | 0.466 |

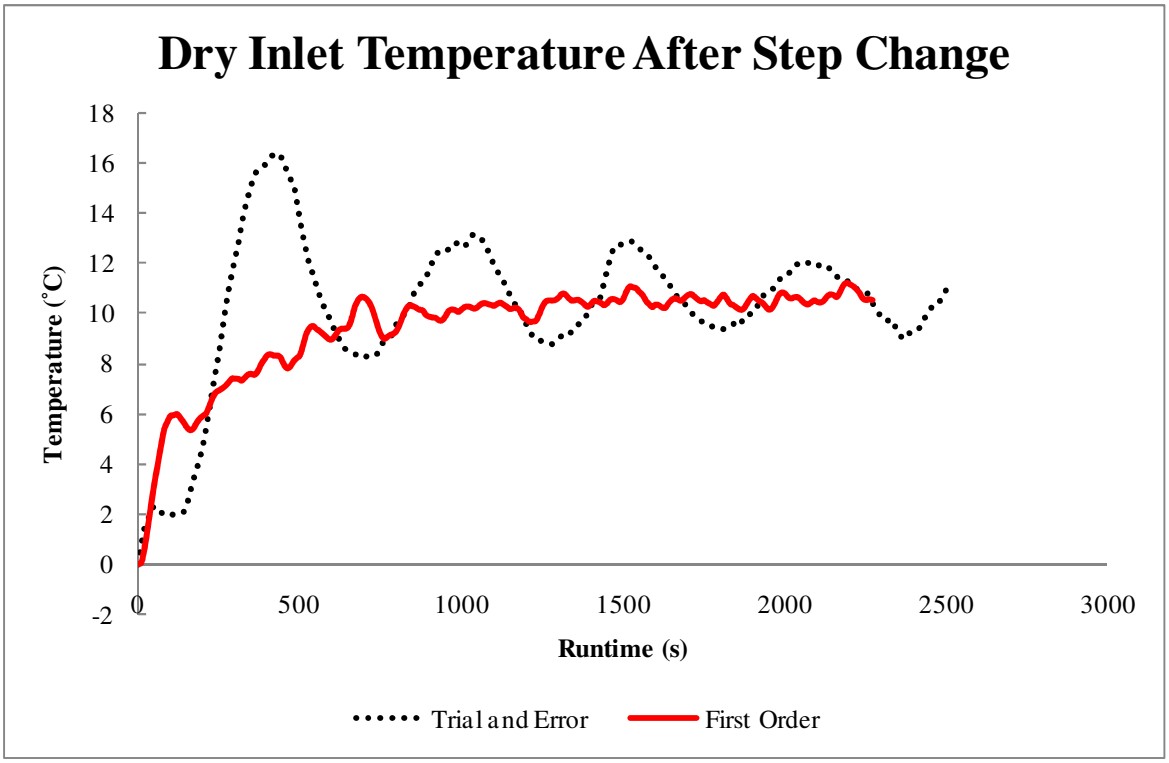


**Figure 36 - PID tuning: Dry inlet controller performance**

Note the large over-shoot from the original trial-and-error settings. The model-based tuning parameters exhibit a similarly short settling time but with significantly improved temperature stability. It can be seen that the use of model-based tuning methods reduced the steady state temperature swing from roughly 2°C to less than 0.5°C; a favourable outcome for the control of the system downstream. Table 14 presents the tuning parameters used in the PID control structure for the dry inlet temperature.

**Table 14 - PID tuning: Dry inlet tuning parameters**

| | $K_c$ | $\tau_I$ | $\tau_D$ |
|---|---|---|---|
| Trial-and-Error | 0.800 | 0.400 | 0.500 |
| Model Based | 11.002 | 5.780 | ---- |

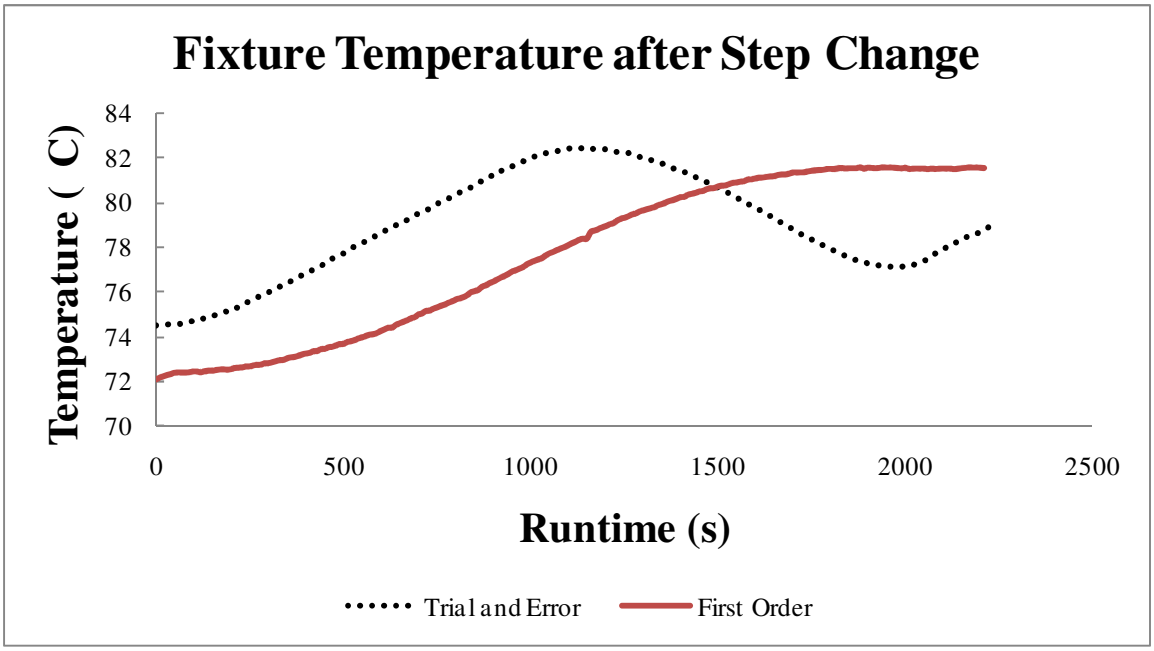


**Figure 37 - PID tuning: Fixture controller performance**

Figure 37 shows that the model based controller responds less aggressively than the trial-and-error based controller scheme. This less aggressive tuning resulted in a slightly slower response to the set-point change however the overall system stability was greatly improved. The fixture temperature reached the 80°C set-point with imperceptible ringing while the previous controller implementation demonstrated 5°C temperature swings before and after the set-point change. These performance tests indicate that the model-based tuning parameters result in a system with both improved set-point tracking and stability.

## 5.3. Least squares Data Analysis

A mathematical model was developed using the least squares method proposed in Section 4.2. The Generalized Reduced Gradient (GRG2) algorithm was employed to determine the values of the coefficients [55]. The resulting model is presented as Equation 50.

$$flux = 0.0924 + 0.0706T - 3.80 * 10^{-4}T^2 + \frac{0.0419}{T} + \frac{2.10*10^{-3}}{T^2} + 0.105V_w - 2.1 * 10^{-3}V_w^2 + \frac{0.0607}{V_w} + \frac{0.0128}{V_w^2} + 0.105V_d - 1.53 * 10^{-3}V_d^2 + \frac{0.0607}{V_d} + \frac{0.0128}{V_d^2} - 5.39RH + 3.38RH^2 - \frac{1.61}{RH} + \frac{0.234}{RH^2} - 0.0505T_d + 3.29 * 10^{-4}T_d^2 - \frac{0.0312}{T_d} + \frac{3.62*10^{-7}}{T_d^2} + 0.0384T_w - 3.80 * 10^{-4}T_w^2 - \frac{0.0255}{T_w} - \frac{4.86*10^{-4}}{T_w^2}$$ (Eq50)

Where T is the cell temperature in °C, $V_w$ is the wet-side flow rate in SLPM, $V_d$ is the dry-side flow rate in SLPM, RH is the wet-inlet relative humidity, $T_d$ is the dry-side inlet temperature in °C and $T_w$ is wet-side inlet temperature in °C. Three significant figures have been included as several terms are sensitive to small changes in the coefficient. The square and inverse-square terms in particular vary significantly for less than three significant figures.

This model was used to estimate humidifier performances under the Standard Operational Scenarios found in Table 8. Experimental uncertainty was estimated as part of the factorial design experiment presented in Section 4.3. A standard deviation of 0.05 $g \cdot min^{-1}$ was determined by computing a pooled variance based on 6 factorial center-point replicates collected as part of two separate sets of factorial design experiments as described in Section 5.4. The result of this comparison is presented in Figure 38 with error bars representing three standard deviations of uncertainty in the experimental data.

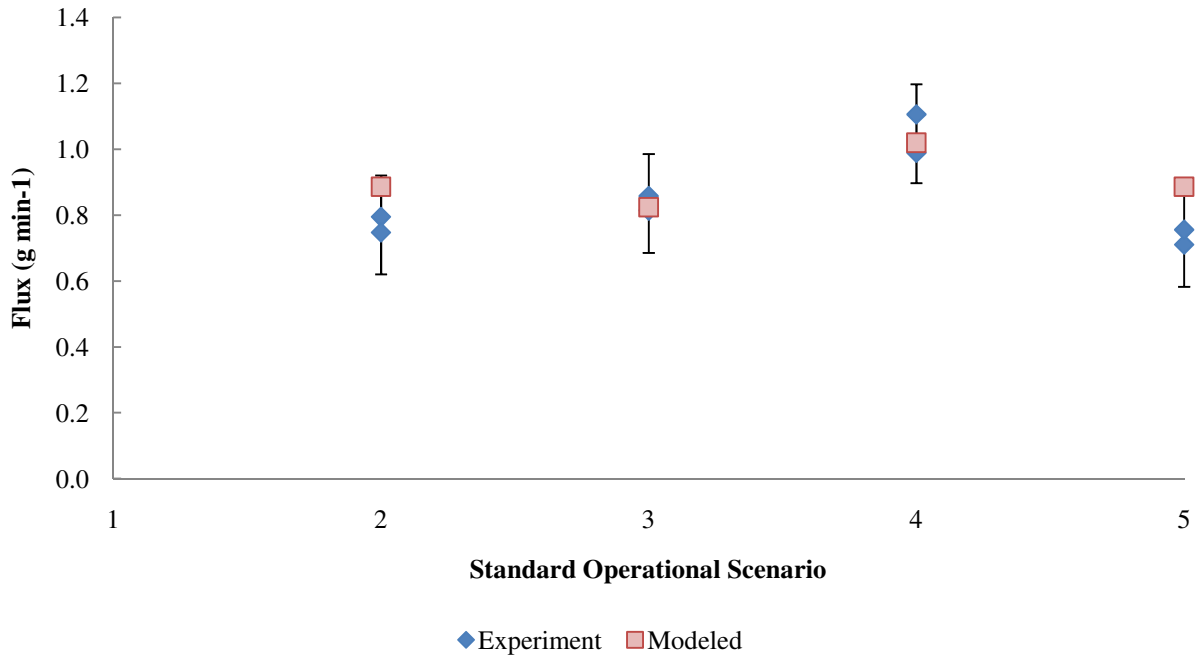


**Figure 38 - Least squares comparison: Standard operational scenarios**

It can be seen that each modelled test-point lies within three standard deviations of the experimental data. The standard scenarios performance can be accurately predicted by the least squares model however these scenarios do not contain very diverse data points. Each of these points was taken to be theoretical fuel cell operation points and as such do not vary considerably in temperature or water content. The same model was also used to analyze the data collected from the factorial design experiment and is located in Figure 39.

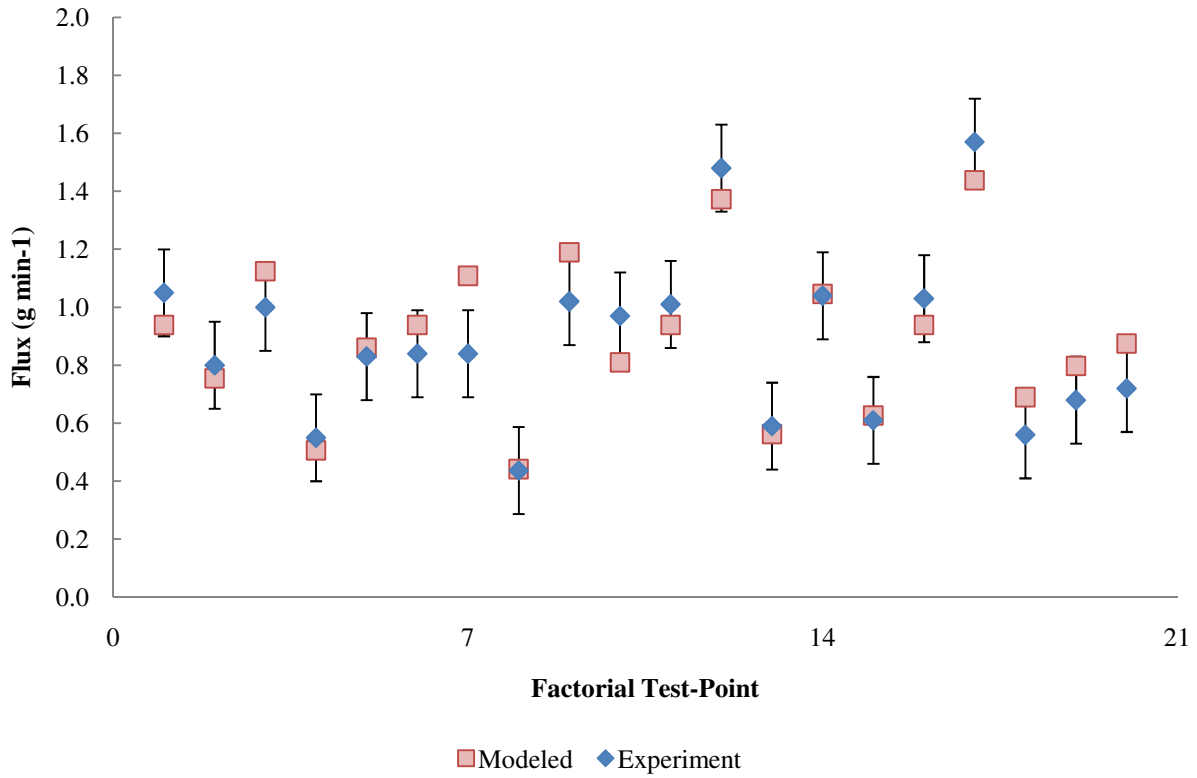


**Figure 39 - Least squares comparison: Factorial**

One will notice that nearly all data points lie inside of the experimental variance for these tests. Data points 5, 6, 7 and 8 are consecutive runs performed on the same day as part of the factorial design experiment. The experimental flux for data point 8 was unexpectedly high and as such was re-run in duplicate at the conclusion of the experiment. The flux decreased from 0.790 $g \cdot min^{-1}$ to 0.437 $g \cdot min^{-1}$ which was much closer to the results predicted by several methods developed as a part of this thesis. A possible explanation for the unexpectedly low experimental performance for data point 7 is that the proposed least squares model can not accurately represent the observed behaviour. Examination of Figure 42 indicates that this test-point lies outside the predicted range of the MATLAB model as well and as such it seems there may be experimental errors with this point as well and as such it can be considered as an experimental outlier. While examination of the raw experimental did not indicate any particular erroneous behaviour future predictions for this data point may not agree with experimental values.

A significant drawback of this least-squares method is that it is not able to model humidifiers with alternative membrane chemistries or channel geometries. The model could be adapted to

account for alternative channel geometries by converting the inlet gas flow rates, an extrinsic variable, into the Reynolds number within the channel or system space volumes which are intrinsic properties.

This regression model can be used to aid in the design of planar membrane fuel cell humidifiers. Assuming information about the wet-inlet humidity, channel geometries and gas flow-rates are known this model can be used to predict the water transfer across the membrane. Use of this model can be used to calculate the performance of both single cells as well as stacks of cells. A parallel arrangement of cells can be investigate by setting the wet- and dry-side flow rates equal to the stack inlet flow rates divided by the total number of cells. A series arrangement of cells could not necessarily be calculated using this method, as it assumes a completely dry wet-side gas stream.

Several significant drawbacks limit the applicability of this model. Firstly, the membrane size is not a factor in the regression model and as such it may not be universally applicable. At low membrane sizes where wet- or dry-side water content does not vary much the fixture performance likely varies linearly with membrane size however at larger sizes the mass transfer driving force will rapidly decrease. Secondly, this model cannot be applied to humidifiers with alternative membranes. The contribution of the membrane cannot be extricated from the rest of the performance affecting factors. Thirdly, the model can only to be applied when the temperature or gas flow-rates are close to the values used to generate the model. As with any regression model particularly high or low dependent variables can result in erroneous results.

## 5.4. Factorial Design Results

A factorial design experiment was conducted using the factors described in Section 4.3. Table 15 illustrates the factor codings used in the experiment.

**Table 15 - Factorial: Factor coding**

| | |
|---|---|
| A | Temperature |
| B | Water concentration |
| C | Wet flow |
| D | Dry flow |

Table 16 presents the calculated effects and the significance levels for the full factorial experiment. The critical F-value for this analysis is 7.708 based on a 95% confidence and four center-point replicates. This F-value is important in that for any factor for which the significance is lower than this value one cannot be completely certain that the influence of this factor has not been masked by simple experimental error. For factors in which the significance exceeds this value one has a 95% certainty that the calculated influence of the factor has not been mistakenly caused by random experimental error.

**Table 16 - Factorial: Calculated effects**

| **Factor** | **Effect** | **Significance** | | **Factor** | **Effect** | **Significance** |
|---|---|---|---|---|---|---|
| A | -0.4085 | 73.63 | | BD | 0.0969 | 4.14 |
| B | 0.2812 | 34.88 | | CD | 0.0500 | 1.10 |
| C | -0.0191 | 0.16 | | ABC | 0.0905 | 3.61 |
| D | 0.2851 | 35.86 | | ABD | -0.0011 | 0.00 |
| AB | -0.1394 | 8.57 | | ACD | -0.0702 | 2.17 |
| AC | -0.0067 | 0.02 | | BCD | -0.0181 | 0.14 |
| AD | -0.0645 | 1.83 | | ABCD | 0.1061 | 4.97 |
| BC | 0.0491 | 1.06 | | s^2 | 0.00907 | |

The values in the effect column have been determined by subtracting the average response at the factor's low level from the average response at the factor's high level. The significance column has been calculated by dividing the effect of the factor by the error variance calculated from the

center-point replicates. It can be seen that the temperature, the water concentration, and wet-side flow rate main effects are all considered to be statistically significant. The two-factor interaction for temperature/water concentration has also been deemed significant by this analysis. Based on the significant effects, Equation 51 was developed to estimate the humidifier fixture performance.

$$\mu = \bar{\mu} + aT' + bC' + cV_d' + dT'C'$$

$$flux = 0.88 - 0.204T' + 0.141C' + 0.142V_d' - 0.070T'C' \quad \text{(Eq51)}$$

Where T represents the cell temperature, C represents the wet-inlet water concentration, $V_w$ is the wet-side flow rate and $V_d$ is the dry-side flow rate. These factors are in factor-level form according to the methods presented in Section 4.3. The results of the factorial analysis are compared to the factorial design experimental data in Figure 40.

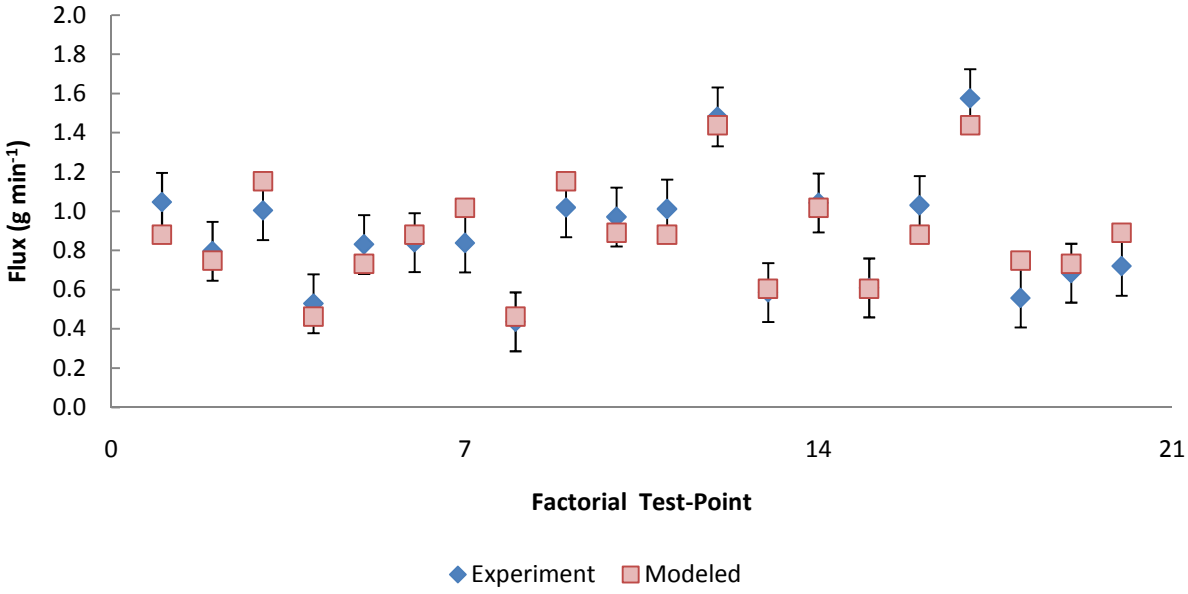


**Figure 40 - Factorial: Model comparison to experimental data**

By analyzing the significant effects it can be inferred that, due to wet-side flow rate being non-significant, the membrane surface on the wet-side may have significant condensation. A layer of liquid water blocking direct contact with the bulk air phase is an idea expanded upon in Section 4.4.2. The negative correlation with cell temperature can likely be attributed to the fact that a higher temperature would impede the formation of a liquid water layer on the wet-side

membrane surface. The temperature/concentration interaction term appears weakly significant and may play a part in the amount of this condensed liquid phase on the surface of the membrane due to the fact that a higher temperature at constant water concentration would represent a lower relative humidity within the fixture.

This method fits the experimental data quite well however it suffers from many of the same drawbacks of the previously discussed least squares equation namely that it cannot accommodate alternative membrane chemistry and that it exhibits poor scalability. One significant improvement made in this method is the inclusion of multi-variable factors. Fundamental statistical analysis procedures allow the insignificant terms to be dropped resulting in a relatively simple model that accounts for multi-factor behaviour.

## 5.5. MATLAB Simulation using Simple Water Coverage Model

Recall the water transfer performance under the liquid covered portion of the membrane is higher than the portion exposed to unsaturated air at the wet channel conditions. This property was used to tune the performance of the overall fixture adjusting the value of $\varepsilon_w$.

As presented in Section 4.4.2 a mathematical expression was developed to calculate the value of $\varepsilon_w$ based on the fixture operating conditions. The first-generation expression for $\varepsilon_w$ is presented below in Equation 52. Note the similarity to the least-squares method used in Figure 39 however the dry- and wet-side flow rate terms have been modified to space velocities. Recall that the space velocity is determined by dividing a flow rate (Q) by a flow volume (V). This modification to the model used to calculate $\varepsilon_w$ allows the MATLAB model to generate results for alternative membrane chemistries and channel geometries.

$$\varepsilon_w = -0.370 - 0.0318T + 1.42 * 10^{-4}T^2 - \frac{9.05*10^{-3}}{T} - \frac{1.65*10^{-4}}{T^2} - 0.0921SV_w + 5.82 * 10^{-4}SV_w^2 - \frac{0.0375}{SV_w} - \frac{2.75*10^{-3}}{SV_w^2} + 0.2201SV_d - 1.86 * 10^{-3}SV_d^2 - \frac{0.0385}{SV_d} - \frac{2.8*10^{-3}}{SV_d^2} - 0.0165RH + 0.2620RH^2 - \frac{0.5672}{RH} + \frac{0.1366}{RH^2} \quad \text{(Eq52)}$$

Where T is the temperature in °C, $SV_w$ is the wet-side dry-basis space volumes in $s^{-1}$, $SV_d$ is dry-side space volumes in $s^{-1}$ and RH is the relative humidity ratio. One should be careful not to use the relative humidity in terms of percent. An alternative style of $\varepsilon_w$ calculation using the

standard condition space velocities was determined to be less accurate than the model using the actual gas stream space velocities. Recall that standard conditions infer a pressure of one atmosphere and 0°C. Equation 52 was used to estimate $\varepsilon_w$ for use in several modeled operational scenarios. Model predictions for the standard operational test-point conditions can be found in Figure 41.

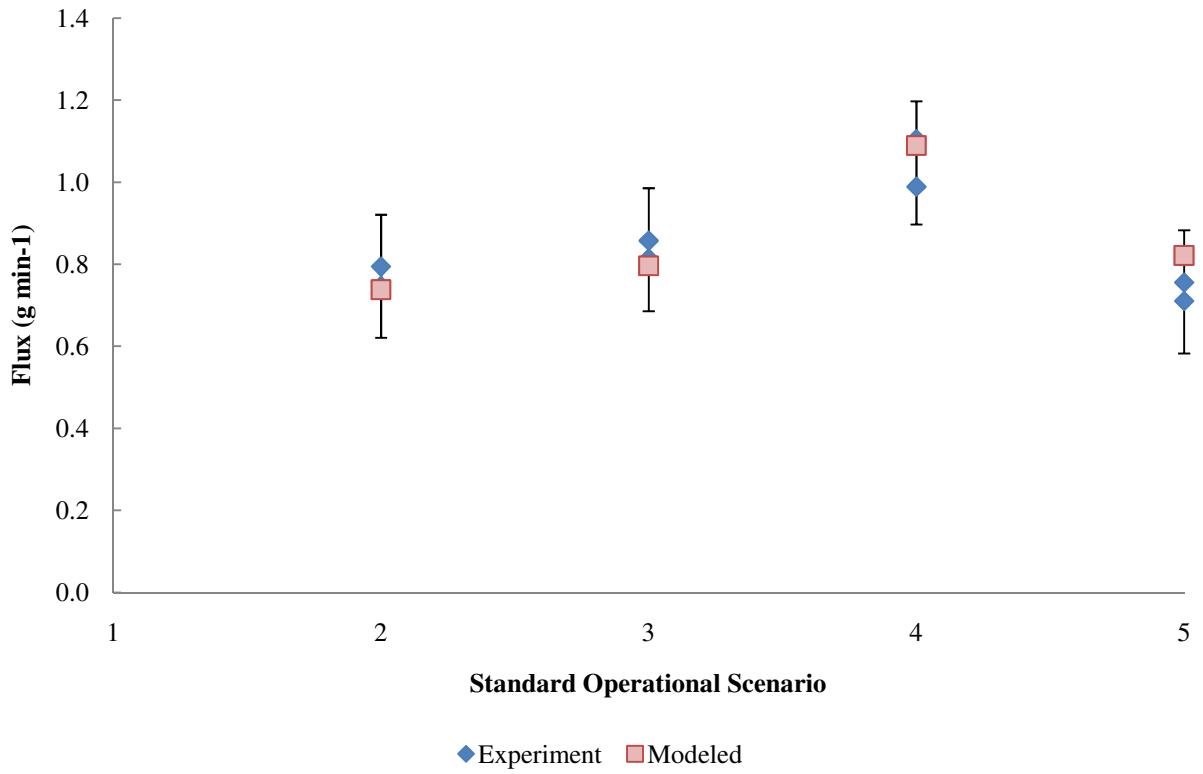


**Figure 41 - Simulation: Standard operational scenarios**

It would appear that the performance prediction model for the fuel cell humidifier can predict the fixture performance quite accurately for the standard operational scenarios. Each of the eight test results lay within the bounds for experimental error. Figure 42 contains the comparison of the model performance to the factorial design experimental data.

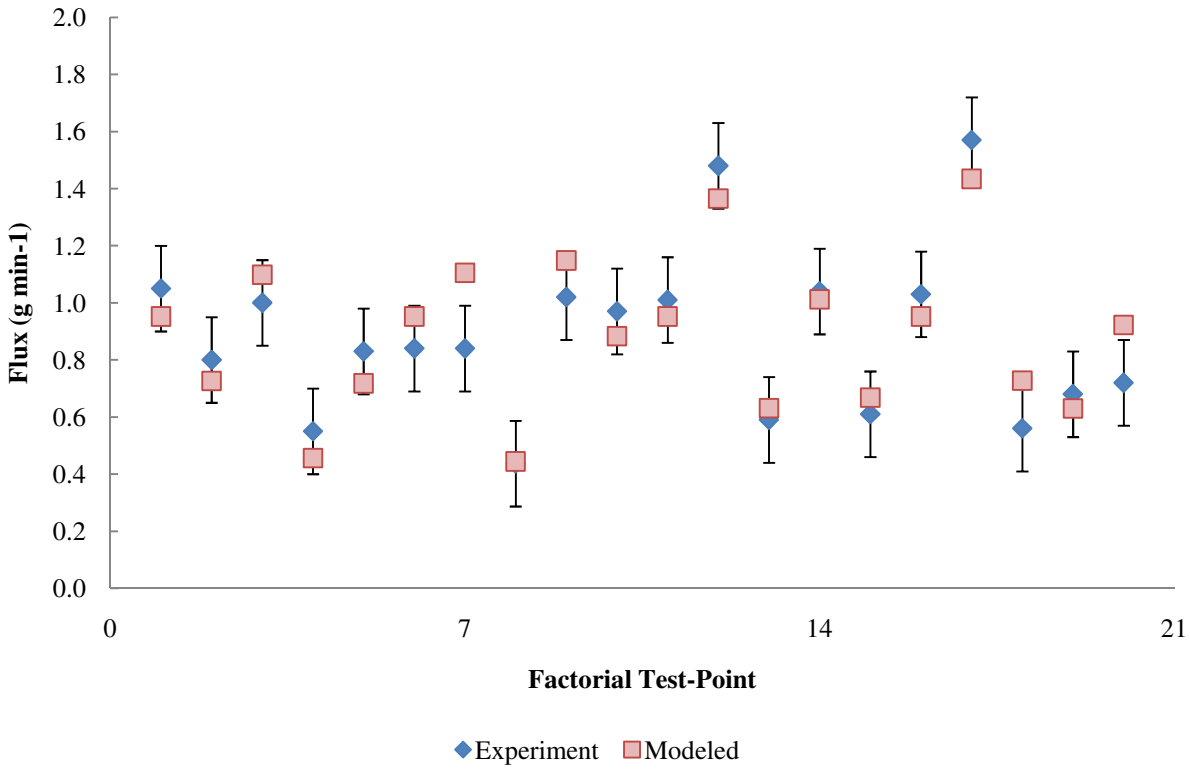


**Figure 42 - Simulation: Factorial design conditions**

In Figure 42 one can see that many of the experimental test-points are described within the experimental uncertainty. As previously touched upon, the only test-point that lies outside of the three standard deviation error bars is test-point 7. This non-agreement may well have more to do with experimental error than with model inadequacies. It has been demonstrated that this method can reproduce acceptable results however the water coverage estimation itself does not have a strong foundation in engineering principles. The linear regression optimization method used thus far could be described as a 'brute-force' method and has several significant drawbacks. Firstly the method can not apply well-developed regression methods since any regressor matrix made from the squared and inverse square terms will be ill-conditioned. A second drawback, which stems from the first, is that the method is susceptible to local minimum behaviour that cannot be accounted for in this optimization technique. Finally this method does not include any multi-factor interaction terms. One should keep these drawbacks in mind as Section 5.6 presents several advanced water coverage models that forego these drawbacks.

## 5.6. Simulation using Advanced Water Coverage Models

A significant drawback of the water coverage model introduced in Section 5.5 is that it is relatively complex. The Excel Solver-based model also does not include the multi-factor effects that a factorial design derived model would include. This section contains the results of several prototype models generated to replace the existing water coverage model.

### 5.6.1. Water Coverage based on Fixture Flux Factorial Model (Concentration)

This theoretical model was generated using the factorial design model presented in Section 5.4 as a template. It was conjectured that the terms that were deemed significant for factorial design model based on the overall fixture flux could sufficiently describe the physical phenomenon within the cell. Equation 53 below illustrates the proposed replacement model.

$$\varepsilon_w = \beta_1 + \beta_2 T' + \beta_3 C' + \beta_4 SV_d^{O\prime} + \beta_5 T'C' \qquad \text{(Eq 53)}$$

Note that this model can be solved using a standard linear regression approach instead of the inexact Excel Solver method employed in Section 5.5. Equation 53 also includes coded variables in order to avoid generating a singular regressors matrix. Additionally the dry space velocity term is based on the standard space velocity which is calculated by taking the volumetric flow rate at one atmosphere and 0°C and dividing by the flow volume. In this case the flow volume consists of the total volume contained within the dry-side channels. Table 17 below presents the calculations used to convert from non-coded form to the form used in the least squares model.

**Table 17 - Coding conversions for water coverage models**

| Coded Value | Calculation |
|---|---|
| T' | $\frac{(T-85)}{5}$ |
| C' | $\frac{(C-11.814)}{3.243}$ |
| $SV_d{}^O{}'$ | $\frac{(SV_d{}^O-51.268)}{12.954}$ |

The calculated best-fit model for this scenario is presented below in Equation 54.

$$\varepsilon_w = 0.3101 - 0.1270T' + 0.0564C' + 0.1231SV_d^{O\prime} - 0.0372T'C' \quad \text{(Eq 54)}$$

Another similar method based on the general structure of the fixture flux regression model can be found in the next section. A summary and comparison of all proposed water coverage determination methods are found in Section 5.6.4.

### 5.6.2. Water Coverage based on Fixture Flux Factorial Model (RH)

This method is nearly identical to the method in Section 5.6.1 however the relative humidity of the inlet wet stream has been exchanged for the water concentration term. The relative humidity term was coded in a similar fashion as the previous method and is shown in Table 18.

**Table 18 - Additional coding conversion for RH-based water coverage models**

| Coded Value | Calculation |
|---|---|
| RH' | $\frac{(RH-0.713)}{0.219}$ |

The linear regression model based on this modification can be found below in Equation 55.

$$\varepsilon_w = 0.3277 - 0.0459T' + 0.1399RH' + 0.1230SV_d^{O\prime} + 0.0111T'RH' \quad \text{(Eq 55)}$$

The next section proposes a factorial design method employed directly for determining an $\varepsilon_w$ model. Comparisons between this and other methods of calculating the theoretical water coverage can be found in Section 5.6.4.

### 5.6.3. Water coverage as a dependent variable in factorial analysis

The hypothesis put forward in Section 5.6.1 has a significant flaw in the assumption that a regression model generated to calculate overall fixture flux can be applied to make a new model that calculates the fractional water coverage within the cell. A factor that increases the overall water transfer in the macroscopic model could have no effect on the microscopic water coverage or even may potentially decrease the fractional coverage. For example an increased gas flow rate could increase the macroscopic performance due to increased driving force across the membrane however this increased gas flow could suppress the formation of a liquid layer.

The factorial design approach can be still be applied using the existing factorial design data assuming the fractional water coverage is used as the dependent variable instead of the overall fixture flux. The results of this water coverage focused regression analysis are summarized below in Table 19.

**Table 19 - Water coverage factorial design effects**

| Factor | Effect | Significance | | Factor | Effect | Significance |
|---|---|---|---|---|---|---|
| A | -0.2538 | 53.38 | | BD | 0.1138 | 10.73 |
| B | 0.1113 | 10.26 | | CD | 0.04375 | 1.587 |
| C | -0.03375 | 0.9443 | | ABC | 0.07625 | 4.820 |
| D | 0.2463 | 50.27 | | ABD | -0.00375 | 0.01166 |
| AB | -0.0713 | 4.209 | | ACD | -0.09375 | 7.286 |
| AC | 0.00875 | 0.06347 | | BCD | -0.01875 | 0.2915 |
| AD | -0.1013 | 8.499 | | ABCD | 0.07375 | 4.509 |
| BC | 0.02375 | 0.4676 | | | | |

Recall that factor A represents the coded temperature and factor B represents the coded water concentration. In order to account for alternative gas flow channel geometries factors C and D have been changed to represent the wet and dry standard condition space volumes through the

fixture. The mathematical model developed from the significant effects can be found below in Equation 56.

$$\varepsilon_w = 0.31 - 0.127T + 0.056C' + 0.123SV_d^{O\prime} - 0.051T'SV_d^{O\prime} + 0.057C'SV_d^{O\prime} \quad \text{(Eq 56)}$$

It should be made clear that model presented above was generated using only the data collected as part of the factorial design experiment. The results of this factorial analysis were used to generate two additional regression models based on the entire set of collected data using methods similar to those discussed in Sections 5.6.1 and 5.6.2. The regression model for the concentration-based analysis can be found below in Equation 57.

$$\varepsilon_w = 0.322 - 0.143T' + 0.152C' + 0.071SV_d^{O'} - 0.005T'SV_d^{O\prime} + 0.217C'SV_d^{O\prime} \quad \text{(Eq 57)}$$

One can see that by including the full set of data, the resulting regression model has similar but slightly modified regressor coefficients. The associated RH-based regression model is presented in Equation 58.

$$\varepsilon_w = 0.409 - 0.044T' + 0.178RH' + 0.199SV_d^{O\prime} + 0.144T'SV_d^{O\prime} + 0.276RH'SV_d^{O\prime} \quad \text{(Eq 58)}$$

Several methods of water coverage estimation have been presented thus far. Refer to Section 5.6.4 for an analysis of the accuracy associated with these models.

### 5.6.4. Water Coverage Model Selection

Up to this point three major subclasses of water coverage model have been put forward for consideration. The first subclass is the general model for which the squared, inverse and inverse squared terms are included for each factor. This subclass exhibits two significant drawbacks: it does not include any two-factor interaction terms and it must be calculated using Excel's Solver add-in. Two models were developed using this framework: one based on water concentration and one based on stream relative humidity.

The second model subclass is based on the fixture performance factorial regression model developed in Section 5.4. This model uses the factors deemed significant for the overall fixture flux. Again both water concentration and relative humidity were considered as separate models.

The final model subclass directly applies factorial design concepts with the theoretical water coverage as the dependent variable. The resulting significant factors are subtly different than those for when the fixture performance is used as the dependent variable. The original experimental data collected used water concentration as an independent variable however regression analysis can still be used when concentration is replaced with relative humidity. It was assumed that the fractional water coverage was affected by the fixture temperature, the wet-side inlet relative humidity, the wet-side gas stream flow rate and the dry-side gas stream flow rate. Recall that the MATLAB model assumes that the entire dry-side membrane surface is exposed to the water vapour concentration present in the bulk stream above the GDM.

Table 20 below presents the general form for each of these 6 hypothetical models. The models are numbered for brevity in subsequent analyses.

**Table 20 - Water coverage models: General forms**

| Model | General Equation |
|---|---|
| 1 | $\varepsilon_w = \beta_0 + \beta_1 T + \beta_2 T^2 + \frac{\beta_3}{T} + \frac{\beta_4}{T^2} + \beta_5 SV_w + \beta_6 SV_w^2 + \frac{\beta_7}{SV_w} + \frac{\beta_8}{SV_w^2} + \beta_9 SV_D + \beta_{10} SV_D^2 + \frac{\beta_{11}}{SV_D} + \frac{\beta_{12}}{SV_D^2} + \beta_{13} RH + \beta_{14} RH^2 + \frac{\beta_{15}}{RH} + \frac{\beta_{16}}{RH^2}$ |
| 2 | $\varepsilon_w = \beta_0 + \beta_1 T + \beta_2 T^2 + \frac{\beta_3}{T} + \frac{\beta_4}{T^2} + \beta_5 SV_w + \beta_6 SV_w^2 + \frac{\beta_7}{SV_w} + \frac{\beta_8}{SV_w^2} + \beta_9 SV_D + \beta_{10} SV_D^2 + \frac{\beta_{11}}{SV_D} + \frac{\beta_{12}}{SV_D^2} + \beta_{13} C_w + \beta_{14} C_w^2 + \frac{\beta_{15}}{C_w} + \frac{\beta_{16}}{C_w^2}$ |
| 3 | $\varepsilon_w = \beta_0 + \beta_1 T' + \beta_2 RH' + \beta_3 SV_d^{O\prime} + \beta_4 T' RH'$ |
| 4 | $\varepsilon_w = \beta_0 + \beta_1 T' + \beta_2 C' + \beta_3 SV_d^{O\prime} + \beta_4 T' C'$ |
| 5 | $\varepsilon_w = \beta_0 + \beta_1 T' + \beta_2 RH' + \beta_3 SV_d^{O\prime} + \beta_4 T' SV_d^{O\prime} + \beta_5 RH' SV_d^{O\prime}$ |
| 6 | $\varepsilon_w = \beta_0 + \beta_1 T' + \beta_2 RH' + \beta_3 SV_d^{O\prime} + \beta_4 T' SV_d^{O\prime} + \beta_5 C' SV_d^{O\prime}$ |

Model 1 is the least squares model determined using Excel's Solver that includes the wet-inlet RH as an independent variable while Model 2 an equivalent model in which the RH is replaced with the wet-inlet water concentration in mol $m^{-3}$. Models 3 and 4 use the prototype regression model deemed statistically significant as part of the fixture performance-based factorial design

experiment. Model 3 is based on the wet-side inlet RH while Model 2 is based on the wet inlet water concentration. Finally Models 5 and 6 use the prototype regression model developed using factorial design analysis where fractional water coverage is the dependent variable.

The accuracy of each of these methods shall be evaluated by comparing their sums of squared error. Assuming the same sets of data are compared this method would provide a relatively reliable indicator that can be calculated for each method. Table 21 presents the sums of squared error based on all available experimental data.

**Table 21 - Water coverage: Error sums for all data**

| Model | Overall Sum of Squared Error |
|---|---|
| 1 | 0.2696 |
| 2 | 0.3016 |
| 3 | 0.4614 |
| 4 | 0.4342 |
| 5 | 0.3301 |
| 6 | 0.3515 |

Note that the two models with the lowest sums of squares were bolded for emphasis. It appears the GRG2 algorithm used for the simple regression methods provide the lowest overall sum of squares. The models derived by the water coverage factorial design method predict $\varepsilon_w$ more accurately than the regression models based on the humidifier performance factorial models. It is interesting to note that the relative humidity based models tend to have a lower sum of squares than the concentration based models. Even though the relative humidity models tend to have a lower sum of squared error one should keep in mind that the factorial design experiments used to derive these models were performed with water concentration as a factor and not relative humidity of the inlet stream. These same theoretical models were applied using only the factorial design subset of data. The sum of squares for this particular set of cases is found below in Table 22.

**Table 22 - Water coverage: Error sums for factorial data**

| Model | Factorial Sum of Squared Error |
|---|---|
| 1 | 0.1727 |
| 2 | 0.1998 |
| 3 | 0.2555 |
| 4 | 0.2396 |
| 5 | 0.1468 |
| 6 | 0.1652 |

One should note here that the two lowest sums of squares are attributed to the regression models based on the water coverage factorial method. The lowest error is associated with the relative humidity-based model based on the findings of the factorial design methods in Section 5.6.3. The second lowest error was observed in the model derived directly in Section 5.6.3.

Comparison of the squared error sums in Table 21 and Table 22 show that while Model 5 is suitable for the factorial design set of data it exhibits more error than the simple regression method when including other data such as the standard operational scenarios. Assessing the error sums associated with Model 5 indicate that it may be a reasonable alternative to the simple Excel Solver derived Model 1. Figure 43 presents the standard operational scenario experimental data, estimated performance based on Model 1 and estimated performance based on Model 5. Recall that Model 5 represents a method of calculating the fractional water coverage that was determined by factorial design analysis to be a prototype model for which only the statistically significant effects are present. This factorial analysis along with a low overall sum of squared error indicated that Model 5 was the most representative method of the six investigated.

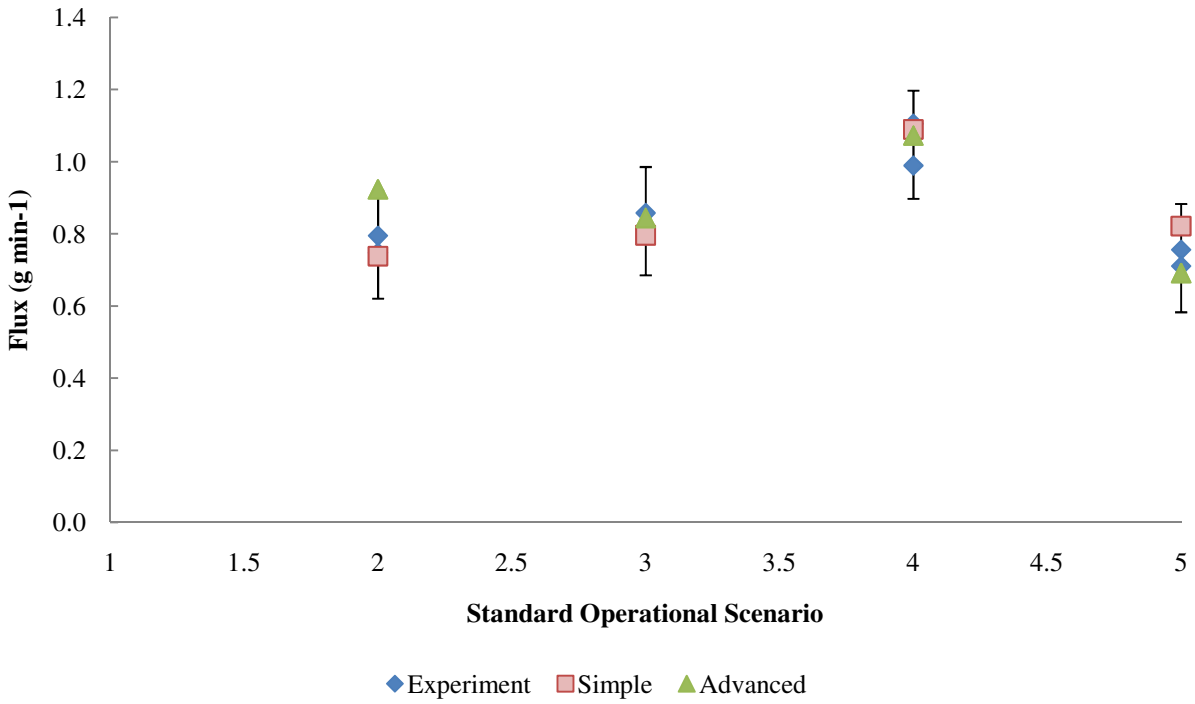


**Figure 43 - Advanced water coverage: Standard scenario comparison to simple method**

Note that neither model appears to fit the experimental data better than the other. While the advanced method over-estimates the performance in Scenario 2 the simple method over-estimates the fixture performance in Scenario 5. The same comparison for factorial design data can be found below in Figure 44.

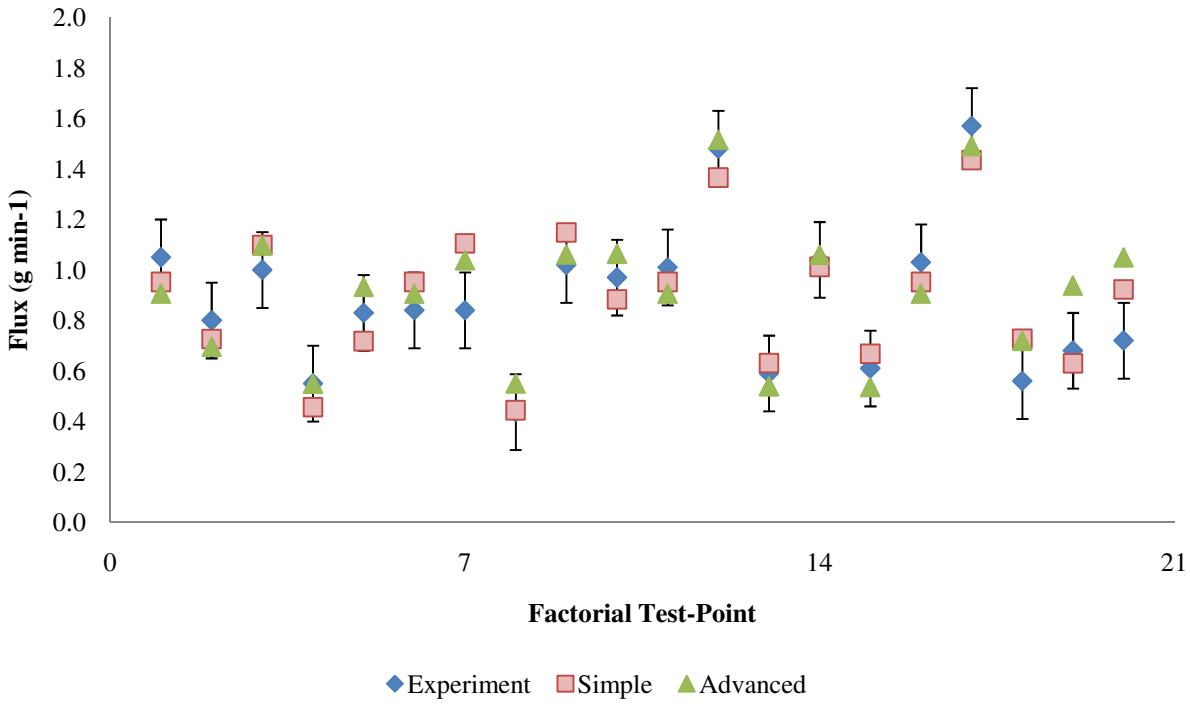


**Figure 44 - Advanced water coverage: Factorial data comparison to simple method**

The advanced method does not seem to predict the behaviour any better or worse than the simple method. Test-point 7 continues to be outside the predictive range of both water coverage methods, as initially discussed in Section 5.3. Both methods maintain the ability to predict overall humidifier performance within the bounds of experimental error. Since both models appear to have valid areas of operation, both were included in the final thesis program.

## 5.7. Simulated Performance Dependence on Single Factors

This section shall present simulated results generated by modifying a single factor while all other factors are kept constant. The factors investigated in this section include: wet-flow rate, dry-flow rate, wet inlet relative humidity (RH), cell temperature with water concentration held constant and cell temperature with RH held constant.

The behaviour of these dependence plots is highly dependent on the water coverage calculation method employed and as such Models 1 and 5 from the previous section shall be considered. The first single-factor to be considered is the wet-flow dependence based on the simple regression model and is illustrated below in Figure 45.

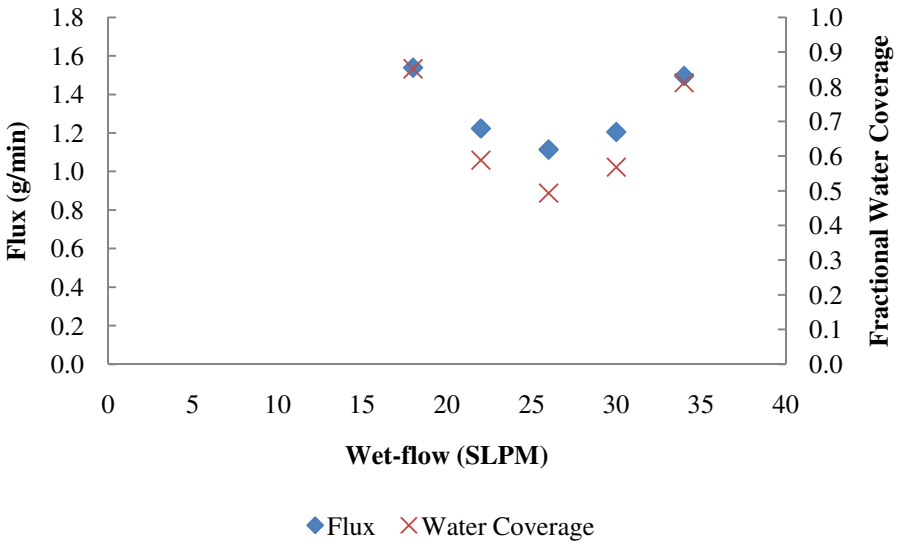


**Figure 45 - Simple model: Wet-flow performance effect**

Here a very prominent non-linear wet-flow effect can be observed for both the overall fixture flux and the calculated fractional water coverage. Before this behaviour is discussed in behaviour, the same wet-flow effect should be investigated using Model 5 from Section 5.6.4. The wet-flow single-factor dependence generated using this advanced model can be found in Figure 46.

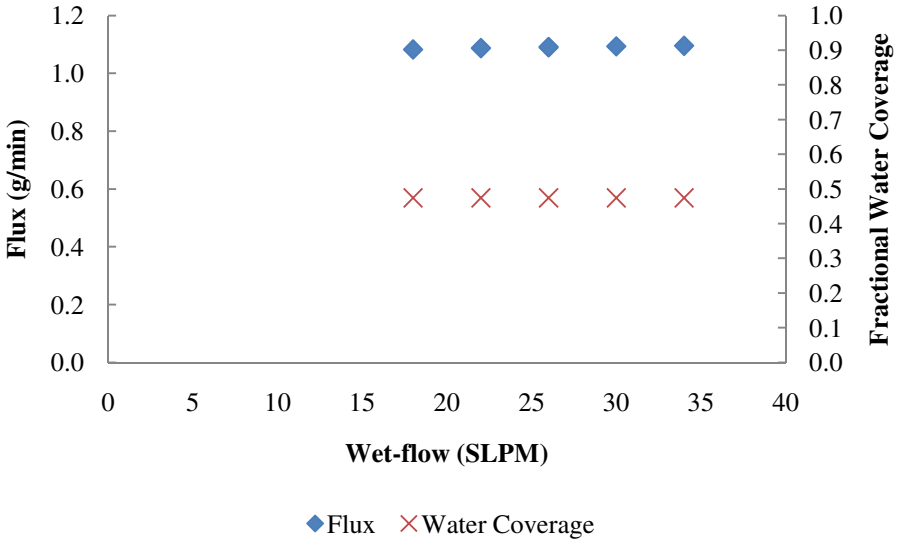


**Figure 46 - Advanced model: Wet-flow performance effect**

One can see that using this model the wet-side flow rate has little effect on the overall humidifier performance. Previously discussed factorial design investigations determined that wet-side flow rate was not significant for either the fractional water coverage or the overall fixture performance. It is thus theorized that, for the remainder of the single-factor performance effects, the advanced model should be the preferred method of analysis. The dry-flow performance effect is the next factor to be presented in Figure 47.

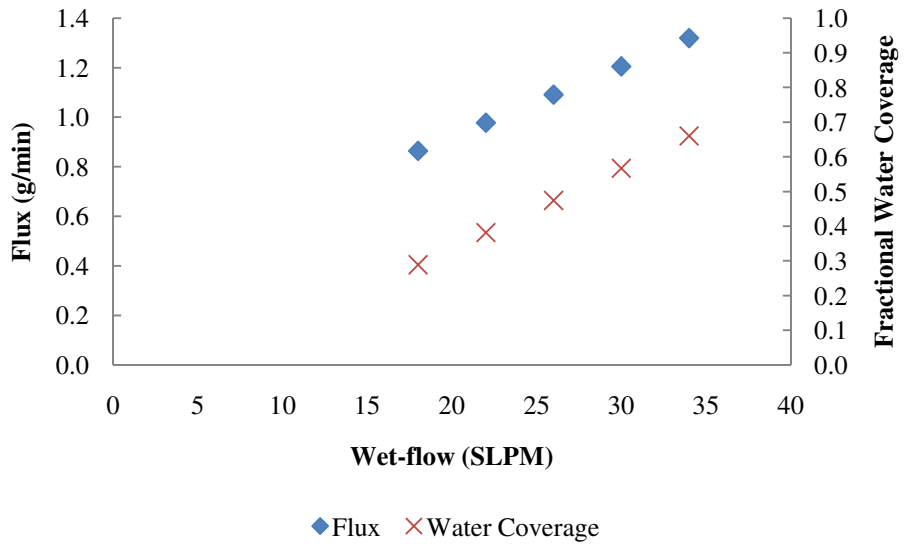


**Figure 47 - Advanced model: Dry-flow performance effect**

Note the performance of the humidifier fixture is over 50% higher at 34 SLPM compared to the operation at 18 SLPM. The current model assumes an absence of liquid water on the dry side however the positive water coverage trend indicates that perhaps the model does not completely describe the physical behaviour on the dry side. The increased humidifier performance with increased dry-flow rate makes sense from a simple mass transfer standpoint however an increased dry-flow rate should not result in increased wet-side fractional water coverage. An increased dry-flow would increase overall fixture performance by affecting the driving force across the membrane however an increased amount of liquid water on the wet-side would not be observed. This behaviour might indicate an evaporative situation at some nodes for which an increased dry-side gas flow rate would improve mass transfer however the model accounts for this increase in performance by increasing the theoretical wet-side fractional water coverage. The fixture operating temperature is the next factor to be presented in Figure 48 and Figure 49.

Note that the trends depicted in Figure 48 represent the temperature dependence assuming the wet inlet stream remains at a constant 80% RH.

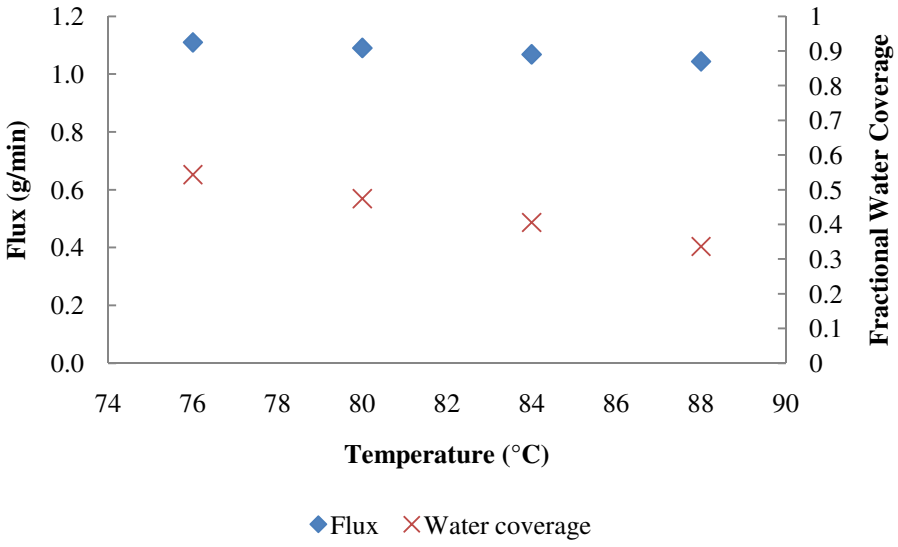


**Figure 48 - Advanced model: Temperature performance effect (constant RH)**

One should note that in this situation fixture temperature only weakly affects humidifier performance. Note that the mass of water injected at the 88°C operating scenario is nearly three times as much as the 76°C scenario. The following behaviour exhibited in Figure 49 was generated for a series of temperatures for which the molar water concentration was held at 12.9 mol $m^{-3}$.

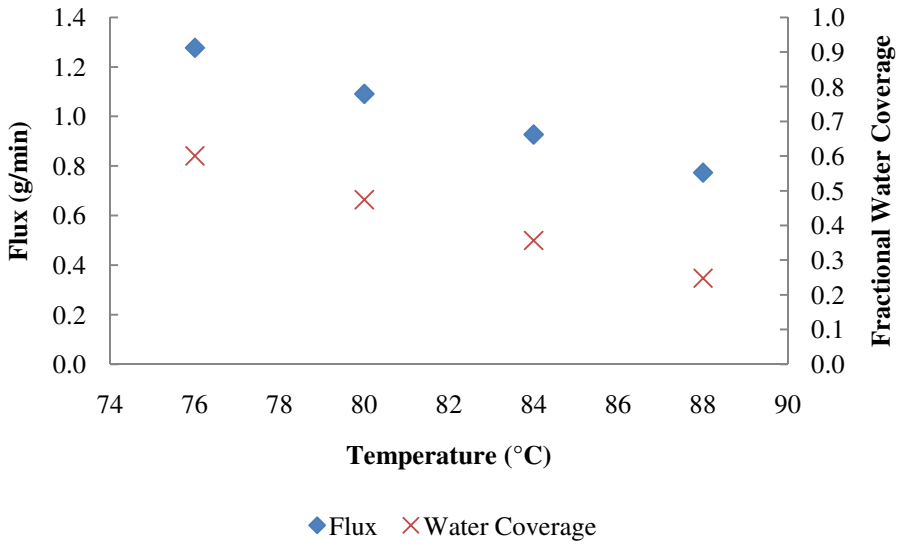


**Figure 49 - Advanced model: Temperature performance effect (constant concentration)**

Figure 49 shows that increased temperature can significantly reduce the effectiveness of the humidifier fixture for gas streams at a constant concentration. It is evident that the primary effect of increased temperature is a marked reduction in wet-side fractional water coverage. The situations in Figure 48 and Figure 49 illustrate a very important point one must consider when integrating this humidifier into a fuel cell system. For situations in which temperature fluctuates considerably, the stream conditions will tend to constant-concentration behaviour over constant-RH behaviour. Under such conditions even a few degrees instability could drastically affect the operation of the fuel cell humidifier.

## 5.8. Two-Factor Map: Concentration and Temperature

A series of simulated conditions were modeled with the intent of illustrating the multi-factor behaviour of the fixture performance. The effect of both temperature and wet-inlet water concentration on the simulated water flux are shown below in Figure 50. Several of the simulated conditions also have matching experimental data collected as part of the factorial design experiment and these points have been included where appropriate. Note that all test-points were run with wet- and dry-side flow rates at 21 SLPM.

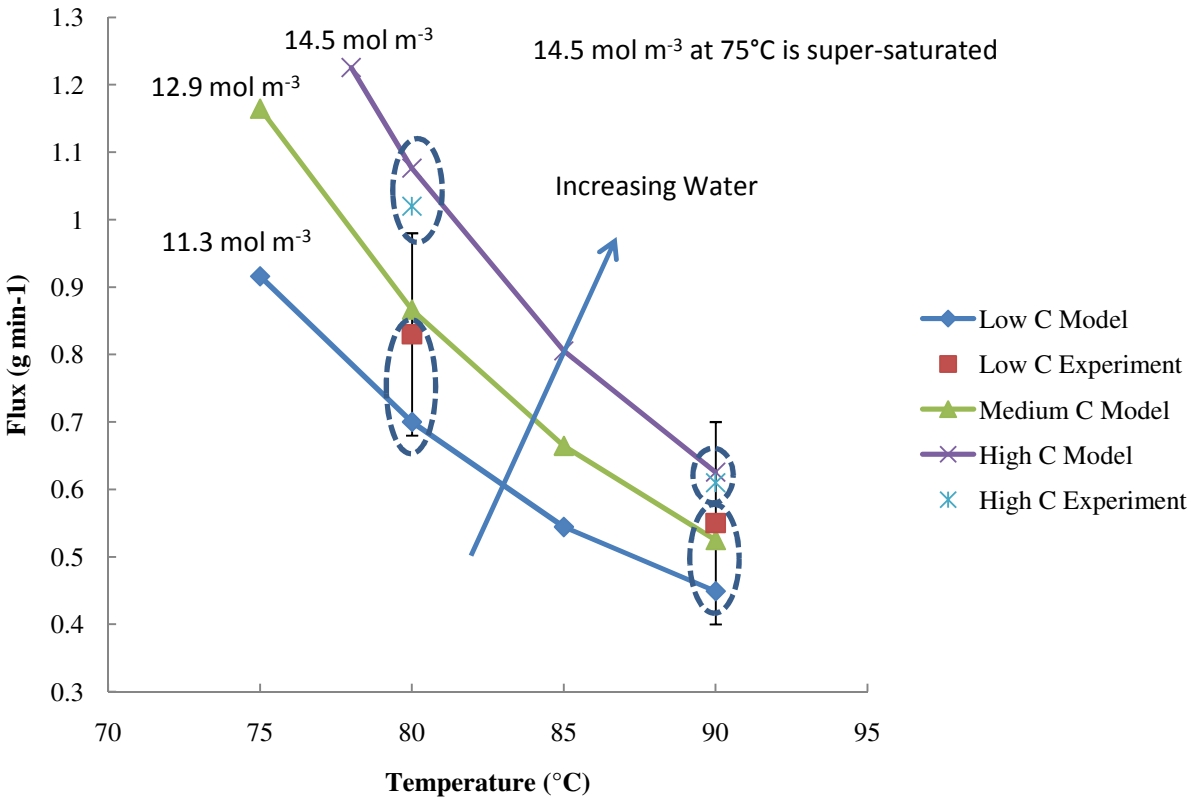


**Figure 50 - Cell performance: Dependence on two-factor effects**

## 5.9. Aspect Ratio Effect on Performance

It was conjectured that modifying the ratio of wet channels to dry channels could affect the overall performance of the humidifier fixture. The humidifier fixture used in these experiments contains 87 dry channels and 31 wet channels which results in a 2.8 aspect ratio of dry channels to wet channels. This particular combination of dry and wet channels results in 2697 intersectional nodes. At 85°C and 26 SLPM dry-basis flow rates for both sides the simulated performance was 0.93 g·min$^{-1}$. A series of additional simulations were performed in which the number of dry channels and wet channels were changed while keeping the number of intersectional nodes as close as possible to 2697. The simulated results of changing the aspect ratio can be found below in Figure 51 however bear in mind that these results are fully simulated and do not include any experimental data.

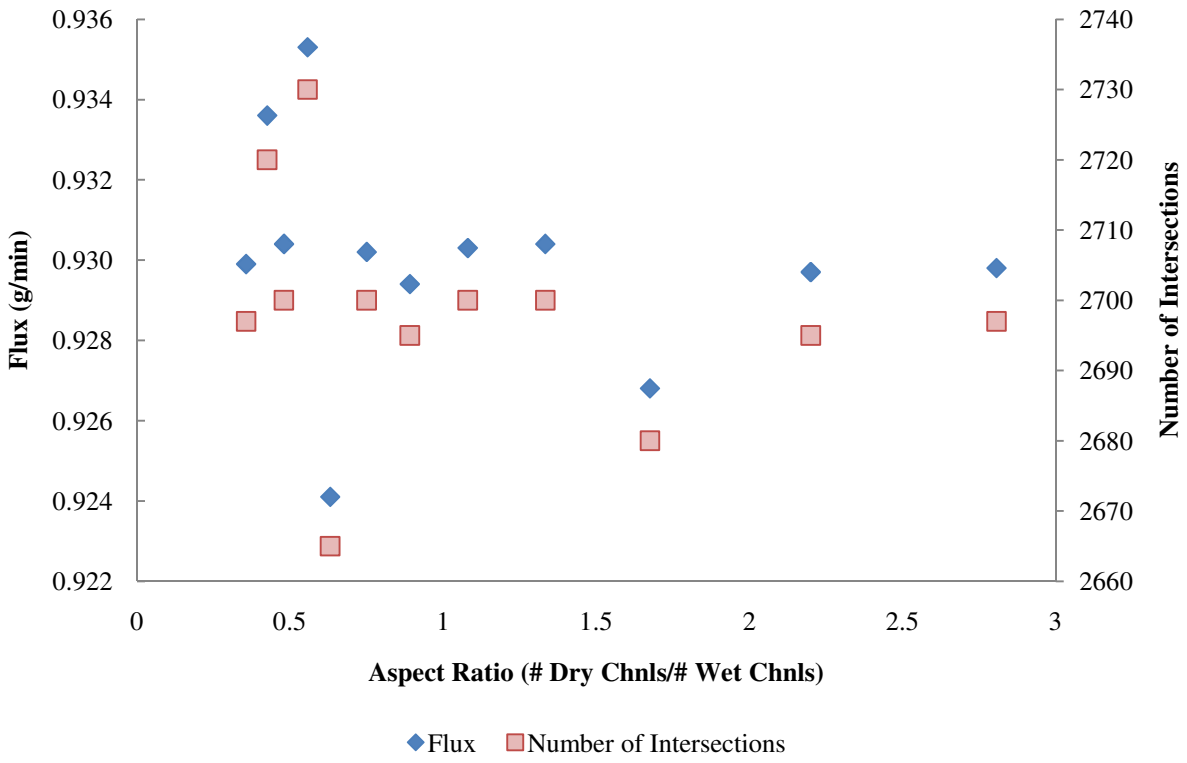


**Figure 51 - Simulation: Aspect ratio effects investigation**

One can see that there are slight variations in humidifier fixture performance for different operational scenarios. The total number of intersections was also presented on the secondary axis in order to show that the performance variations were due to small changes in the total available operational area. Investigation of each of these test cases reveals that the performance at the minimum nodal flux is at least 96% of the maximum nodal flux. Further investigation of the simulation results reveals that the wet outlet stream contains nearly 92% of the water content in the wet inlet stream entering the fixture. The driving force for water transport within this fixture is the difference in water concentration between the wet and dry sides of the membrane. It can be concluded that for the standard operational scenarios the water content of the gas streams does not vary enough for the aspect ratio of this humidifier to impact the performance.

## 5.10. Non-constant water coverage investigation

Results presented thus far have been generated under the assumption that the fractional water coverage is a constant value for all computational nodes. It was hypothesized that the actual conditions within the cell were likely better represented by a non-constant nodal water coverage

based on the node's location in the cell. Note that for this section of analysis, all modeled results are based on the factorial design center-point conditions. These conditions are summarized below in Table 23. Note that the space velocities are calculated on a dry-stream basis.

**Table 23 - Factorial design center-point experimental conditions**

| T (°C) | Dry SV ($s^{-1}$) | Wet SV ($s^{-1}$) | Wet Inlet RH | Flux (g $min^{-1}$) |
|---|---|---|---|---|
| 85 | 56.1 | 77.4 | 0.682 | 1.03 |

The first suggested water coverage array was generated under the assumption that the nodes close to the wet inlet are fully covered by liquid water and the remaining nodes experience zero water coverage. The number of saturated nodes for each wet flow channel was adjusted until the modeled results matched the results observed during experimentation. The appropriate array of nodal water coverages can be found below in Figure 52.

| | | ⇩ Dry Inlets | | | | | | | |
|---|---|---|---|---|---|---|---|---|---|
| | | i=1 | i=2 | | i=38 | i=39 | | i=77 | i=78 |
| -> | j=1 | 1 | 1 | 1 | 1 | 0 | 0 | 0 | 0 |
| -> | j=2 | 1 | 1 | 1 | 1 | 0 | 0 | 0 | 0 |
| Wet Inlets | | 1 | 1 | 1 | 1 | 0 | 0 | 0 | 0 |
| -> | j=30 | 1 | 1 | 1 | 1 | 0 | 0 | 0 | 0 |
| -> | j=31 | 1 | 1 | 1 | 1 | 0 | 0 | 0 | 0 |

**Figure 52 - Continuous water coverage: Fully saturated or no liquid nodal model**

It was determined that the $\varepsilon_w$ array of this type to match the experimental fixture performance of 1.03 g $min^{-1}$ required each wet channel to have 38 nodes of fully saturated membrane. The sudden drop from full liquid water coverage to zero liquid water is surely not representative of how the liquid water would be distributed in a real system however this case has been included as an interesting theoretical concept. The second case to be investigated was the situation in which the "wet inlet-dry outlet" intersection was fully covered in liquid water while the "wet outlet-dry inlet" intersection had zero water coverage. The remainder of the array was

designated such that the water coverage varied linearly from one to zero. The proposed array is presented below in Figure 53.

| | | ↓ | ↓ | ↓ | Dry Inlets | | | ↓ | ↓ | ↓ |
|---|---|---|---|---|---|---|---|---|---|---|
| | | i=1 | i=2 | | i=38 | i=39 | | i=77 | i=78 | |
| -> | j=1 | 0.74 | 0.73 | | 0.42 | 0.41 | | 0.01 | 0 | |
| -> | j=2 | 0.75 | 0.74 | | 0.43 | 0.42 | | 0.02 | 0.01 | |
| Wet Inlets | | | | | | | | | | |
| -> | j=30 | 0.99 | 0.98 | | 0.67 | 0.66 | | 0.26 | 0.25 | |
| -> | j=31 | 1 | 0.99 | | 0.68 | 0.67 | | 0.27 | 0.26 | |

**Figure 53 - Continuous water coverage: Maximum of 1 to minimum of 0 model**

This water coverage array resulted in a modeled performance of 1.12 $g \cdot min^{-1}$ which was significantly higher than the observed 1.03 $g \cdot min^{-1}$. Evidently the water coverage in this situation is too high and the maximum water coverage must be lower than 1. Subsequently the maximum value was varied in order to match the modelled results to experimental data. It was observed that the overall fixture performance matched when the maximum water coverage at the "wet inlet-dry outlet" node was set to 0.86 as illustrated in Figure 54.

| | | ↓ | ↓ | ↓ | Dry Inlets | | | ↓ | ↓ | ↓ |
|---|---|---|---|---|---|---|---|---|---|---|
| | | i=1 | i=2 | | i=38 | i=39 | | i=77 | i=78 | |
| -> | j=1 | 0.64 | 0.63 | | 0.36 | 0.36 | | 0.01 | 0 | |
| -> | j=2 | 0.65 | 0.64 | | 0.37 | 0.36 | | 0.01 | 0.01 | |
| Wet Inlets | | | | | | | | | | |
| -> | j=30 | 0.85 | 0.85 | | 0.58 | 0.57 | | 0.22 | 0.22 | |
| -> | j=31 | 0.86 | 0.85 | | 0.59 | 0.58 | | 0.23 | 0.22 | |

**Figure 54 - Continuous water coverage: Maximum of 0.86 to minimum of 0 model**

The modeled results using a continuous water coverage array from 0.86 to 0 matched the results observed during experimentation. The array presented in Figure 54 represents only one of an

infinite number of arrays that could be generated to recreate the experimental performance. For example a similar array with several nodes at zero water coverage could be balanced by higher maximum water coverage. Examination of the model results indicated that the wet outlet gas stream generally contained 90-94% of the water fed to the fixture. As such it was proposed that the water coverage should change no more than water content of the gas stream. For the factorial design center-point a flux of 1.03 $g \cdot min^{-1}$ indicates that the wet outlet stream contains 91% of the water in the wet inlet stream. The water coverage array presented in Figure 55 has a minimum water coverage value 91% of the maximum water coverage as well as matching the experimental fixture performance requirement.

| | | ↓ | ↓ | ↓ | Dry Inlets | | ↓ | ↓ | ↓ |
|---|---|---|---|---|---|---|---|---|---|
| | | i=1 | i=2 | | i=38 | i=39 | | i=77 | i=78 |
| -> | j=1 | 0.44 | 0.44 | | 0.43 | 0.43 | | 0.41 | 0.41 |
| -> | j=2 | 0.44 | 0.44 | | 0.43 | 0.43 | | 0.41 | 0.41 |
| Wet Inlets | | | | | | | | | |
| -> | j=30 | 0.45 | 0.45 | | 0.44 | 0.44 | | 0.42 | 0.42 |
| -> | j=31 | 0.45 | 0.45 | | 0.44 | 0.44 | | 0.42 | 0.42 |

**Figure 55 - Continuous water coverage: Maximum of 0.45 to minimum of 0.41 model**

It is hypothesized that this final representation of non-uniform water coverage most accurately recreates the conditions within the operation fuel cell humidifier fixture. Comparison to the uniformly distributed water coverage model yields very interesting results. A uniform coverage of 0.43 generates a modeled water flux of 1.0336 $g \cdot min^{-1}$ compared to the Figure 55 gradient coverage result of 1.0332 $g \cdot min^{-1}$; indicating that both methods result in similar findings. Large water content variation through the wet channels may necessitate the use of a non-uniform water layer however for the fixture performance demonstrated in these trials a uniformly distributed liquid water layer may adequately describe the process.

## 5.11. Enthalpy Balance Calculations

Post-run analysis of the wet- and dry-side outlet gas stream temperatures revealed that the wet-side temperature often dropped considerably lower than the PID controlled fixture temperature.

It was also observed that the dry-side temperature was often higher than the fixture temperature. These unexpected temperature behaviours indicated that the humidifier fixture heaters may not have been operating ideally. These heaters are used to replenish the enthalpy lost to the environment during operation such that the overall enthalpy of the system remains constant. Enthalpy will be transferred from the wet stream to the dry stream in the form of water vapour however the total enthalpy in the inlet streams should balance the enthalpy in the outlet streams. It was hypothesized that performing an enthalpy balance on the humidifier streams may illustrate any unexpected behaviour in the fixture heating system.

Analysis of the factorial design test run indicated that nearly every experimental run exhibited an overall loss in enthalpy in the outlet streams. Only the tenth run shows an overall increase in stream enthalpy. Through investigation of the raw data it was discovered that the dry inlet temperature was 10°C higher than the wet inlet and fixture set-points, which indicates an experimental error. The enthalpy calculation results are summarized below in Figure 56.

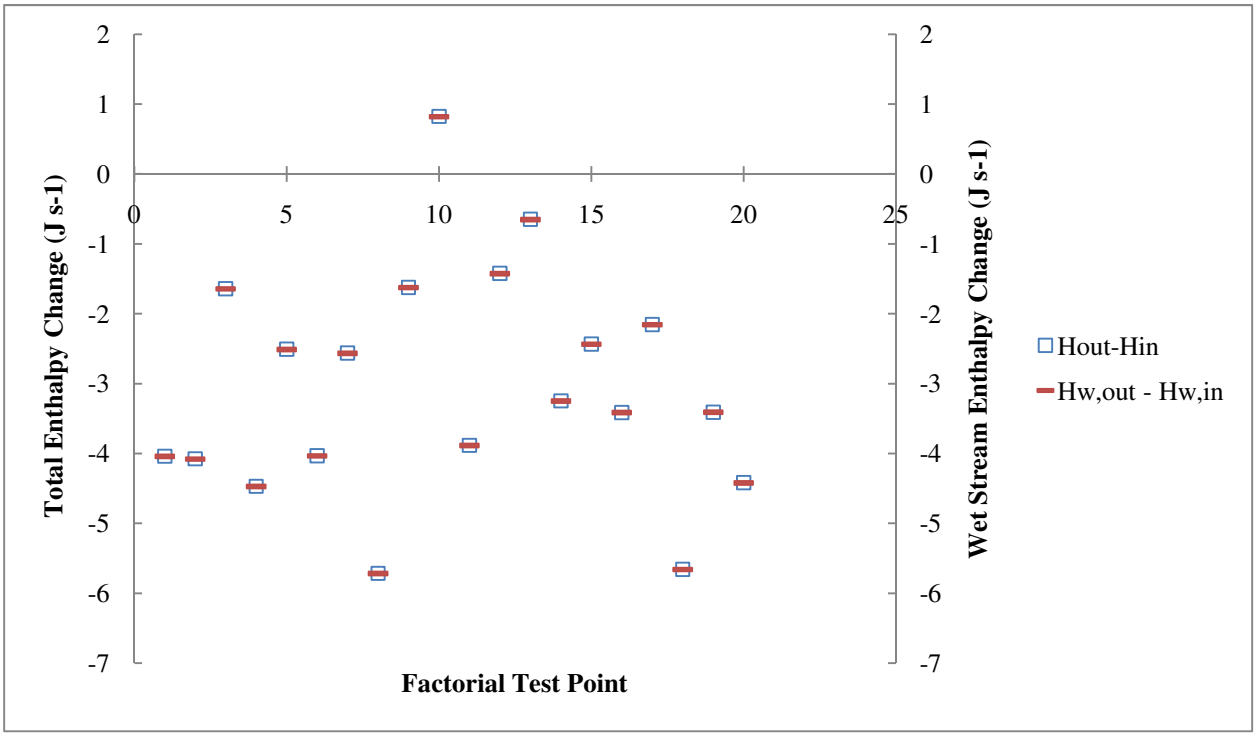


**Figure 56 - Fixture enthalpy balance calculations**

This figure includes an overlay of the enthalpy balance centered on the wet-side stream instead of the overall system. It illustrates that the enthalpy losses on the wet stream dominate the

enthalpy effects for the entire fixture. Note that the data presented in this figure accounts for the enthalpy loss associated with the water transfer from wet to dry streams. In essence $H_{w,in}$ is actually the enthalpy flow of the wet-side air and non-transferable water rather than the entire inlet water content. Dry-side enthalpy balances tended to be very slightly positive due to a slight increase in temperature from inlet to outlet. Figure 56 presents the data in the factorial design experimental order and as such presents it in a rather random fashion. Figure 57 was constructed in order to demonstrate the wet-side enthalpy loss correlation with the fixture temperature.

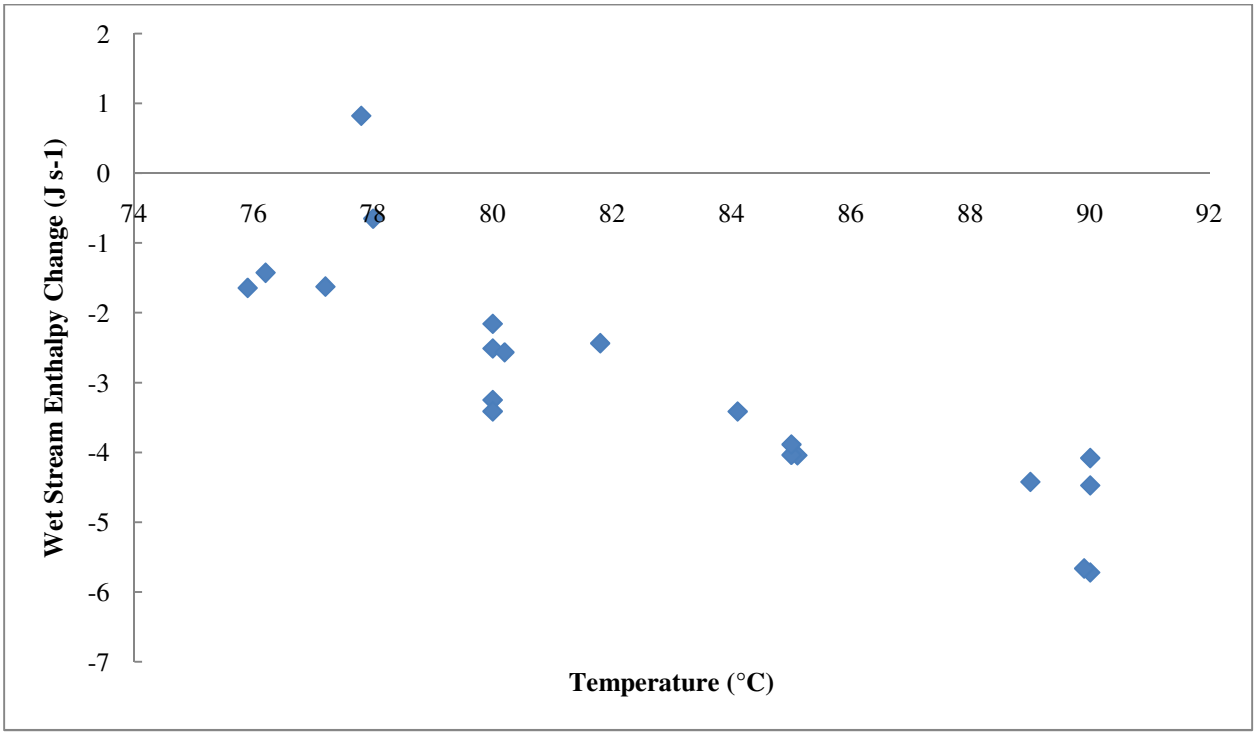


**Figure 57 - Wet-side enthalpy loss correlation with temperature**

It seems that increased temperatures correlate very strongly with increased wet-stream enthalpy losses. It was thus theorized that the experimental apparatus heaters are not properly balanced on the wet- and dry-sides of the fixture. This unbalance resulted in significant overall enthalpy losses through the fixture as well as significant temperature gradients in both the wet and dry streams.

# 6. Conclusions

Polymer electrolyte membrane fuel cells require a specialized humidification technology in order to operate at optimal power outputs. Planar membrane humidifiers have several advantages for automotive applications including relatively simple assembly, a robust design and most importantly the ability to use the fuel cell cathode exhaust as the water source. Manufacturing costs and concerns such as scalability are also addressed in plate-and-frame systems.

A test bench was constructed in order to evaluate flat plate humidifiers. This bench was shown to adequately simulate the performance of automotive fuel cell cathode water generation over a range of typical conditions. It was determined that this experimental apparatus could achieve water balance and that it could be used as a suitable evaluation tool for small scale humidifiers or single cells of a larger stack. A range of industrial membrane and humidifier designs were tested however this data was not included in this thesis. A flat plate humidifier test fixture was built with the intention of using materials with well-known mass transfer characteristics. For example SGL diffusion medium and PFSA membrane, well documented for use in fuel cells, were used in the prototype humidifier. This prototype cathode humidifier was tested over a range of automotive fuel cell system test conditions. Enthalpy balances indicated that the dry-side of the fixture may have been preferentially heated by the PID control system in order to maintain the fixture at the specified set-point. The magnitude of this imbalance is relatively low and can be corrected through independent control of the wet- and dry-sides based on the outlet gas stream temperatures.

In this work it was demonstrated that a relatively simple least-squares analysis can be used to predict the performance of a particular fixture. A significant drawback of this analysis is that it is geometry specific. These analyses are developed for particular channel geometries and membrane chemistries and thus would be of limited application for alternative designs. Nevertheless the methodology has been demonstrated and can be scaled for use within these material and design parameters.

The model developed through the factorial experiment appeared to strongly agree with experimental data. Each of the estimated results was within the experimental uncertainty associated with the apparatus. Similar to the simple least-squares analysis these results are only

valid for this particular humidifier fixture. It was determined that fixture temperature, water concentration, dry-side gas flow rate and the temperature-concentration interaction factors were statistically significant for determining the overall fixture water transfer rate.

It is unclear which method of water coverage estimation provides the most accurate data. Comparison between several regression models did not yield a particular method that was clearly more correct than other methods. The simple regression model exhibited the lowest overall sum of squared error for predicting fractional water coverage for the experimental data collected however it exhibited unexpected behaviour during the single-factor performance effect analyses. The best simple regression method and best factorial-based method have been included as run-time options in the final thesis code.

Table 24 and Table 25 present the abbreviated results from the SoS error analysis of the water coverage estimation methods originally presented in Section 5.6. The primary impact of these results is that the least squares methods may be a better predictor for the standard operational situations derived from actual fuel cell operating conditions while the factorial-derived data is a better descriptor for conditions that lay outside those standard situations.

**Table 24 – Sum of squared error for all data**

| Model | Sum of Squared Error |
|---|---|
| RH-based Least Squares | 0.2696 |
| $C_w$-based Least Squares | 0.3016 |

**Table 25 – Sum of squared error for factorial data**

| Model | Sum of Squared Error |
|---|---|
| RH-based Water Coverage Factorial | 0.1468 |
| $C_w$-based Water Coverage Factorial | 0.1652 |

Even though no particular water coverage estimation method was determined to be the best, in both cases computational modeling results seemed to agree with the experimental data collected. The advantage of this model over the other analysis types is that this model can easily be extended to alternative geometries. Water coverage values could be extended to other situations based on physical conditions within the fixture. This model also has the benefit of allowing analysis using the three region nodal calculation which could be paired with noble gas experiments to determine significance of vapour-phase mass transfer resistance.

# 7. Future Work

Several possibilities for future investigation and development of this performance evaluation software are found below listed in descending priority.

- Confirm the amount of condensed water within the cell during operation by neutron imaging techniques or flash freezing;
- Perform experiments using alternative carrier gases to investigate significance of gas phase transfer with a special emphasis on dry-side transfer;
- Expand model to include mass transfer resistance in the channel/GDM if gas phase resistance is significant;
- Verify model against performances using alternative channel geometries;
- Develop humidifier design tool that leverages results from the model;
- Update PID control system to independently control wet- and dry-side temperatures; and,
- Expand model to include an estimation method for non-uniform water coverage.

# References


[1] L. J. Pettersson and R. Westerholm, "State of the art of multi-fuel reformers for fuel cell vehicles: problem identification and research needs," *International Journal of Hydrogen Energy*, vol. 26, no. 3, pp. 243-264, Mar. 2001.

[2] A. S. Patil et al., "Portable fuel cell systems for America's army: technology transition to the field," *Journal of Power Sources*, vol. 136, no. 2, pp. 220-225, Oct. 2004.

[3] C. Thomas, "Fuel cell and battery electric vehicles compared," *International Journal of Hydrogen Energy*, vol. 34, no. 15, pp. 6005-6020, Aug. 2009.

[4] J. Larminie and A. Dicks, *Fuel Cell Systems Explained*, 2nd ed. John Wiley & Sons.

[5] N. Djilali, "Computational modelling of polymer electrolyte membrane (PEM) fuel cells: Challenges and opportunities," *Energy*, vol. 32, no. 4, pp. 269-280, Apr. 2007.

[6] A. Proracki, T. Mali, and M. Fowler, "Application of High Volume Manufacturing Practices to Fuel Cell Manufacturing," presented at the SMTA International, 2008.

[7] J. T. Gostick, M. A. Ioannidis, M. W. Fowler, and M. D. Pritzker, "On the role of the microporous layer in PEMFC operation," *Electrochemistry Communications*, vol. 11, no. 3, pp. 576-579, Mar. 2009.

[8] R. Huizing, "Design and Membrane Selection for Gas to Gas Humidifiers for Fuel Cell Applications," University of Waterloo, 2007.

[9] D. M. Bernardi and M. W. Verbrugge, "A Mathematical Model of the Solid-Polymer-Electrolyte Fuel Cell," *Journal of The Electrochemical Society*, vol. 139, no. 9, pp. 2477-2491, 1992.

[10] C. Chamberlin, P. Lehman, and R. Reid, "Preliminary Results of the Schatz Fuel Cell Research Project," presented at the World Hydrogen Energy Conference.

[11] J. Kim, S. Lee, S. Srinivasan, and C. E. Chamberlin, "Modeling of Proton Exchange Membrane Fuel Cell Performance with an Empirical Equation," *Journal of The Electrochemical Society*, vol. 142, no. 8, pp. 2670-2674, 1995.

[12] F. Laurencelle et al., "Characterization of a Ballard MK5-E Proton Exchange Membrane Fuel Cell Stack," *Fuel Cells*, vol. 1, no. 1, pp. 66-71, 2001.

[13] S. Srinivasan et al., "Energy Conversion Engineering Conference, 1989. IECEC-89., Proceedings of the 24th Intersociety," presented at the Energy Conversion Engineering Conference, 1989. IECEC-89., Proceedings of the 24th Intersociety, pp. 1623-1629 vol.3, 1989.

[14] K. Kreuer, S. J. Paddison, E. Spohr, and M. Schuster, "Transport in Proton Conductors for Fuel-Cell Applications: Simulations, Elementary Reactions, and Phenomenology," *Chemical Reviews*, vol. 104, no. 10, pp. 4637-4678, Oct. 2004.

[15] S. Motupally, A. J. Becker, and J. W. Weidner, "Diffusion of Water in Nafion 115 Membranes," *Journal of The Electrochemical Society*, vol. 147, no. 9, pp. 3171-3177, 2000.

[16] J. Zawodzinski et al., "Water Uptake by and Transport Through Nafion 117 Membranes," *Journal of The Electrochemical Society*, vol. 140, no. 4, pp. 1041-1047, Apr. 1993.

[17] F. N. Buchi and S. Srinivasan, "Operating Proton Exchange Membrane Fuel Cells Without External Humidification of the Reactant Gases," *Journal of The Electrochemical Society*, vol. 144, no. 8, pp. 2767-2772, 1997.

[18] Y. Yoon, W. Lee, T. Yang, G. Park, and C. Kim, "Current distribution in a single cell of PEMFC," *Journal of Power Sources*, vol. 118, no. 1, pp. 193-199, May. 2003.
[19] Y. Yoon, W. Lee, T. Yang, G. Park, and C. Kim, "Current distribution in a single cell of PEMFC," *Journal of Power Sources*, vol. 118, no. 1, pp. 193-199, May. 2003.
[20] K. Choi, D. Peck, C. S. Kim, D. Shin, and T. Lee, "Water transport in polymer membranes for PEMFC," *Journal of Power Sources*, vol. 86, no. 1, pp. 197-201, Mar. 2000.
[21] T. F. Fuller and J. Newman, "Experimental Determination of the Transport Number of Water in Nafion 117 Membrane," *Journal of The Electrochemical Society*, vol. 139, no. 5, pp. 1332-1337, May. 1992.
[22] J. Smith, H. V. Ness, and M. Abbott, *Introduction to Chemical Engineering Thermodynamics*, 7th ed. McGraw-Hill Science/Engineering/Math, 2004.
[23] R. C. Reid, J. M. Prausnitz, and B. E. Poling, *The Properties of Gases and Liquids*, 4th ed. McGraw-Hill Companies, 1987.
[24] D. Green and R. Perry, *Perry's Chemical Engineers' Handbook, Eighth Edition*, 8th ed. McGraw-Hill Professional, 2007.
[25] W. Mérida, "Diagnosis of PEMFC Stack failures via Electrochemical Impedance Spectroscopy," Thesis in Mechanical Engineering, University of Victoria, 2002.
[26] M. V. Williams, H. R. Kunz, and J. M. Fenton, "Operation of Nafion®-based PEM fuel cells with no external humidification: influence of operating conditions and gas diffusion layers," *Journal of Power Sources*, vol. 135, no. 1, pp. 122-134, Sep. 2004.
[27] K. H. Choi, D. J. Park, Y. W. Rho, Y. T. Kho, and T. H. Lee, "A study of the internal humidification of an integrated PEMFC stack," *Journal of Power Sources*, vol. 74, no. 1, pp. 146-150, Jul. 1998.
[28] M. Santis, D. Schmid, M. Ruge, S. Freunberger, and F. Büchi, "Modular Stack-Internal Air Humidification Concept-Verification in a 1 kW Stack," *Fuel Cells*, vol. 4, no. 3, pp. 214-218, 2004.
[29] D. L. Wood, J. S. Yi, and T. V. Nguyen, "Effect of direct liquid water injection and interdigitated flow field on the performance of proton exchange membrane fuel cells," *Electrochimica Acta*, vol. 43, no. 24, pp. 3795-3809, Aug. 1998.
[30] F. Liu, B. Yi, D. Xing, J. Yu, Z. Hou, and Y. Fu, "Development of novel self-humidifying composite membranes for fuel cells," *Journal of Power Sources*, vol. 124, no. 1, pp. 81-89, Oct. 2003.
[31] S. Kwak, T. Yang, C. Kim, and K. H. Yoon, "The effect of platinum loading in the self-humidifying polymer electrolyte membrane on water uptake," *Journal of Power Sources*, vol. 118, no. 1, pp. 200-204, May. 2003.
[32] M. Watanabe, H. Uchida, Y. Seki, M. Emori, and P. Stonehart, "Self-Humidifying Polymer Electrolyte Membranes for Fuel Cells," *Journal of The Electrochemical Society*, vol. 143, no. 12, pp. 3847-3852, Dec. 1996.
[33] M. Watanabe, H. Uchida, and M. Emori, "Polymer Electrolyte Membranes Incorporated with Nanometer-Size Particles of Pt and/or Metal-Oxides: Experimental Analysis of the Self-Humidification and Suppression of Gas-Crossover in Fuel Cells," *The Journal of Physical Chemistry B*, vol. 102, no. 17, pp. 3129-3137, Apr. 1998.
[34] M. Watanabe, Y. Satoh, and C. Shimura, "Management of the Water Content in Polymer Electrolyte Membranes with Porous Fiber Wicks," *Journal of The Electrochemical Society*, vol. 140, no. 11, pp. 3190-3193, Nov. 1993.
[35] M. Shichun et al., "A Self-Humidifying Composite Membrane with Self-Assembled Pt

Nanoparticles for Polymer Electrolyte Membrane Fuel Cells," *Journal of The Electrochemical Society*, vol. 153, no. 10, pp. A1868-A1872, Oct. 2006.
[36] Y. Liu, B. Yi, Z. Shao, L. Wang, D. Xing, and H. Zhang, "Pt/CNTs-Nafion reinforced and self-humidifying composite membrane for PEMFC applications," *Journal of Power Sources*, vol. 163, no. 2, pp. 807-813, Jan. 2007.
[37] M. Han, S. Chan, and S. Jiang, "Investigation of self-humidifying anode in polymer electrolyte fuel cells," *International Journal of Hydrogen Energy*, vol. 32, no. 3, pp. 385-391, Mar. 2007.
[38] S. Ge, X. Li, and I. Hsing, "Internally humidified polymer electrolyte fuel cells using water absorbing sponge," *Electrochimica Acta*, vol. 50, no. 9, pp. 1909-1916, Mar. 2005.
[39] S. Litster and J. G. Santiago, "Dry gas operation of proton exchange membrane fuel cells with parallel channels: Non-porous versus porous plates," *Journal of Power Sources*, vol. 188, no. 1, pp. 82-88, Mar. 2009.
[40] T. Yang and P. Shi, "Performance of PEMFCs with Internal Humidification," *Journal of The Electrochemical Society*, vol. 153, no. 8, pp. A1518-A1524, 2006.
[41] N. Rajalakshmi, P. Sridhar, and K. S. Dhathathreyan, "Identification and characterization of parameters for external humidification used in polymer electrolyte membrane fuel cells," *Journal of Power Sources*, vol. 109, no. 2, pp. 452-457, Jul. 2002.
[42] R. Glises, D. Hissel, F. Harel, and M. Péra, "New design of a PEM fuel cell air automatic climate control unit," *Journal of Power Sources*, vol. 150, pp. 78-85, Oct. 2005.
[43] S. Tanaka and T. Inamura, "Humidifier," U.S. Patent US 2005/0110172 A1.
[44] Z. Zhong, X. Zhu, and G. Cao, "Modeling a PEMFC by a support vector machine," *Journal of Power Sources*, vol. 160, no. 1, pp. 293-298, Sep. 2006.
[45] S. Park and I. Oh, "An analytical model of Nafion(TM) membrane humidifier for proton exchange membrane fuel cells," *Journal of Power Sources*, vol. 188, no. 2, pp. 498-501, Mar. 2009.
[46] L. Zhang, M. Pan, and S. Quan, "Model predictive control of water management in PEMFC," *Journal of Power Sources*, vol. 180, no. 1, pp. 322-329, May. 2008.
[47] D. McKay, A. Stefanopoulou, and J. Cook, "American Control Conference, 2008," presented at the American Control Conference, 2008, pp. 312-317, 2008.
[48] D. Harvey, J. Pharoah, and K. Karan, "A comparison of different approaches to modelling the PEMFC catalyst layer," *Journal of Power Sources*, vol. 179, no. 1, pp. 209-219, Apr. 2008.
[49] J. O. Hirschfelder, R. B. Bird, and E. L. Spotz, "The transport properties of gases and gaseous mixtures," *Chemical Reviews*, vol. 44, no. 1, pp. 205-231, Feb. 1949.
[50] R. S. Brokaw, "Predicting Transport Properties of Dilute Gases," *Industrial & Engineering Chemistry Process Design and Development*, vol. 8, no. 2, pp. 240-253, Apr. 1969.
[51] J. Zawodzinski et al., "A Comparative Study of Water Uptake By and Transport Through Ionomeric Fuel Cell Membranes," *Journal of The Electrochemical Society*, vol. 140, no. 7, pp. 1981-1985, Jul. 1993.
[52] "Multi-Year Research, Development and Demonstration Plan: Planned Program Activities for 2005-2015," 2007.
[53] D. E. Seborg, T. F. Edgar, and D. A. Mellichamp, *Process Dynamics and Control*, 2nd ed. Wiley, 2003.
[54] J. Welty, C. Wicks, R. Wilson, and G. Rorrer, *Fundamentals of Momentum, Heat, and Mass Transfer*, 5th ed. John Wiley & Sons.

[55] L. S. Lasdon, A. D. Waren, A. Jain, and M. Ratner, “Design and Testing of a Generalized Reduced Gradient Code for Nonlinear Programming,” *ACM Transactions on Mathematical Software*, vol. 4, no. 1, pp. 34-50, 1978.

# Appendix A: Sample Calculations

This section shall take three data points from an experimental run and present the calculations necessary to evaluate humidifier performance. The table below shows the portion of the collected data pertinent to these calculations.

| Runtime (s) | Dry flow rate (SLPM) | Dry Knockout Mass (g) | Dry vent temp (°C) |
|---|---|---|---|
| 530 | 21.078 | 126.369 | 9.1 |
| 540 | 21.383 | 127.327 | 8.9 |
| 550 | 21.078 | 127.710 | 8.9 |

Given the temperatures of the condenser exhaust stream, saturated vapour pressures can be estimated using tabulated values such as those from Perry's Chemical Engineering Handbook [24].

| Dry vent temp (°C) | Saturated Vapour P (atm) |
|---|---|
| 9.1 | 0.0114 |
| 8.9 | 0.0112 |
| 8.9 | 0.0113 |

Assuming the outlet pressure is at one atmosphere, Dalton's law of partial pressures would indicate that the above saturated vapour pressure will represent the mole fraction of water in the gas stream. The water vapour mass flow rate can be determined according to Equation 59 below.

$$\dot{m}_w = \frac{y_w}{1-y_w} * \dot{V}_{dry} * \frac{P_{std}}{R*T_{std}} * M_w \qquad \text{(Eq59)}$$

Using the data from 530 seconds the gaseous water content for that section of time can be calculated.

$$\dot{m}_w = \frac{0.0114}{1-0.0114} * \frac{21.078\ L}{min} * \frac{101325\ \frac{N}{m^2}}{8.314\ \frac{N \cdot m}{mol \cdot K} * 273.15\ K} * \frac{1\ m^3}{1000\ L} * \frac{18\ g}{mol}$$

$$\dot{m}_w = 0.1952 \frac{g}{min} \quad \text{(Eq60)}$$

A cumulative uncondensed water content encompassing the entire experimental run can be determined by taking the above value and multiplying it by the ten second interval for which it is assumed to be valid. The table below shows calculated values from our three interval example.

| Runtime (s) | Vapour rate (g/min) | Cumulative water mass (g) |
|---|---|---|
| 530 | 0.1952 | 0.0325 |
| 540 | 0.1949 | 0.0650 |
| 550 | 0.1926 | 0.0971 |

While the vapour content must be calculated for each ten second interval the condensed water mass can be determined by simply subtracting the initial water knockout mass from the final value.

$$\dot{m}_w = \frac{\{(127.710-126.369)+(0.0971)\}\, g}{(560-530)\, s} * \frac{60\, s}{min} = \frac{2.88\, g}{min} \quad \text{(Eq33)}$$

# Appendix B: Model Code

## Appendix B.1: Diffusion Coefficient of Water in a Gas Mixture

```
%This function evaluates the Dab of water through a gas mixture at
%particular conditions.  'gaslist' should be a vertical array of mole
%fractions in the following order:

%Argon, Helium, Krypton, Neon, Nitrogen, Oxygen, Water
%Inputs: Temperature (Kelvin), Pressure (kPa absolute), Gas composition
%Output: Water Overall diffusion coefficient (cm^2/s).

function Doverall = DabGas(T,P,gaslist)


gaslist=gaslist(:); %Force input to be a column vector
Molarmass=[39.948;4.00260;83.8;20.179;14.00674;15.9994;(2*1.0079+15.9994)];
A=1.06036;
B=0.15610;
C=0.19300;
D=0.47635;
E=1.03587;
F=1.52996;
G=1.76474;
H=3.89411;
%Constants taken from Appendix K.2 (Fundamentals of Momentum, Heat and Mass
%Transfer)
gassigma=[3.418;2.576;3.6;2.898;3.681;3.433;2.649];
epsoverkappa=[124;10.22;190;35.7;91.5;113;356];

numgases=length(Molarmass);

sigmaAB=zeros(numgases,1);
epsABoverkappa=zeros(numgases,1);
omegaD=zeros(numgases,1);
Tstar=zeros(numgases,1);
DAB=ones(numgases,1);

for i=1:(numgases-1)
   if gaslist(i) == 0
   else
      sigmaAB(i)=sqrt(gassigma(i)*gassigma(numgases));
      epsABoverkappa(i)=sqrt(epsoverkappa(i)*epsoverkappa(numgases));
      Tstar(i)=T/epsABoverkappa(i);
      omegaD(i)=A/(Tstar(i)^B)+C/(exp(D*Tstar(i)))+E/(exp(F*Tstar(i)))+G/(exp(H*Tstar(i)));

DAB(i)=0.001858*T^(3/2)*(1/Molarmass(i)+1/Molarmass(numgases))^(1/2)/((P/101.325)*sigmaAB(i)^2*omegaD
(i));
      %page 409-413 of Fundamentals of Momentum, Heat and Mass Transfer
   end
end

denominator=0;
```

```
for j=1:(numgases-1)
   denominator=denominator+gaslist(j)/DAB(j);
   %page 414 of Fundamentals of Momentum, Heat and Mass Transfer
end

Doverall = (1-gaslist(numgases))/denominator;
```

## Appendix B.2: Saturated water vapour pressure

```
%Input: Temperature (Kelvin)
%Output: Water vapour pressure (kPa)
%Calculated according to Wagner's equation.
%Presented: R.C. Reid, J.M. Prausnitz, and B.E. Poling, The Properties
%of Gases and Liquids, McGraw-Hill Companies, 1987.

function pvap = watervapP(Tinput)
A=-7.775;
B=1.466;
C=-2.771;
D=-1.317;
Tcrit=647.31;
Pcrit=exp(10.003);

Tred=Tinput./Tcrit;
lnofPred=(A.*(1-Tred)+B.*(1-Tred).^(1.5)+C.*(1-Tred).^3+D.*(1-Tred).^6)./Tred;

Pred=exp(lnofPred);

pvap=Pred.*Pcrit;
```

## Appendix B.3: Membrane lambda given gas phase water activity

```
% This function evaluates lambda, or moles of water per mole of SO3, given
% the water activity.
% Based on results from "Diffusion of Water in Nafion 115 Membranes" by
% Motupally.
function lambda = lambdagivenact(actw)
coeffs=[36;-39.85;17.81;0.043];
lambda=polyval(coeffs,actw);
```

## Appendix B.4: Diffusion coefficient for lamba below three

```
% This function determines the Fickian diffusion coefficient of water given
% the temperature and the membrane hydration 'lambda' is less than three.
% Based on results from "Diffusion of Water in Nafion 115 Membranes" by
% Motupally.
% Dmemb Units: 'cm^2/s'.
function Dmemb = Dwfbelowthree(lambda,T)
if lambda > 3
   error('Lambda cannot be greater than 3 in this function');
elseif lambda <0
```

```
    error('Lambda cannot be less than 0');
else
    Dmemb=3.1e-3.*lambda.*(-1+exp(0.28.*lambda)).*exp(-2436./T);
end
```

## Appendix B.5: Diffusion coefficient for lambda above three

```
% This function determines the Fickian diffusion coefficient of water given
% the temperature and the membrane hydration 'lambda' is less than three.
% Based on results from "Diffusion of Water in Nafion 115 Membranes" by
% Motupally.
% Dmemb Units: 'cm^2/s'.
function Dmemb = Dwfabovethree(lambda,T)
if lambda < 0
    error('Lambda cannot be less than 0');
elseif lambda < 3
    error('Lambda cannot be less than 3 in this function');
elseif lambda > 22
    error('Lambda exceeds model limit of 22 is temp below 30 deg C?');
else
    Dmemb=4.17e-4.*(lambda+161.*exp(-lambda)).*exp(-2436./T);
end
```

## Appendix B.6: Water flux calculation at particular conditions

```
%This function calculates a water flux through the membrane given
%cellT given in Kelvin
%Inputs: Channel water concs Cw/Cd (mol/m^3), Channel pressures Pwet/Pdry
%(kPa abs), GDL condensation amount (fraction of surface covered), Cell
%temperature cellT(Kelvin)
%Output: Cell water flux (mol/m^2 s)

function fluxoutput = cellflux(Cw, Cd, epsw, membthickness, cellT)

%Calculation of dewpoint at cell temperature
satdconc = watervapP(cellT)*1000/(8.314*cellT); %mol/m^3

membdensity=2*100^3; %g/m^3
Mm=1100; %g/mol

actwet=Cw/satdconc;
actdry=Cd/satdconc;

if (actwet > 1) || (actdry > 1)
    error('Water concentration is above saturation!')
end

lambdawet= lambdagivenact(actwet);
lambdadry= lambdagivenact(actdry);

%calc flux in water covered area
liqwaterlambda=22-(22-17)/(80-30)*(cellT-(273.15+30)); %linear interpolation of values at 30C and 80C

if lambdadry > lambdawet
    liqflux=0;
```

```
    gasflux=0;
else
    if (lambdadry > 3) && (lambdawet > 3)
        liqflux=membdensity/(Mm*membthickness)*quad(@(x)Dwfabovethree(x,cellT),lambdadry, liqwaterlambda);
        gasflux=membdensity/(Mm*membthickness)*quad(@(x)Dwfabovethree(x,cellT),lambdadry, lambdawet);
    elseif (lambdadry < 3) && (lambdawet >3)
        liqflux=membdensity/(Mm*membthickness)*quad(@(x)Dwfbelowthree(x,cellT),lambdadry,3)+
membdensity/(Mm*membthickness)*quad(@(x)Dwfabovethree(x,cellT),3,liqwaterlambda);
        gasflux=membdensity/(Mm*membthickness)*quad(@(x)Dwfbelowthree(x,cellT),lambdadry,3)+
membdensity/(Mm*membthickness)*quad(@(x)Dwfabovethree(x,cellT),3,lambdawet);
    else
        liqflux=membdensity/(Mm*membthickness)*quad(@(x)Dwfbelowthree(x,cellT),lambdadry, 3)+
membdensity/(Mm*membthickness)*quad(@(x)Dwfabovethree(x,cellT),3,liqwaterlambda);
        gasflux=membdensity/(Mm*membthickness)*quad(@(x)Dwfbelowthree(x,cellT),lambdadry, lambdawet);
    end
end
%liqflux and gasflux are in mol cm^2 / m^4 s, must convert to mol / m^2 s
fluxoutput=((1-epsw)*gasflux+(epsw)*liqflux)/(100^2);
```

## Appendix B.7: Main script for overall fixture performance

```
%thesismain.m is the main file run in order to set up the humidifier
%simulation

%commands to read operating conditions and geometry

numruns=size(Tarray);
overallflux=zeros(numruns);

drychnlwidth=0.15/100; %in m
drychnldepth=0.05/100; %in m
drychnllength=0.14; %in m
wetchnlwidth=0.15/100; %in m
wetchnldepth=0.05/100; %in m
wetchnllength=0.28; %in m
membthickness=50*10^-6; %in m
drynumchnl=87;
wetnumchnl=31;

for m=1:numruns
    cellT=273.15+Tarray(m); %in K
    wetflow=wetflowarray(m); %in SLPM, dry basis
    dryflow=dryflowarray(m); %in SLPM, dry basis
    dryP=101.325+dryParray(m); %in kPa absolute
    wetP=101.325+wetParray(m); %in kPa absolute
    wetinletRH=wetRHarray(m);
    dryinletRH=dryRHarray(m);


    %epsw Estimation
    epswestmode=1;
    %Mode 0: epsw is a predefined constant specified by the user
    %Mode 1: epsw is a constant calculated using a general least-squares regression model
```

```
    %Mode 2: epsw is a constant calculated using a factorial-derived
    %regression model
    %Mode 3: epsw is a non-constant array generated by function initepsw.m

    if epswestmode==0
        epsw=0.43;
    elseif epswestmode==1
        wetchnlvol=wetnumchnl*wetchnllength*wetchnldepth*wetchnlwidth*1000; %in L
        drychnlvol=drynumchnl*drychnllength*drychnldepth*drychnlwidth*1000; %in L
        actualwetflow=wetflow*101.325/273.15*(cellT)/(wetP); %in L/min
        actualdryflow=dryflow*101.325/273.15*(cellT)/(dryP); %in L/min
        wetSV=(actualwetflow/60)/wetchnlvol; %Space Velocity in 1/s
        drySV=(actualdryflow/60)/drychnlvol; %Space Velocity in 1/s
        %Coefficients: [x0 T T^2 1/T 1/T^2 SVw SVw^2 1/SVw 1/SVw^2 SVd SVd^2 1/SVd 1/SVd^2
        %RH RH^2 1/RH 1/RH^2]
        cellTC=cellT-273.15;
        ecof=[-0.36647880428812;
            -0.0344791849594583;
            0.000166601342502353;
            -0.00896094703573905;
            -0.000163747665832341;
            -0.122652481800567;
            0.000783567924206526;
            -0.0373687929563857;
            -0.00275026270583079;
            0.263908337824153;
            -0.00226255061832048;
            -0.0383241735995554;
            -0.00279730455754524;
            -0.0130866630679548;
            0.265168732054913;
            -0.564001654246613;
            0.138260091009553];

epsw=ecof(1)+ecof(2)*cellTC+ecof(3)*cellTC^2+ecof(4)/cellTC+ecof(5)/cellTC^2+ecof(6)*wetSV+ecof(7)*wetS
V^2+ecof(8)/wetSV+ecof(9)/wetSV^2+ecof(10)*drySV+ecof(11)*drySV^2+ecof(12)/drySV+ecof(13)/drySV^2+ec
of(14)*wetinletRH+ecof(15)*wetinletRH^2+ecof(16)/wetinletRH+ecof(17)/wetinletRH^2;
    elseif epswestmode==2
        %Calculating the wet and dry space volumes
        wetchnlvol=wetnumchnl*wetchnllength*wetchnldepth*wetchnlwidth*1000; %in L
        drychnlvol=drynumchnl*drychnllength*drychnldepth*drychnlwidth*1000; %in L
        wetstdSV=(wetflow/60)/wetchnlvol; %Space Velocity in 1/s
        drystdSV=(dryflow/60)/drychnlvol; %Space Velocity in 1/s

        cellTC=cellT-273.15;
        %need to code the independent variables
        codedT=(cellTC-85)/5;
        codedRH=(wetinletRH-0.713)/0.219;
        codedwetSV=(wetstdSV-71.94)/18.177;
        codeddrySV=(drystdSV-51.268)/12.954;

        ecof=[0.401822552;
            -0.027809724;
            0.227405009722522;
            0.151484160077179;
```

```
        0.0320500564827515;
        0.175179940415389;
        0.0123335671728742;];

epsw=ecof(1)+codedT*ecof(2)+codedRH*ecof(3)+codeddrySV*ecof(4)+codedT*codedRH*ecof(5)+codedRH*cod
eddrySV*ecof(6)+codedT*codedRH*codeddrySV*codedwetSV*ecof(7);
  elseif epswestmode==3
    maxepsw=0.45;
    minepsw=0.91*maxepsw;
    nodesatmax=1;
    epsarray=initepsw(drynumchnl, wetnumchnl, maxepsw, minepsw, nodesatmax);
    %epsarray=zeros(wetnumchnl,drynumchnl); %For non-continous epsw
    %epsarray(:,1:38)=1; %For non-continous epsw
  else
    error('Epsilon estimation mode not defined')
  end

  %Check to see if estimation method
  if epsw>1
    warning('Water coverage is greater than 1')
    iteration=m
  elseif epsw<0
    warning('Water coverage is less than 0')
    iteration=m
  end
  epswstddev=0.0397;

  %Initializing arrays to store information by cell
  if m==1
    drywaterflow=zeros(wetnumchnl, drynumchnl); %mol/min
    wetwaterflow=zeros(wetnumchnl, drynumchnl); %mol/min
    localflux=zeros(wetnumchnl, drynumchnl); %g/cm^2 s
  end

  %Calculate carrier gas molar flow rates per channel
  drygasmolflow=(dryflow*101325/(8.314*273.15*1000))/drynumchnl; %n = V*P/(R*T),mol/min
  wetgasmolflow=(wetflow*101325/(8.314*273.15*1000))/wetnumchnl; %n = V*P/(R*T),mol/min

  %Set up channel inlet conditions
  dryinletwaterflow= InjfromRH(dryflow,dryP,cellT,dryinletRH)/(60*18*drynumchnl); %mol/min
  wetinletwaterflow= InjfromRH(wetflow,wetP,cellT,wetinletRH)/(60*18*wetnumchnl); %mol/min
  drygasconc=dryP*1000/(8.314*cellT); %mol/m^3
  wetgasconc=wetP*1000/(8.314*cellT); %mol/m^3

  for i = 1:wetnumchnl
    for j=1:drynumchnl

      if i==1
        drycellwater=dryinletwaterflow;
      else
        drycellwater=drywaterflow(i-1,j);
      end
      if j==1
        wetcellwater=wetinletwaterflow;
      else
```

```
            wetcellwater=wetwaterflow(i,j-1);
        end

        if drycellwater<0 ||wetcellwater<0
            error('Channel flows are negative!')
        end

        wetwaterconc=wetcellwater/(wetcellwater+wetgasmolflow)*wetgasconc; %mol/m^3
        drywaterconc=drycellwater/(drycellwater+drygasmolflow)*drygasconc; %mol/m^3

        %reassigns epsw variable if the gradient water coverage mode is
        %activated
        if epswestmode==3
            epsw=epsarray(i,j);
        end

        localflux(i,j)= cellflux(wetwaterconc, drywaterconc, epsw, membthickness, cellT); %mol/m^2 s
        watertransfer=(wetchnlwidth)*(drychnlwidth)*localflux(i,j)*60; %mol/min

        wetwaterflow(i,j)=wetcellwater-watertransfer;
        drywaterflow(i,j)=drycellwater+watertransfer;

      end
    end

    %mass flows are in mol/min, sum the water at the outlet and convert to
    %g/min
    overallflux(m)=(sum(drywaterflow(wetnumchnl,:))-dryinletwaterflow*drynumchnl)*18;
end
runcomplete=true
```